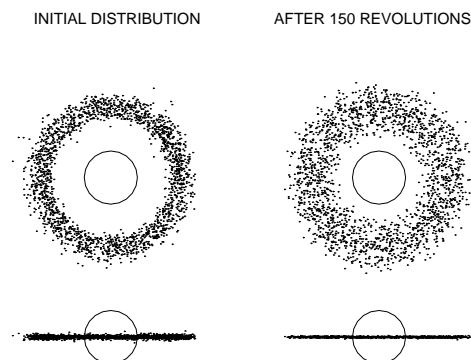


# Computer Simulations of Planetary Rings (8.3.2016)

H. SALO, K. OHTSUKI AND M. C. LEWIS

The local dynamics of planetary rings is governed by the orbital motion, the frequent impacts between ring particles, their mutual self-gravity, and the perturbations exerted by external satellites and embedded moonlets. In Saturn's dense A and B rings the particles collide  $\sim 100$  times per orbital revolution. Although the orbital velocities are  $\sim 20$  km/s, the random velocities related to orbital eccentricities and inclinations are small, of the order of few mm/s (this corresponds to a ring vertical thickness of few tens of meters, excluding strongly perturbed regions). Such gentle impacts do not lead to fragmentation, but still dissipate a significant fraction of random kinetic energy in each collision. This loss is balanced by the viscous gain of energy from the orbital motion around the planet, resulting in a local steady-state in a time scale of few tens of impacts/particle (Hämeen-Anttila, 1978; Goldreich and Tremaine, 1978b; Stewart et al., 1984). Characteristics of this energy balance (such as velocity dispersion, geometric thickness, and viscosity) are determined by the frequency and elasticity of impacts, and by the internal density and size distribution of particles. In much longer timescales the ring radial evolution is governed by viscous evolution. Depending on the viscosity-density relation following from the energy balance, the ring can be either stable or unstable against the viscous growth of local perturbations. For example, dense rings composed of quite inelastic particles can become viscously overstable, while less dissipative particle may be prone to viscous instability.

The fundamental importance of ring particles' feeble mutual gravity for shaping the fine structure of Saturn's rings is strikingly demonstrated by the Cassini stellar (Colwell et al., 2006, 2007; Hedman et al., 2007) and radio occultation measurements (Thomson et al., 2007), which confirm the presence of unresolved trailing structures (self-gravity wakes (Salo, 1992a)) throughout the A and B rings. These transient, continuously re-generated trailing density enhancements arise as a superposition of tiny wakes excited around each individual ring particle, amplified by the interplay of shear and gravity (swing-amplification mechanism, see: Toomre, 1981; Goldreich and Lynden-Bell, 1965). Such structures were envisioned already decades ago (Julian and Toomre, 1966), though in a very different context (and scale - kpcs rather than tens of meters), as a suggestion of how to create and maintain spiral structure in galactic stellar disks. In planetary rings the dissipative impacts between particles provide a natural mechanism which keeps the rings dynamically cool and reactive to such gravitational disturbances.



**Figure 1.1** Simulation example of azimuthally complete ring. The number of particles  $N=2000$ , and the particle radius is  $0.005a$ , where  $a$  is the mean distance of particles. The initial width of the ring is  $0.2a$ , yielding a dynamical optical depth  $\tau_D = 0.125$ . The impacts are described with a constant coefficient of restitution  $\epsilon_n = 0.5$ . During 150 orbital revolution each particle has experienced on the average about 250 impacts: the system has flattened to a few particle diameter thick disk, and has at the same time nearly doubled its radial width.

For the same reason the excitation of spiral density waves at satellite resonance locations (Goldreich and Tremaine, 1978a)- another concept originally developed in the context of galaxy dynamics - has its clearest manifestation in Saturn's rings (see e.g. Burns and Cuzzi, 2006; Cuzzi et al., 2010); Saturn's rings also provide the most extreme examples of disk warping (Hedman et al., 2011), and the Julian-Toomre type wakes excited around individual massive boulders orbiting among the ring particles ('propellers') (Spahn and Sremčević, 2000).

This Chapter reviews numerical N-body simulations of self-gravitating, mutually colliding particles, concentrating on a local method, where the evolution of a small ring patch co-moving with the mean orbital motion is followed. After reviewing the main ingredients of the simulations (dynamical equations, treatment of boundaries, impacts, and self-gravity), we illustrate the basic mechanisms affecting the local energy balance and give simulation examples of self-gravity wakes and the nonlinear structures resulting from viscous overstability and instability. For detailed theoretical background, see Chapters XX. For simulations including external perturbations and dealing with the large scale evolution of the rings, see Chapters YY.

### 1.1 Early simulation studies

The pioneering simulation studies of the collisional evolution of planetary rings were performed in the 1970s, by Trulsen (1972), Brahic (1977) and Hämeen-Anttila and Lukkari (1980). All these simulations used the same basic approach: a complete ring of particles revolving the central body in Keplerian orbits. The particles were identical hard spheres, and impacts were treated as leading to instantaneous changes of relative velocity vectors. Since only a few hundred particles could be followed with the available computer capacity, these simulations were limited to low optical depth  $\tau_D \lesssim 10^{-3}$ . The particle sizes were unrealistically large compared to the width of the ring, which made it difficult, for example, to separate the time scales for the establishment of local steady-state velocity dispersion from the viscous radial spreading (see Fig. 1.1). Nevertheless, many basic characteristics of collisional systems (see Section 1.6) were discovered, including the existence of a critical upper limit for the coefficient of restitution  $\epsilon_{cr}$ , required for a stable thermal balance in the case of constant  $\epsilon_n$  (Trulsen, 1972), a minimum residual velocity dispersion of the order of few times  $nR$  (Brahic, 1977), where  $n$  is the local angular velocity and  $R$  the particle radius, and the establishment of equilibrium with a finite velocity dispersion in a case of a velocity-dependent coefficient of restitution (Hämeen-Anttila and Lukkari, 1980). These simulations also served as important checks for various analytic treatments (see Stewart et al. (1984)). Brahic (1977) also provided the first constraints for the velocity dispersion in Saturn's rings, in terms of timescales for viscous spreading. However, a fundamental breakthrough was provided by the Wisdom and Tremaine (1988) application of local method to planetary ring simulations.

In contrast to the simulations of a complete ring, in local simulations all calculations are restricted to a small region co-moving with the mean orbital motion of the particles (Fig. 1.2). This allows to extend the simulations to high optical depths, with realistic particle sizes. However, due to systematic velocity shear individual particles will rapidly leave the calculation region. As described in detail below, this is taken into account by periodic boundary conditions, returning the leaving particles to the calculation region with properly modified position and velocity vectors. An important advantage of the method is that it facilitates the study of local steady-state properties as a function of fixed optical depth. The larger-scale viscous evolution can then be deduced from the viscosity-density relation derived from a set of small-scale simulations for different optical depths. This is justified, based on the large separation of the time scale for the establishment of the local thermal balance ( $\propto (\tau_D n)^{-1}$ ), and the much longer time scale for the radial evolution ( $\propto W^2/\nu \propto (\tau_D n)^{-1}(W/H)^2$ , where  $\nu$  is the kinematic viscosity,  $W$  is the radial scale of interest, and  $H$  is the ring vertical thickness).

The local method, developed for Molecular Dynamics simulations by Lees and Edwards (1972), was first applied to planetary rings by Wisdom and Tremaine (1988) and to stellar disks by Toomre and Kalnajs (1991). In the former

study impacts between identical particles were taken into account, but not their mutual gravity, whereas the latter study concentrated only on gravitational forces. In Salo (1992a) both, gravity and impacts, were simultaneously included. Since then, the local method has been extensively used (e.g. Richardson, 1993, 1994; Salo, 1995; Mosqueira, 1996; Daisaka and Ida, 1999; Lewis and Stewart, 2000; Daisaka et al., 2001; Ohtsuki, 1999; Robbins et al., 2010; Perrine and Richardson, 2012).

### 1.2 The Local Simulation Method

The coordinate system in the local method has its origin at  $\vec{r}_0$ , a reference point orbiting the planet of mass  $M$  in a circular orbit at the distance  $a$ , with a constant angular velocity  $n = \sqrt{GM_p/a^3}$ . The x-axis points in the radial direction, the y-axis in the direction of orbital motion, and the z-axis is perpendicular to the equatorial plane, parallel to the angular velocity vector  $\vec{n} = n\hat{z}$ . Since a rotating reference frame is used, the equations of motion are

$$\ddot{\vec{r}} + 2\vec{n} \times \dot{\vec{r}} + \vec{n} \times (\vec{n} \times \vec{r}) = \vec{F}_G/m + \vec{F}/m \quad (1.1)$$

where  $\vec{r} = (x, y, z)$  is a particle's radius vector with respect to  $\vec{r}_0$ ,  $\vec{F}_G$  denotes the central force on the particle relative to the force at  $\vec{r}_0$ ,  $\vec{F}$  the additional forces, and the two last terms on the left hand side represent the Coriolis and centrifugal terms, respectively. For the Keplerian case (spherically symmetric central body) the difference in the acceleration due to central field is

$$\begin{aligned} \vec{F}_G/m &= -GM \left( \frac{\vec{r}_0 + \vec{r}}{|\vec{r}_0 + \vec{r}|^3} - \frac{\vec{r}_0}{a^3} \right) \\ &\approx -\frac{GM}{a^3} \left( \vec{r} - 3\frac{\vec{r} \cdot \vec{r}_0}{a^2} \vec{r}_0 \right) \\ &= n^2(2x, -y, -z), \end{aligned} \quad (1.2)$$

if only terms linear in  $|\vec{r}|/a$  are retained. In the more general case where the azimuthal, radial, and vertical frequencies ( $n$ ,  $\kappa$ , and  $n_z$ ) are different from each other<sup>1</sup>

$$\vec{F}_G/m = \left( (3n^2 - \kappa^2)x, -n^2y, -n_z^2z \right), \quad (1.3)$$

with

$$\begin{aligned} n^2 &= \left. \frac{F_r}{r} \right|_{\vec{r}=\vec{r}_o}, \\ \kappa^2 &= \left. \frac{1}{r^3} \frac{d}{dr} (r^3 F_r) \right|_{\vec{r}=\vec{r}_o}, \\ n_z^2 &= \left. \frac{d}{dz} (F_z) \right|_{\vec{r}=\vec{r}_o}, \end{aligned}$$

where  $F_r$  and  $F_z$  are the radial and vertical components of the central force. Inserting this to Eq. (1.1) yields

$$\begin{aligned} \ddot{x} - 2n\dot{y} + (\kappa^2 - 4n^2)x &= F_x/m, \\ \ddot{y} + 2n\dot{x} &= F_y/m, \\ \ddot{z} + n_z^2 z &= F_z/m, \end{aligned} \quad (1.4)$$

<sup>1</sup> Note that in this Chapter the symbol  $n_z$  is used for the vertical frequency instead of  $\nu$ ; the latter symbol is reserved for kinematic shear viscosity

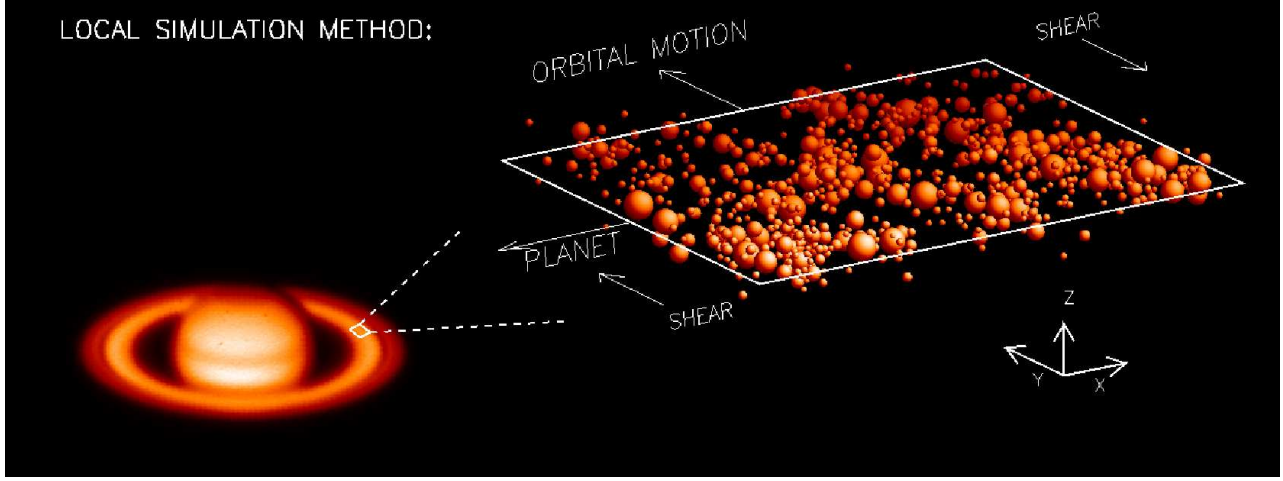


**Figure 1.2** Schematic representation of the local simulation method (“shearing brick” method) (see text for explanation).

where  $F_x, F_y, F_z$  stand for the components of additional forces besides the central force, e.g. due to impacts and particles’ mutual gravity. This is the familiar Hill-approximation, describing the elliptical motion in terms of epicycles superposed on the circular motion of the guiding centre. In the absence of additional forces Eqs. (1.4) have the solution

$$\begin{aligned} x &= x_0 - A \cos[\kappa(t - t_0)], \\ y &= y_0 + \frac{2nA}{\kappa} \sin[\kappa(t - t_0)] + \frac{\kappa^2 - 4n^2}{2n} x_0 t, \\ z &= B \sin[n_z(t - t_1)], \end{aligned} \quad (1.5)$$

where  $x_0, y_0, A, t_0, B, t_1$  are six constants of integration:  $x_0$  and  $y_0$  are given by the guiding centre location at  $t = 0$ , while  $A = ea, B = Ia$  correspond to eccentricity and inclination, and  $t_0, t_1$  to the times of pericenter and ascending node passage, respectively. The guiding centre drifts tangentially with the speed  $sx_0$ , where the shear rate

$$s = \frac{\kappa^2 - 4n^2}{2n} \quad (1.6)$$

reduces to  $s = -\frac{3}{2}n$  in the Keplerian case.

The use of linearized equations is physically well justified, as the typical particle excursion from circular orbit may be expected to be at least a factor of  $10^{-6}$  smaller than  $a$ . Furthermore, through the linearization the set of Eqs. (1.4) is invariant under the transformation

$$\begin{aligned} (x', y', z') &= (x + \Delta x, y + \Delta y + \Delta x st, z), \\ (v'_x, v'_y, v'_z) &= (v_x, v_y + \Delta x s, v_z), \end{aligned} \quad (1.7)$$

where  $\Delta x$  and  $\Delta y$  denote arbitrary shifts in radial and tangential directions, respectively. This allows to use simple periodic boundary conditions in simulations: using  $\Delta x = n_x L_x$  and  $\Delta y = n_y L_y$ , where  $n_x$  and  $n_y$  are integers, and  $L_x$  and  $L_y$  denote the radial and tangential dimensions of the calculation region,

$$\begin{aligned} (x', y', z') &= (x + n_x L_x, y + n_y L_y + n_x L_x st, z), \\ (v'_x, v'_y, v'_z) &= (v_x, v_y + n_x L_x s, v_z), \end{aligned} \quad (1.8)$$

with  $|n_x|, |n_y| = 1, 2, \dots$ , define a set of image particles (replicas, see Fig. 1.3), so that each particle leaving the actual calculation region ( $|x| > L_x/2$  or  $|y| > L_y/2$ ), is replaced by one of its replicas which enters the region from

the opposite face, with appropriately modified position and velocity. Especially, if the particle crosses the outer or inner radial boundary, the tangential velocity of the particle is modified by  $\Delta v_y = \pm s L_x$ , which corresponds to the difference of shear velocity across  $L_x$ . Since the mean tangential velocity at the radial coordinate  $x$  equals  $sx$ , this leaves the shear corrected tangential velocity  $v_y - sx$  unaffected. With the use of these periodic boundary conditions the evolution of the system is independent of the choice of the origin of the coordinate system. The resulting steady-state properties are also independent of the size of the calculation region, provided that the size is large compared to the mean free path between impacts (Wisdom and Tremaine (1988), Salo (1991)). Implicitly it is assumed in the local method that the rings are homogeneous on a scale comparable or larger than the size of the simulation region.

For a system of  $N$  particles moving according to Eqs. (1.4) the quantities

$$\begin{aligned} U &= \frac{1}{m_{tot}} \sum_{i=1}^N m_i \dot{x}_i, \\ V &= \frac{1}{m_{tot}} \sum_{i=1}^N m_i (\dot{y}_i - s x_i), \end{aligned} \quad (1.9)$$

are the analogues to centre-of-mass velocities, where  $m_{tot}$  is the total mass. From Eqs. (1.4),

$$\begin{aligned} m_{tot}(\dot{U} - 2nV) &= \sum_i \sum_j F_x^{ij}, \\ m_{tot}(\dot{V} + (2n + s)U) &= \sum_i \sum_j F_y^{ij}, \end{aligned} \quad (1.10)$$

where  $\vec{F}^{ij}$  stands for the mutual impact or gravity force, exerted by particle  $j$  on particle  $i$ . Since the forces cancel pairwise, the sums on the right-hand sides vanish. Also,  $U$  and  $V$  are unaffected by boundary crossings. Thus,  $U$  and  $V$  remain zero at all times if they vanish initially. This provides an useful check for the accuracy of the orbit and impact calculations. In the more general case,  $U$  and  $V$  oscillate about

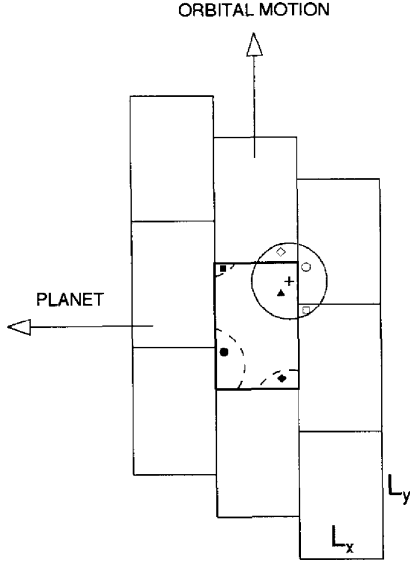


**Figure 1.3** Schematic diagram displaying the simulation cell (thick lines) and its eight surrounding replicas (thin lines). Gravitational forces on the given target particle (marked by cross) are calculated from the particles whose nearest images lie within a given maximum distance marked by the circle. The nearest image can either be the actual particle (solid symbols) or one of its copies (open symbols). Likewise, collisional calculations take into account impacts with image particles.

their initial values, but as shown in Wisdom and Tremaine (1988), the evolution of a system with arbitrary  $U_0$  and  $V_0$  is easily determined from the evolution with  $U_0 = V_0 = 0$ .

Eqs. (1.4) have the energy integral (multiply with velocities and integrate once),

$$E = \sum_i m_i \left( \frac{1}{2} (\dot{x}_i^2 + \dot{y}_i^2 + \dot{z}_i^2) + n s x_i^2 + \frac{1}{2} n z^2 z_i^2 \right) - \frac{1}{2} \sum_i \sum_{j \neq i} G \frac{m_i m_j}{|\vec{r}_j - \vec{r}_i|}, \quad (1.11)$$

the last term representing the self-gravitational potential energy (we have assumed that the additional forces arise from mutual self-gravity). In contrast to centre-of-mass velocities, the quantity  $E$  does not remain constant in boundary crossings or impacts.

### 1.3 Impact calculations

#### 1.3.1 Instantaneous Impacts

In most local simulations (Wisdom and Tremaine (1988), Salo (1991, 1992b,a); Richardson (1993)) an impact model with instantaneous velocity changes has been used. This is well justified, as the contact time in impacts is probably less than one second (Bridges et al., 1984), or of the order of  $10^{-5}$  orbital periods. The damping of the relative velocity between a particle pair in the direction perpendicular to the impact plane is specified by the normal coefficient of

restitution  $\epsilon_n$ , describing the energy loss due to irreversible deformations during the impact. Similarly, the tangential coefficient of restitution,  $\epsilon_t$ , can be included, describing the change of the relative velocity component along the impact plane. In this case the exchange of energy with the particles' spin motion needs also be taken into account. Surface irregularities and the overall non-spherical shape of the particles may also affect the impact outcome. Below we summarize the equations for the velocity and spin changes in impacts, following from the specified elastic model and the conservation laws of linear and angular momentum. The equations are first derived in an inertial frame, and then we discuss the slight modifications required when a local rotating frame is used.

##### 1.3.1.1 Contact dynamics

The pre-collisional position, velocity, and spin vector of the impacting particle are denoted by  $\vec{r}$ ,  $\dot{\vec{r}}$ , and  $\vec{\omega}$ , respectively, and its radius and mass by  $R$  and  $m$ . The impact partner is distinguished by the subscript 1, and the post-collisional quantities by a prime. We define

$$\begin{aligned} \vec{v} &= \dot{\vec{r}}_1 - \dot{\vec{r}}, \\ \vec{k} &= \frac{\vec{r}_1 - \vec{r}}{R + R_1}, \end{aligned} \quad (1.12)$$

standing for the velocity difference of the particle centres, and for the unit vector in the direction joining the particle centres. For an impact to take place  $\vec{v} \cdot \vec{k} < 0$ . The pre-collisional velocity difference at the contact point, taking into account the spins, is

$$\vec{g} = (\dot{\vec{r}}_1 - R_1 \vec{\omega}_1 \times \vec{k}) - (\dot{\vec{r}} + R \vec{\omega} \times \vec{k}) \quad (1.13)$$

$$= \vec{v} - (R \vec{\omega} + R_1 \vec{\omega}_1) \times \vec{k}. \quad (1.14)$$

The post-collisional contact velocity  $\vec{g}'$  is determined by the impact model, giving its components in three orthogonal directions  $\vec{k}$ ,  $\vec{k} \times (\vec{g} \times \vec{k})$ , and  $\vec{g} \times \vec{k}$ , of which the last two lay on the impact plane; unit vectors in these directions will be denoted by  $\vec{k}_T$  and  $\vec{k}_\gamma$ , respectively. Note that these vectors form a right-handed system. We use the notation

$$\vec{g}' = -\epsilon_n \vec{k} \vec{k} \cdot \vec{g} + \epsilon_t \vec{k} \times (\vec{g} \times \vec{k}) + \epsilon_\gamma \vec{g} \times \vec{k}, \quad (1.15)$$

which implies

$$\begin{aligned} \vec{k} \cdot \vec{g}' &= -\epsilon_n \vec{k} \cdot \vec{g}, \\ \vec{k} \times (\vec{g}' \times \vec{k}) &= \epsilon_t \vec{k} \times (\vec{g} \times \vec{k}) + \epsilon_\gamma \vec{g} \times \vec{k} \end{aligned} \quad (1.16)$$

Thus  $\epsilon_n$  denotes the coefficient of normal restitution, and if  $\epsilon_\gamma = 0$ , then  $\epsilon_t$  corresponds to friction. For totally elastic impacts  $\epsilon_n = 1$  while with  $\epsilon_n = 0$  the post-collisional perpendicular velocity difference vanishes. Similarly  $\epsilon_t = 1$  means a frictionless impact while if  $\epsilon_t = 0$  the whole tangential velocity difference at the contact point is lost. Note that  $\epsilon_n = \epsilon_t = 0$  does not imply sticking of particles as the orbital motion is free to separate them. In principle,  $-1 \leq \epsilon_t < 0$  is also physically meaningful, corresponding to reversal of tangential velocity difference (Shu and Stewart, 1985). A non-zero  $\epsilon_\gamma$  can be used to describe the effect of

surface irregularities, giving rise to a post-collisional velocity component perpendicular to both  $\vec{k}$  and  $\vec{g}$ . If included,  $\epsilon_\gamma$  needs to be a random variable with a zero mean, and since surface irregularities affect also in the direction of  $\vec{k} \times (\vec{g} \times \vec{k})$ , a similar random component needs to be present in  $\epsilon_t$ .

The collisional changes of particles' velocity and spin vectors,

$$\begin{aligned} \Delta \vec{r} &= \vec{r}' - \vec{r}, & \Delta \vec{r}_1 &= \vec{r}'_1 - \vec{r}_1, \\ \Delta \vec{\omega} &= \vec{\omega}' - \vec{\omega}, & \Delta \vec{\omega}_1 &= \vec{\omega}'_1 - \vec{\omega}_1 \end{aligned} \quad (1.17)$$

are determined by the conservation of linear momentum

$$m\vec{r}' + m_1\vec{r}'_1 = m\vec{r} + m_1\vec{r}_1, \quad (1.18)$$

and the conservation of angular momentum

$$\begin{aligned} m\vec{r} \times \vec{r}' + m_1\vec{r}_1 \times \vec{r}'_1 + J\vec{\omega}' + J_1\vec{\omega}'_1 \\ = m\vec{r} \times \vec{r} + m_1\vec{r}_1 \times \vec{r}_1 + J\vec{\omega} + J_1\vec{\omega}_1 \end{aligned} \quad (1.19)$$

where  $J$  and  $J_1$  denote the particles' moments of inertia. These equations can be written into more compact form

$$m\Delta \vec{r} + m_1\Delta \vec{r}_1 = 0 \quad (1.20)$$

$$m\vec{r} \times \Delta \vec{r} + m_1\vec{r}_1 \times \Delta \vec{r}_1 + J\Delta \vec{\omega} + J_1\Delta \vec{\omega}_1 = 0 \quad (1.21)$$

Together with the model for  $\vec{g}'$  (Eq. 1.15), the conservation laws provide nine conditions for the six post collisional velocity components and six spin components. The remaining three relations are obtained by determining how the change of spin is distributed between the two particles. Since the forces acting on both particles are identical except in their sign, the torques during the impact are proportional to the particle radii,

$$\frac{J\Delta \vec{\omega}}{R} = \frac{J_1\Delta \vec{\omega}_1}{R_1}. \quad (1.22)$$

To simplify the notations in solving the above set of 12 equations, Eqs. (1.15), (1.20) - 1.22), we define

$$\vec{q} \equiv R\vec{\omega}, \quad \vec{q}_1 \equiv R_1\vec{\omega}_1, \quad \vec{q}_s \equiv \vec{q} + \vec{q}_1, \quad (1.23)$$

$$J = \alpha m R^2, \quad J_1 = \alpha_1 m_1 R_1^2. \quad (1.24)$$

Thus  $\vec{q}$  denotes the surface velocity due to spin rotation, and  $\alpha$  describes the internal mass distribution of particles; for homogeneous spherical particles  $\alpha = \alpha_1 = 2/5$ . From Eqs. (1.20) and (1.22) we find

$$\Delta \vec{r} = -\frac{m_1}{m+m_1} \Delta \vec{v}, \quad \Delta \vec{q} = \frac{m_1\alpha_1}{m\alpha+m_1\alpha_1} \Delta \vec{q}_s, \quad (1.25)$$

$$\Delta \vec{r}_1 = \frac{m}{m+m_1} \Delta \vec{v}, \quad \Delta \vec{q}_1 = \frac{m\alpha}{m\alpha+m_1\alpha_1} \Delta \vec{q}_s. \quad (1.26)$$

Inserting these in Eq. (1.21), using  $\vec{r}_1 = \vec{r} + \vec{k}(R+R_1)$  yields

$$\Delta \vec{q}_s = m_{\text{eff}} \left( \frac{1}{m\alpha} + \frac{1}{m_1\alpha_1} \right) \Delta \vec{v} \times \vec{k} \equiv f \Delta \vec{v} \times \vec{k}. \quad (1.27)$$

Here

$$m_{\text{eff}} = \frac{m_1 m}{m + m_1} \quad (1.28)$$

is the effective mass of the pair. In the case of particles with the same internal mass distribution the factor  $f$  reduces to  $f = 1/\alpha$ , which equals  $f = 5/2$  for homogeneous spheres.

The change of the relative velocity at the point of contact can thus be written (from Eq. 1.14)

$$\begin{aligned} \Delta \vec{g} = \vec{g}' - \vec{g} &= \Delta \vec{v} - \Delta \vec{q}_s \times \vec{k} \\ &= \Delta \vec{v} + f \vec{k} \times (\Delta \vec{v} \times \vec{k}). \end{aligned} \quad (1.29)$$

Solving for  $\Delta \vec{v}$  gives

$$\Delta \vec{v} = \Delta \vec{g} \cdot \vec{k} \vec{k} + (1+f)^{-1} \left( \Delta \vec{g} \cdot \vec{k}_T \vec{k}_T + \Delta \vec{g} \cdot \vec{k}_\gamma \vec{k}_\gamma \right), \quad (1.30)$$

and inserting the components of  $\Delta \vec{g}$  which follow from the impact model, Eq. (1.15),

$$\Delta \vec{g} = -(1+\epsilon_n)\vec{g} \cdot \vec{k} \vec{k} + (\epsilon_t - 1)\vec{k} \times (\vec{g} \times \vec{k}) + \epsilon_\gamma \vec{g} \times \vec{k} \quad (1.31)$$

finally gives

$$\begin{aligned} \Delta \vec{v} = & - (1+\epsilon_n)\vec{g} \cdot \vec{k} \vec{k} \\ & - \frac{2}{7} \left[ (1-\epsilon_t)\vec{k} \times (\vec{g} \times \vec{k}) - \epsilon_\gamma (\vec{g} \times \vec{k}) \right]. \end{aligned} \quad (1.32)$$

We have used  $(1+f)^{-1} = \frac{2}{7}$ , the value for homogeneous spheres. From Eq. (1.27) we obtain

$$\Delta \vec{q}_s = \frac{5}{7} \left[ (1-\epsilon_t)(\vec{g} \times \vec{k}) + \epsilon_\gamma (\vec{k} \times (\vec{g} \times \vec{k})) \right]. \quad (1.33)$$

The changes for the individual particles are now obtained from Eqs. (1.25). Note that in the case with no friction ( $\epsilon_t = 1$ ) nor irregularity ( $\epsilon_\gamma = 0$ ), the changes of velocity are independent from spins and no change of spins occurs.

### 1.3.1.2 Energy dissipation

The total kinetic energy of a colliding pair of particles consists of translational and rotational parts

$$E = E_{kin} + E_{rot} = \frac{1}{2}(m\dot{\vec{r}}^2 + m_1\dot{\vec{r}}_1^2) + \frac{1}{2}(m\alpha\vec{q}^2 + m_1\alpha_1\vec{q}_1^2) \quad (1.34)$$

With the centre of mass velocity

$$\vec{v}_c = \frac{m\dot{\vec{r}} + m_1\dot{\vec{r}}_1}{m+m_1}, \quad (1.35)$$

the translational part can be written as

$$E_{kin} = \frac{1}{2} \left( (m+m_1)\vec{v}_c^2 + m_{\text{eff}}\vec{v}^2 \right), \quad (1.36)$$

and since  $\vec{v}_c$  is conserved,

$$\Delta E_{kin} = \frac{1}{2} m_{\text{eff}} \Delta(\vec{v}^2) \quad (1.37)$$

The rotational contribution can be decomposed in a similar manner by defining

$$\vec{q}_c = \frac{m\alpha \vec{q} - m_1\alpha_1 \vec{q}_1}{m\alpha + m_1\alpha_1}, \quad (1.38)$$

leading to

$$E_{rot} = \frac{1}{2} \left[ (m\alpha + m_1\alpha_1)\vec{q}_c^2 + \frac{m_{\text{eff}}}{f} \vec{q}_s^2 \right]. \quad (1.39)$$

Since  $\vec{q}_c$  is conserved, we have

$$\Delta E_{rot} = \frac{1}{2} \frac{m_{\text{eff}}}{f} \Delta(\vec{q}_s^2), \quad (1.40)$$

As  $\Delta \vec{q}_s = f \Delta \vec{v} \times \vec{k}$ , the total energy change is



$$\begin{aligned}\Delta E &= \frac{1}{2}m_{\text{eff}} \left[ 2\vec{v} \cdot \Delta\vec{v} + (\Delta\vec{v})^2 + 2\Delta\vec{v} \times \vec{k} \cdot \vec{q}_s + f(\vec{k} \times \Delta\vec{v})^2 \right] \\ &= \frac{1}{2}m_{\text{eff}} \left[ 2\vec{g} \cdot \Delta\vec{v} + (\Delta\vec{v})^2 + f(\vec{k} \times \Delta\vec{v})^2 \right].\end{aligned}\quad (1.41)$$

Inserting  $\Delta\vec{v}$  from Eq.(1.30) gives

$$\Delta E = -\frac{1}{2}m_{\text{eff}} \left[ \Delta(g_n^2) + \frac{1}{1+f}\Delta(g_t^2) \right], \quad (1.42)$$

where  $g_n \equiv |\vec{g} \cdot \vec{k}|$  and  $g_t \equiv |\vec{k} \times (\vec{g} \times \vec{k})|$ . In terms of the impact model we find

$$\begin{aligned}\Delta E &= -\frac{1}{2}m_{\text{eff}} \left[ (1 - \epsilon_n^2)g_n^2 \right. \\ &\quad \left. + \frac{1}{1+f} \left( 1 - (\epsilon_t + \epsilon'_\gamma)^2 - \epsilon_\gamma'^2 \right) g_t^2 \right],\end{aligned}\quad (1.43)$$

where we have also explicitly included the random component  $\epsilon'_\gamma$  present in  $\epsilon_t$ . Note that the factor  $\frac{1}{1+f}$  enters by including the exchange of energy between rotational and translational motions. The use of  $\epsilon_t$  to account for friction without including particle spins, would correspond to setting  $f = 0$ , thus leading to incorrect amount of dissipation.

### 1.3.1.3 Surface irregularities

In principle, irregularities can be described in terms of  $\epsilon_\gamma$ , but this treatment has some caveats. Namely, a realistic impact model must have  $\Delta E \leq 0$ . With  $\epsilon_\gamma = \epsilon'_\gamma = 0$  the energy change implied by Eq. (1.43) is guaranteed to be negative for all  $0 < \epsilon_n < 1, -1 < \epsilon_t < 1$ , but if irregularity is included, the allowed range of  $\epsilon_\gamma$  and  $\epsilon'_\gamma$  depends on  $\epsilon_n$ ,  $\epsilon_t$ , and the ratio  $g_n/g_t$ . This makes it hard to interpret the physical meaning of the model. An alternative description for small-scale irregularity was introduced in Salo (1987a,b), where the actual normal vector of the impact plane,  $\vec{k}^*$ , is allowed to deviate from  $\vec{k}$  by a small random amount in each impact,

$$\vec{k}^* = \vec{k} \sqrt{1 - \gamma_a^2 - \gamma_b^2} + \gamma_a \vec{k}_T + \gamma_b \vec{k}_\gamma, \quad (1.44)$$

where  $\gamma_a$  and  $\gamma_b$  are random variables with zero mean, and using

$$\Delta\vec{g} = -(1 + \epsilon_n)\vec{g} \cdot \vec{k}^* \vec{k}^* + (\epsilon_t - 1)\vec{k}^* \times (\vec{g} \times \vec{k}^*). \quad (1.45)$$

On the other hand, the overall shape of the particles is assumed to stay close to spherical, so that Eq. (1.14) can still be used for the relative velocity at the contact point. The advantage of this description is that the variables  $\gamma_a$  and  $\gamma_b$  have an obvious physical interpretation, and a negative energy loss is guaranteed for any allowed impact with  $\vec{k}^* \cdot \vec{v} < 0$ .

### 1.3.1.4 Rotating frame

The calculations presented above are valid in an inertial frame. When using a rotating frame, with same instantaneous axis directions, the velocities and spins are connected to their inertial frame values as

$$\begin{aligned}\dot{\vec{r}}_I &= \dot{\vec{r}}_n + \vec{n} \times \vec{r}_I, \\ \vec{\omega}_I &= \vec{\omega}_n + \vec{n},\end{aligned}\quad (1.46)$$

where subscripts  $I$  and  $\Omega$  are used to distinguish between the two frames. On the other hand, the instantaneous direction vectors are unaffected. Thus the only differences to Eqs. (1.32) and (1.33) for  $\Delta\dot{\vec{r}}$  and  $\Delta\vec{\omega}$  would come through  $\vec{g} = \vec{v} - (R_1\vec{\omega}_1 + R\vec{\omega}) \times \vec{k}$ . However, as

$$\begin{aligned}\vec{v}_I &= \vec{v}_\Omega + \vec{n} \times \vec{k}(R + R_1), \\ (R\vec{\omega} + R_1\vec{\omega}_1)_I \times \vec{k} &= (R\vec{\omega} + R_1\vec{\omega}_1)_\Omega \times \vec{k} \\ &\quad + (R + R_1)\vec{n} \times \vec{k},\end{aligned}\quad (1.47)$$

the vector  $\vec{g}$  has the same expression in both frames. Thus no modifications are needed if both, velocities and spins, are treated consistently. Alternatively, we may use  $\vec{\omega}_I$  in the collisional equations and add a correction term  $(R + R_1)\vec{n} \times \vec{k}$  to  $\vec{g}_\Omega$ , as was done in Hämeen-Anttila and Salo (1993).

### 1.3.2 Force model for impacts

The treatment of impacts in terms of instantaneous velocity changes leads to problems if the particles do not separate after the impact. Even in the absence of mutual gravity, a situation can occur where the particles' have a net central acceleration toward each other even when their post-collisional relative velocity is zero. This corresponds to a sliding motion of the particles, before they are eventually separated by the shear. Following Wisdom and Tremaine (1988) such a phase is convenient to handle with a succession of small jumps, achieved by setting  $\epsilon_n = 1$  whenever the perpendicular impact velocity falls below a threshold value, say,  $0.01nR$ . Since such impacts do not dissipate much energy to start with, the energy balance of the system is not affected by this replacement.

However, the problem becomes more severe if self-gravity or cohesive forces between particles are included. In these cases impacts may lead to a semi-permanent physical sticking of particles. In the instantaneous impact method this leads to particle overlaps, unless some special measure is applied to force a separation of the particles. Further difficulties may still arise for example if gravitational aggregates are formed, in which case it is insufficient to consider only binary impacts independently from each other. A physically motivated solution, which is also computationally feasible, is to include explicitly the pressure forces affecting the particles in the impact. In Salo (1995) this was done in terms of the linear visco-elastic model originally developed by Dilley (1993) for the theoretical parameterisation of his measurements of velocity and size-dependent elasticity. Likewise, frictional forces may be included in the simulations (Salo, 1995; Morishima and Salo, 2006). Such *Discrete element method (DEM)* algorithms (Cundall and Strack, 1979) are commonly used in granular dynamics (see e.g. Pöschel and Schwager (2005)).

The equations of motion for the impacting particles are

$$\begin{aligned}m\ddot{\vec{r}} &= \vec{F}^{imp} + \vec{F}, \\ m_1\ddot{\vec{r}}_1 &= \vec{F}_1^{imp} + \vec{F}_1,\end{aligned}\quad (1.48)$$

$$\begin{aligned}J\dot{\vec{\omega}} &= R\vec{k} \times \vec{F}^{imp}, \\ J_1\dot{\vec{\omega}}_1 &= R_1(-\vec{k}) \times \vec{F}_1^{imp},\end{aligned}\quad (1.49)$$

where  $\vec{F}_1^{imp} = -\vec{F}_1^{imp}$  represent the impact forces, and  $\vec{F}$  and  $\vec{F}_1$  include additional forces affecting the particles (central force and gravity of other particles), not causing any torque on the impacting pair. Let us express the impact force as

$$\vec{F}_1^{imp} = f_N \vec{k} + f_T \vec{k}_T \quad (1.50)$$

with the normal force (the tangential force  $f_T$  will be treated below)

$$\begin{aligned} f_N(\xi) &= \beta_1 \xi + \beta_2 \dot{\xi}, & \xi > 0 \\ &= 0, & \xi \leq 0, \end{aligned} \quad (1.51)$$

where

$$\xi = R + R_1 - |\vec{r} - \vec{r}_1| \quad (1.52)$$

is the penetration depth during the impact. Here  $\beta_1 > 0$  is the spring constant of the restoring harmonic force, while due to the dissipative term with  $\beta_2 > 0$  the energy stored during the compression phase is not completely returned in the rebound phase. From Eqs. (1.48), (1.51) and (1.52),

$$\begin{aligned} \dot{\xi} &= -\vec{v} \cdot \vec{k}, \\ \ddot{\xi} &= -\vec{v} \cdot \vec{k} - \vec{v} \cdot \dot{\vec{k}}, \\ \ddot{\vec{v}} &= (\vec{F}/m - \vec{F}_1/m_1) + \vec{F}_1^{imp}/m_{\text{eff}}, \end{aligned} \quad (1.53)$$

which yields

$$\ddot{\xi} = -\frac{(\beta_1 \xi + \beta_2 \dot{\xi})}{m_{\text{eff}}} + C, \quad (1.54)$$

with

$$C = \left( \frac{\vec{F}_1}{m_1} - \frac{\vec{F}}{m} \right) \cdot \vec{k} - \vec{v} \cdot \dot{\vec{k}}, \quad (1.55)$$

where  $C$  contains the difference of additional accelerations felt by the particles, as well as the change of the normal direction during the impact.

Ignoring the term  $C$ , the solutions of Eq. (1.54) are exponentially damped oscillations (impact starts at  $t = 0$  when  $\xi = 0$ ),

$$\xi = \frac{v_n}{\omega} \exp(-\omega_d t) \sin(\omega t) \quad (1.56)$$

where  $v_n \equiv \dot{\xi}(0)$ , and the oscillation frequency  $\omega$  and the damping rate  $\omega_d$  are

$$\begin{aligned} \omega^2 &= \omega_0^2 - \omega_d^2, \\ \omega_0^2 &= \frac{\beta_1}{m_{\text{eff}}}, \\ \omega_d &= \frac{1}{2} \frac{\beta_2}{m_{\text{eff}}}, \end{aligned} \quad (1.57)$$

with  $\omega_0$  denoting the undamped frequency. The duration of the impact (the length of the first half-cycle) and the coefficient of restitution are

$$\begin{aligned} T_{\text{dur}} &= \pi/\omega \approx \pi/\omega_0 \\ \epsilon_n &= -\frac{\dot{\xi}(T_{\text{dur}})}{\dot{\xi}(0)} = \exp\left(-\pi \frac{\omega_d}{\omega}\right) \end{aligned} \quad (1.58)$$

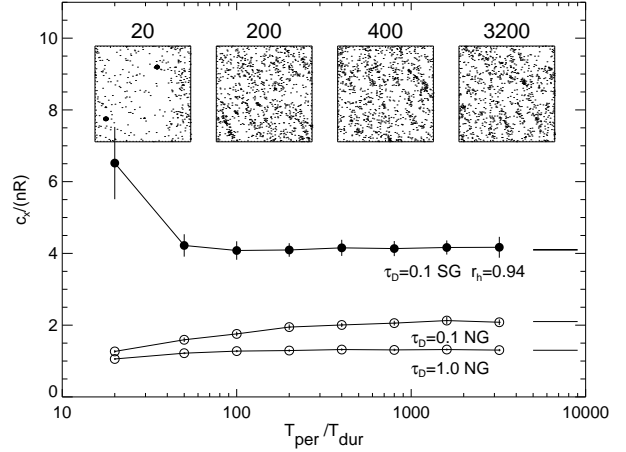


**Figure 1.4** The steady-state velocity dispersion in force-method simulations using different impact duration  $T_{\text{dur}}$ . Results with instantaneous impact method are indicated by the horizontal lines. A constant  $\epsilon_n = 0.5$  is used. In the non-gravitating simulation (NG) elongation of impact duration ( $T_{\text{per}}/T_{\text{dur}} \lesssim 100$ ) enhances dissipation, resulting in a lower velocity dispersion. In self-gravitating simulations (SG) this extra dissipation is compensated by the enhanced energy gain due to gravitational viscosity for ( $T_{\text{per}}/T_{\text{dur}} \lesssim 50$ ), caused by the longer time the particles spend in the vicinity of each other. For long enough  $T_{\text{dur}}$  the particles may even stick together, leading to strongly enhanced gravitational viscosity. The inserts show snapshot from the self-gravitating simulations with different  $T_{\text{per}}/T_{\text{dur}}$  ratios.

Thus specifying  $\beta_1/m_{\text{eff}}$  gives the approximate impact duration, and then  $\beta_2$  is determined by  $\epsilon_n$ ,

$$\frac{\beta_2}{m_{\text{eff}}} = \frac{2\omega_0}{\sqrt{\left(\frac{\pi}{\ln \epsilon_n}\right)^2 + 1}}. \quad (1.59)$$

Note that a velocity-dependent elasticity law  $\epsilon_n(v_n)$  can also be used in simulations: in this case the value of  $\beta_2$  is chosen for each impact based on the pre-impact relative velocity  $v_n$  of the pair and the desired  $\epsilon_n$ .

In the force method the particle motion is integrated through the impact, so that the time step is basically determined to be a small fraction of  $T_{\text{dur}}$ . On the other hand, the total span of any simulation is determined by the orbital time-scale  $T_{\text{per}} = 2\pi/n$ . Since the physical  $T_{\text{dur}} \ll T_{\text{per}}$ , it is advantageous to speed up the calculations by scaling the simulated impact duration to be larger than the physical duration. Otherwise most of the computing time would be spent on calculating the motion of particles which are not currently colliding with much smaller steps than required to resolve their motion due tidal and self-gravitational forces. Indeed, the most attractive feature of the above linear force model is that the impact duration is independent of impact velocity, and is easily adjusted via  $\beta_1$ .

However, there is an upper limit for the allowed  $T_{\text{dur}}$ , as the solution obtained above ignored the term  $C$ : preserving this term may change the implied elasticity. Likewise, the maximum penetration in impacts  $\xi_{\text{max}} \approx (v_n/\pi)T_{\text{dur}}$  should not be too large compared to the particle size. Also,

if the impact duration is extended to  $T_{dur} > 1/\omega_c$ , where  $\omega_c$  is the impact frequency, the binary nature of collisions is not retained. It is thus important to address what is the maximum  $T_{dur}$  one can use. According to simulation tests (see Fig. 1.4), using  $T_{dur}/T_{per} < 10^{-2}$  leads to a practically same steady state as the instantaneous impact method. Most of the simulations of Sect. 1.6.2 use  $\omega_0/n = 400$ , corresponding to  $T_{dur}/T_{per} = 1/800$ . In this case  $\xi_{max}/R$  is typically of the order of  $10^{-3}$ .

### 1.3.2.1 Surface friction

A straightforward way to include friction to the force model is to use

$$f_T = \mu f_N \quad (1.60)$$

in Eq. (1.51), where  $\mu < 0$  denotes the coefficient of friction. This description is quite different from using  $\epsilon_t$  in the instantaneous impact model, as there is no single choice of  $\mu$  that would corresponds to a given  $\epsilon_t$ . To connect  $\mu$  to  $\epsilon_t$ , we write  $\vec{g}$  in terms of Eqs. (1.48) and (1.49) as

$$\begin{aligned} \vec{g} &= \vec{v} - (R_1 \dot{\vec{\omega}}_1 + R \dot{\vec{\omega}}) \times \vec{k} \\ &= \frac{1}{m_{\text{eff}}} \left( \vec{F}_1^{imp} + f \vec{k} \times (\vec{F}_1^{imp} \times \vec{k}) \right) \\ &= \frac{1}{m_{\text{eff}}} \left( f_N \vec{k} + (1 + f)\mu f_N \vec{k}_T \right), \end{aligned} \quad (1.61)$$

where  $f$  is the factor defined in connection to Eq. (1.29), reducing to 5/2 for homogeneous spheres; we have ignored here the extra forces due to orbital motion and self-gravity ( $C = 0$ ). Thus, the total change of normal and tangential velocity difference are

$$\begin{aligned} \Delta g_n &= \Delta \vec{g} \cdot \vec{k} = \int_{T_{dur}} \frac{f_N}{m_{\text{eff}}} dt \equiv (1 + \epsilon_n) g_n, \\ \Delta g_t &= \Delta \vec{g} \cdot \vec{k}_T = \frac{7}{2} \mu \int_{T_{dur}} \frac{f_N}{m_{\text{eff}}} dt \equiv (\epsilon_t - 1) g_t, \end{aligned} \quad (1.62)$$

where the force model results are identified with those of the instantaneous impact model. Thus

$$\epsilon_t = 1 + \frac{7}{2} \mu (1 + \epsilon_n) g_n / g_t \quad (1.63)$$

implying  $\epsilon_t \leq 1$  since  $\mu < 0$ . Nevertheless, the regime  $\epsilon_t < 0$  can not be modeled, as the frictional force acts against the relative tangential contact velocity. In practice, if friction is strong enough to suppress the tangential velocity difference,  $g_t = 0$  appears as a discontinuity in the force and the solution oscillates around  $\epsilon_t = 0$ .

In principle, more realistic theoretical models for both friction and normal restitution (Spahn et al., 1995) can also be used in simulations, but then the various scalings become more complicated, as the impact duration will generally depend on the impact velocity.

### 1.3.3 Search of impact pairs

The speed of the collisional simulation depends crucially on the efficient search of impact pairs. For example, in their simulations of non-gravitating particles Wisdom and Tremaine

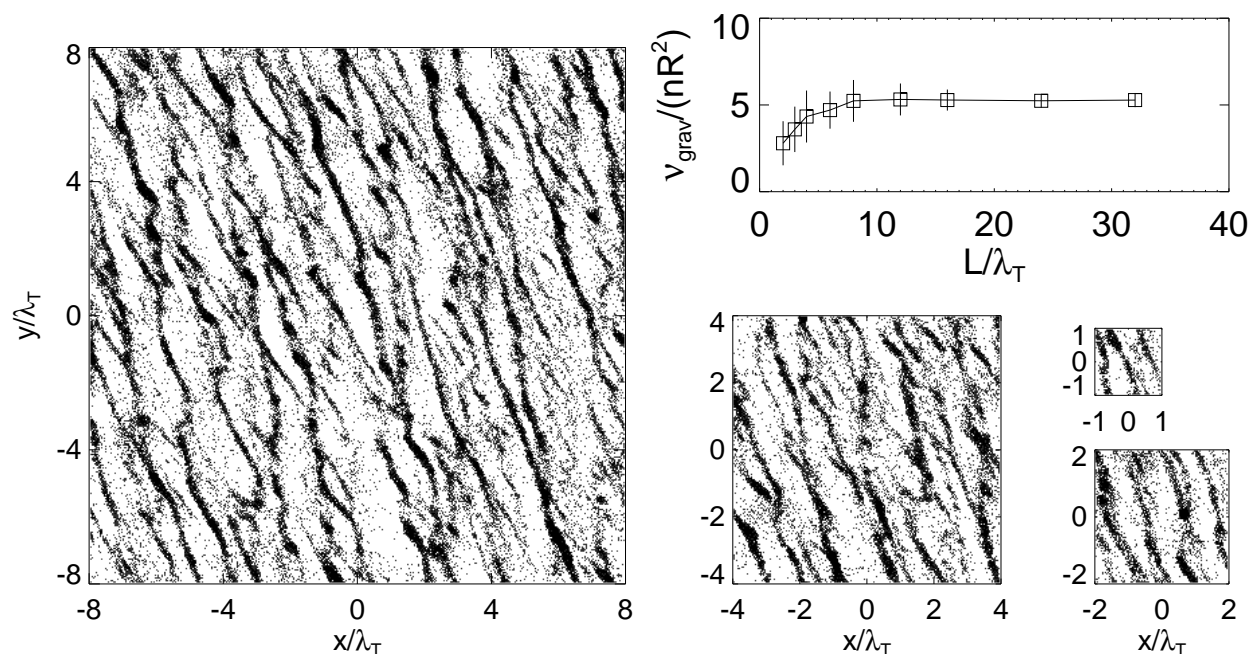
(1988) used the fact that orbits between impacts are Keplerian epicycles, and solved iteratively for the intersection time of each pair of epicycles. The impact of the pair with the smallest impact time was executed with instantaneous velocity changes, and the post-impact orbital elements were calculated, leading to updated intersection times with all the other particles. The system was thus moved on from one impact to the next (the method is called “event-driven”). Similar methods were used also in the early simulations of rarefied azimuthally complete rings: due to extremely long intervals between impacts elaborate schemes were developed for detecting orbital intersections taking place after even several hundreds of synodic periods (Hämeen-Anttila and Lukkari, 1980).

Event-driven methods are fairly fast for small particle numbers ( $N \approx 50$  in Wisdom and Tremaine (1988)), but as  $N$  increases, the checking of next orbital intersections between all  $N(N-1)/2$  pairs gets excessively slow. Also, the inclusion of additional forces besides the central gravity poses problems. Therefore, in the self-gravitating case the equations of motions are integrated with small time steps, and the potential intersections during each step are searched only among the neighboring particles. Similar stepwise time integration is advantageous also in the case of high particle density and large  $N$ , even if self-gravity is not included. Provided that the step size is small, the distances between particles can be expanded as a second-order Taylor polynomial, providing a fast method for constructing a list of potential impacts during the step (Salo, 1991). From this list, the impacts during the time step are then executed as in the event-driven method.

Regardless of the time-advancement method a considerable speedup can be achieved if the number of pairs examined for potential impacts is kept as small as possible. This can be done quite efficiently by keeping track of the maximum pre-step separation which has actually led to an impact during previous steps, and by checking in each step only those pairs whose distance does not exceed this maximum, multiplied by some threshold factor. This threshold must be chosen in a manner which ensures that no impacts are lost, and it also must be dynamically adjusted as the velocity dispersion of the system evolves. A useful trick is to sort the particles according to their radial coordinate and choose first only pairs whose radial distances fall below the threshold. In the optimal case, the number of pairs examined is proportional to  $\frac{c}{nR} N$ . Note that the actual orbital integration needs not to be performed by a Taylor-series: for example in Salo (1995) a fourth order Runge-Kutta integration was utilized, and the impact locations initially estimated by the second-degree polynomial expansion were iteratively improved to correspond to the full accuracy of the integration.

It must be stressed that it is important to take correctly into account impacts taking place over boundaries of the local calculation region. For small calculation regions this fraction can be quite significant, and the omission of such impacts will considerably modify the energy balance, and thus, all steady-state properties of the system. Also, if the force method is used, even a single non-detected impact may





lead to large injection of energy to the system if it happens to lead to a deep overlap on the next step. However, such a situation is easy to detect by monitoring the  $\xi_{max}$  during the simulation.

## 1.4 Calculation of self-gravity

### 1.4.1 Force evaluation

Inclusion of gravitational forces increases the computational burden significantly, as in principle the forces between each particle pair need to be included (as well as to account for the contribution of the replicas of the local calculation region). Moreover, self-gravity typically enhances the velocity dispersion and increases the impact frequency (see Section 1.6). Both factors make the collisional calculations more time consuming. These problems are especially pronounced in the case of a weak tidal field, i.e. far from the planet, when gravitationally bound particle aggregates form. Proper simulation of self-gravity also sets additional constraints for the required minimum size of the calculation region, since it must exceed the scale of the self-gravity wake structures formed via gravity (roughly of the order of Toomre critical wavelength  $\lambda_T$ , see Fig 1.5). In practice this means using at least  $10^4 - 10^5$  simulation particles. On the other hand, for non-gravitating spatially uniform systems a fairly modest particle number ( $10^2 - 10^3$ ) is usually sufficient to give the steady-state properties with a good accuracy.

The most straight-forward way of force evaluation is the *particle-particle* (PP) method, using a direct summation over particle pairs. The obvious advantage is that no approx-

**Figure 1.5** Snapshots of self-gravitating simulations with different sized calculation regions, after 50 orbital periods. In each simulation  $\tau_D = 0.5$ ,  $\epsilon_n = 0.5$ ,  $\rho = 900 \text{ kg/m}^3$ ,  $R = 1\text{m}$ , and  $a = 100,000 \text{ km}$  ( $r_h = 0.82$ ). The width of the square-shaped region is  $L/\lambda_T = 32, 16, 8, 4, 2$ . In physical units the Toomre critical wavelength  $\lambda_T = 41.6\text{m}$ . The self-gravity is calculated from all particles within a cylindrical radius  $\Delta_{max} = L/2$ . Gravitational forces from within  $\Delta_{min} = 0.25\lambda_T$  are calculated with the PP-method and beyond that with the PM-method, using a grid spacing of  $\lambda_T/16$ . The graph shows the gravitational viscosity (Eq. 1.87) as a function  $L/\lambda_T$  (average between 25-50 orbits).

imations are involved, the gravitational field corresponding exactly to that implied by the particle ensemble. The method can also be fairly efficient (Daisaka et al., 2001) when using a special-purpose processor, like GRAPE, with a hardware calculation of gravity forces (Makino and Fujimoto, 1993). With standard-type processors the implied  $N^2$  time consumption becomes however prohibitively large already for a few thousand particles, so that other methods are needed. Also, due to partial cancellation of distant forces it is in fact unnecessary to calculate the contribution from distant particles with the same accuracy as that of the nearby particles.

This fact is utilized in *hierarchical tree-codes*, where the distant particles are grouped together in force calculation, so that only few low order moments of their distribution are included (see e.g. the galaxy simulation codes described in Barnes and Hut, 1986; Hernquist and Katz, 1989). The essential part of the method is the efficient construction of the connected particle lists ('tree'), leading to a  $N \ln N$  dependence of the CPU-time consumption. Richardson (1994) first applied this method to self-gravitating rings. On the other hand, N-body simulations of galactic dynamics often employ

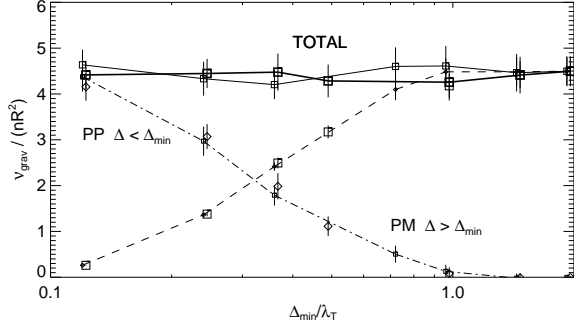


**Figure 1.6** The near (PP) and far (PM) contributions to self-gravity, measured in terms of gravitational viscosity, are compared for different dividing distances  $\Delta_{min}$ . Simulation parameters are the same as in the previous figure, and the total extent of the simulation region is  $4\lambda_T \times 4\lambda_T$ . The rightmost point corresponds to using solely PP method. Two set of simulations are shown, with  $\lambda_T/16$  (thin lines, small symbols) and  $\lambda_T/32$  (thick lines, large symbols) PM grid spacing. Within error bars, the total gravitational viscosity is the same in all simulations.

*particle-mesh* (PM) method (see Sellwood, 2014): the density of the system is tabulated in a regular mesh, and the forces (or gravity potential) at each mesh location are evaluated by convolving the density with the interaction law, and then interpolating to the particle locations. The speed of the method relies on the use of a Fast Fourier Transform for performing the force convolution, and in the optimal case the CPU-time consumption of gravity calculations is determined mainly by the interpolation of forces, being linear in  $N$ . In current large-scale cosmological simulations the tree and PM methods are often combined (Springel, 2005).

The important difference between planetary rings and galaxy disks is that binary gravitational encounters between ring particles are not insignificant compared to the mean gravitational field (rings are not ‘collisionless’). Therefore the smoothing of forces implied by the gravity mesh (or by explicit gravity softening) is incorrect. On the contrary, the most important contributions from self-gravity come from the fluctuating gravitational forces exerted by the nearest neighboring ring particles (within  $\sim \lambda_T$ , see Fig. 1.7).

An obvious way to speed up the calculations, while retaining the accurate treatment of nearby gravity encounters, is to combine PP and PM methods, for example in a manner that was employed in Salo et al. (2001). In this treatment the gravitational force exerted on each particle is divided in a nearby and distant contribution,

$$\vec{F}_i = \vec{F}_i^{near} + \vec{F}_i^{far},$$

$$\vec{F}_i^{near} = G \sum_{\Delta_{ij} < \Delta_{min}} m_j \frac{\vec{r}_j - \vec{r}_i}{|\vec{r}_j - \vec{r}_i|^3}, \quad (1.64)$$

$$\vec{F}_i^{far} = G \int_{\Delta > \Delta_{min}} \rho(\vec{r}) \frac{\vec{r} - \vec{r}_i}{|\vec{r} - \vec{r}_i|^3} d^3r, \quad (1.65)$$

where  $\Delta$  denotes the projected 2D distance in the xy-plane. The near contribution is calculated by direct particle-particle summation, in order to include accurately the effects of close gravitational encounters, as well as the gravitational sticking of particles. Typically  $\Delta_{min} \ll L_x, L_y$ , so that just a few percents of all  $N(N-1)/2$  particle pairs are involved. The latter, usually smaller distant contribution is calculated with a particle-mesh method.

An efficient way to calculate the PM contribution is to use FFT in a sheared coordinate system, defined by the transformation

$$\begin{aligned} u &= x, \\ v &= y - tsx \mod L_y, \end{aligned} \quad (1.66)$$

where  $t$  is the time since the beginning of the simulation and  $s = -\frac{3}{2}n$  in the Keplerian case. In these coordinates the Eqs. (1.8) for the image particles transform into

$$\begin{aligned} u' &= u + nL_x, \\ v' &= v + mL_y. \end{aligned} \quad (1.67)$$

indicating that the system is double periodic in the planar directions. We define a 3D Cartesian mesh with  $m_u \times m_v \times m_z$  cells, and tabulate the mass  $\delta m(u, v, z)$  in each cell by a cloud-in-cell (CIC) assignment. In planar directions the mesh has the same size as the calculation region,  $|u| < L_x/2, |v| < L_y/2$ . The vertical coverage of the mesh,  $|z| < L_z/2$  can be either a constant, or varied according to the vertical thickness of the system, using  $L_z/2 = k\sqrt{z^2}$ , for example with  $k = 3$ : the small fraction of particles with  $|z| > L_z/2$  contribute insignificantly to the total density and can be ignored. The force on each cell center is obtained with a convolution

$$\vec{F}_{i,j,k} = G \sum_{l,m,n} \delta m_{l,m,n} \vec{\Gamma}_{l-i,m-j,n-k} \quad (1.68)$$

where  $\vec{\Gamma}$  (with same number of elements as  $\delta m$ ) denotes the Green function for the gravitational interaction between the cells. Written in terms of the newly defined coordinates,

$$\vec{\Gamma}_{abc} = [a\Delta u, b(\Delta v + st\Delta u), c\Delta z] / d_{abc}^3 \quad (1.69)$$

with

$$d_{abc} = \left[ (a\Delta x)^2 + (b(\Delta v + st\Delta u))^2 + (c\Delta z)^2 \right]^{1/2}. \quad (1.70)$$

To exclude the near contribution  $\vec{\Gamma}_{abc}$  is set to zero for  $(a\Delta x)^2 + (b(\Delta v + st\Delta u))^2 < \Delta_{min}^2$ .

If carried out by direct summation, the convolution in Eq. (1.68) would require  $\propto (m_x m_y m_z)^2$  operations. Even for moderate spatial resolution this would mean an excessive number of calculations (even larger than that for the direct summation over all  $N(N-1)/2$  pairs). It is therefore essential to utilize the Fourier convolution theorem, according to which the inverse transform of mesh forces equals the product of the inverse transforms of density and Green function,

$$\vec{F}_{i,j,k} = \widetilde{\delta m}_{l,m,n} \vec{\Gamma}_{l-i,m-j,n-k}. \quad (1.71)$$

In order to be able to apply the convolution theorem, we double the mesh size in the vertical direction, padding

the extra cells with zeros. Using Fast Fourier Transform, the number of calculations becomes proportional to  $(m_x \ln m_x)(m_y \ln m_y)(2m_z \ln 2m_z)$ , making the method feasible. The forces at the particle locations are interpolated from the grid, with the same CIC-assignment as in the tabulation of density. The forces on the few particles with  $|z| > L_z/2$  are calculated with an extrapolation from the grid. In this manner the force on each particle is due to the density in the region which corresponds in size to the whole original rectangular calculation region (see Fig. 1.3). If a circular region is desired (to avoid any artificial 'polarization' of forces due to corners of the region) we can set the  $\Gamma_{abc}$  to zero beyond some distance  $\Delta_{max} (< \max\{L_x/2, L_y/2\})$ .

Figure 1.6 shows the gravitational viscosity (Eq. (1.87)) from  $4\lambda_T \times 4\lambda_T$  simulations where different dividing distances  $\Delta_{min}$  between PP and PM methods are used, confirming that similar results are obtained in all cases. However, the gravity calculation is about 10 faster when using PP+PM with  $\Delta_{min}/\lambda_T = 1/8$  in comparison with using just the PP method to calculate gravity from within  $2\lambda_T$ . For larger calculation regions and particle numbers, the gain in speed becomes even more important.

#### 1.4.2 Approximate treatments of self-gravity

Fully self-consistent calculation of particles' mutual gravity, as described above, is quite CPU time intensive. Wisdom and Tremaine (1988) devised a simple method for mimicking self-gravity in terms of an enhanced vertical frequency  $n_z > n$  in the dynamical equations. They estimated the vertical self-gravity inside the ring layer from Poisson's equation,

$$F_{sg}(z) = -2\pi G \int_{-z}^z \rho(z') dz' = -\frac{4\pi G \Sigma}{H} z, \quad (1.72)$$

where the ring is approximated with a homogeneous infinite layer with a vertical half-thickness  $H$ . Combining with the vertical component of the central field,  $F_c = -n^2 z$ , gives

$$F_z(z) = -(n^2 + \frac{4\pi G \Sigma}{H}) z \equiv -n_z^2 z \quad (1.73)$$

Most of their simulations used a constant  $n_z/n = 3.6$ , which corresponds to  $F_{sg}/F_c \approx 12$ , assumed to approximate the enhancement in vertical gravity due self-gravity in the dense B-ring of Saturn. Such a treatment mimics qualitatively quite well the effects of vertical gravity, like the enhanced impact frequency (see Sect. 1.6), which leads to strongly increased non-local viscosity, thus promoting viscous overstability. Indeed, the use of  $n_z/n > 1$ , even if not realistic for exploring the full effects of self-gravity, is a useful method when analyzing overstability in terms of hydrodynamic transport coefficients evaluated from N-body simulations (Salo et al., 2001; Schmidt et al., 2001). Nevertheless, since the approximation ignores the planar components of gravity, which are responsible for the emergence of self-gravity wakes, it is questionable how useful it is for describing real systems in any quantitative way. Also, the originally used enhancement factor 3.6 is likely to overestimate the vertical field considerably, since it is based on space density  $\rho_s = \Sigma/(2H) = 400 \text{ kg/m}^3$  inside the ring layer (Wisdom and Tremaine, 1988).

For example, with the current estimate  $\Sigma \approx 700 \text{ kg/m}^2$  (Hedman and Nicholson, 2016) this would correspond to  $H \approx 1$  meters.

Another useful approximation can be applied to the calculation of axisymmetric component of self-gravity, in terms of a superposition of infinite plane waves. We first make a radial Fourier decomposition of the tangentially averaged surface density

$$\Sigma(x) = \Sigma_0 \left[ 1 + \sum_{m=1}^{\infty} A_m \cos \left( m \frac{2\pi}{L_x} (x - x_m) \right) \right], \quad (1.74)$$

where  $A_m$  and  $x_m$  are the fractional amplitude and phase of different m-components with wavelengths  $\lambda = L_x/m$ . We then treat each component as an infinite plane wave, and use Poisson equation for an infinite 2D sheet to calculate the corresponding radial force. Superposition of modes with different  $m$  gives

$$F_x(x) = -2\pi G \Sigma_0 \sum_{m=1}^{m_{max}} A_m \sin \left[ m \frac{2\pi}{L_x} (x - x_m) \right]. \quad (1.75)$$

A finite  $m_{max}$  is used in order to suppress small scale noise. Such a treatment was applied in Salo and Schmidt (2010) to compare viscous instability in N body simulations to Schmit and Tscharnuter (1995) hydrodynamic predictions in the case axisymmetric self-gravity is included.

#### 1.4.3 Time integration

In the force method the basic timestep of integration is determined by the need to resolve the rebound of individual particle pairs. Depending on the chosen spring constant of the restoring harmonic force, this requires time step of the order of  $\Delta T_{imp} = (0.01 - 0.1) T_{dur} \sim (10^{-4} - 10^{-5}) T_{orb}$ , where  $T_{dur}$  is the impact duration. On the other hand, self-gravitational forces are practically constant over such sort time scales. To speed up calculations, one can therefore use a larger time step, say  $\Delta T_{grav} \sim 10^{-3} T_{orb}$ , for updating the gravity forces. This simple method works well in the case of gravity wake structures: the errors made in keeping the self-gravity constant tend to cancel each other on the average. However, when particles stick physically, this method may lead to artificial destabilization of gravity aggregates via rotational instability (Karjalainen and Salo, 2004). This is solely a numerical artifact, rising from the fact that then the force integration errors do not cancel each other, but lead to a net torque on particles attached to the aggregate. As illustrated in Karjalainen and Salo (2004) a totally sufficient remedy is to calculate both the forces and their time derivatives at the beginning of each gravity step, and then apply linear extrapolation of self-gravity during the step.

### 1.5 Extracting quantities from simulations

The fundamental<sup>2</sup> quantity describing both the dynamics and observed structures of Saturn's rings is the dynamical (geometric) optical depth, defined as the total surface area of particles divided by the total area. For identical particles with radius  $R$

$$\tau_D = \frac{N\pi R^2}{L_x L_y}. \quad (1.76)$$

One of the main advantages of the local method is that the optical depth (and surface density in case of self-gravitating particles) of the system is fixed. Thus, after the establishment of local energy balance, all dynamical properties characterizing the steady-state corresponding to this  $\tau_D$  can be obtained with an arbitrary accuracy, by time averaging over sufficiently long time intervals over all particle orbits and impacts. The efficiency of time averaging was strikingly demonstrated in Wisdom and Tremaine (1988), who made a practically complete study of identical, non-gravitating particles, up to  $\tau_D \sim 3$ , using experiments with only  $N = 50$  particles.

#### 1.5.1 Steady-state quantities

The interesting dynamical quantities include the impact frequency  $\omega_c$ , the velocity dispersion tensor  $\hat{C}_{\alpha\beta}$ , the pressure tensor  $\hat{P}_{\alpha\beta}$  and shear viscosity  $\eta = -\frac{1}{s}\hat{P}_{xy}$ . Other important properties are the geometric thickness  $H$ , and the volume filling factor  $D_3(z)$ , useful for connecting the dynamical estimates to photometric observations of rings. The steady-state values of all these quantities are determined by the optical thickness of the system  $\tau_D$ , the size distribution of particles  $n(R)$ , and by their internal density  $\rho$  and elastic properties  $\epsilon_n, \epsilon_t$ .

The extraction of the impact frequency  $\omega_c$  is straightforward both in the instantaneous impact and force method simulations (total number of impact detections/particle/time interval, divided by factor 2 to avoid counting twice the same impact), as long as the tendency for particle sticking is weak (weak to moderate self-gravity not leading to bound aggregates). In the calculation of impact related mean values, like the average of  $\epsilon_n$  in the case of velocity dependent elasticity, one can weight with  $v_n$  to exclude the contribution of possible sliding motion, if described by small, totally elastic rebounds in the instantaneous impact method.

The flow of momentum across the ring consists of a local contribution, related to the momentum carried with the particles during their random motions between successive impacts, and of a nonlocal contribution, arising due to momentum transferred via impacts or via gravitational forces, between particles at different radial distances (Wisdom and Tremaine, 1988). We denote the particle positions by  $\vec{r}$  and

<sup>2</sup> Observationally the importance comes from the close correspondence of  $\tau_D$  to the normal photometric optical depth  $\tau_\perp$ , which is the quantity inferred from occultation experiments: in the limit of homogeneous low filling factor systems  $\tau_D$  and  $\tau_\perp$  are identical. However, in a typical case of non-homogeneous and/or high filling factor rings they generally differ, see Ect. 1.8.2.1

their random velocities by  $\vec{c} = \dot{\vec{r}} - \vec{u}$ , with  $\vec{u}$  standing for the mean flow velocity at  $\vec{r}$ . For simplicity, we restrict our attention to the case of a linear shear profile  $\vec{u} = s x \hat{e}_y$ , where  $\hat{e}_y$  denotes the unit vector in tangential direction.

By definition, the components of the pressure tensor  $P_{\alpha\beta}$  give the amount of  $\beta$ -component of momentum transferred in  $\alpha$ -direction, per unit area and unit time. When evaluating the momentum flow in simulations, it is convenient to include all particles and impacts, regardless of their vertical coordinate. This corresponds to a vertical averaging

$$\overline{\hat{P}_{\alpha\beta}} = \int_{-\infty}^{\infty} \hat{P}_{\alpha\beta} dz \quad (1.77)$$

From hereon we denote  $\overline{\hat{P}_{\alpha\beta}}$  simply by  $\hat{P}_{\alpha\beta}$ , thus having the units of momentum/unit time/unit length.

The local contribution to the pressure tensor is obtained by adding the momenta  $p_\beta = mc_\beta$  of the  $N$  particles, moving with velocity  $c_\alpha$  with respect to the mean flow,

$$P_{\alpha\beta}^{local} = \frac{1}{A_o} \sum_i^N (c_\alpha)_i (mc_\beta)_i = n \overline{mc_\alpha c_\beta}, \quad (1.78)$$

where  $A_o$  is the area of the simulation region and  $n = N/A_o$  denotes the surface number density. The bar indicates average over particles. Once the steady-state has been achieved, one can improve the accuracy by averaging over arbitrarily long time intervals.

The standard formula for nonlocal momentum transfer is (Wisdom and Tremaine 1988)

$$P_{\alpha\beta}^{nl} = \frac{1}{A_o \Delta t} \sum_{impacts} \Delta r_\alpha m_{>\delta c_{\beta>}}, \quad (1.79)$$

where the summation is over all impacts occurring during the time interval  $\Delta t$ , and  $m_{>\delta c_{\beta>}}$  denotes the change of the momentum of the particle with the larger  $r_\alpha$  in each impact, and  $\Delta r_\alpha$  the absolute difference in the  $r_\alpha$ -coordinates of the impacting particles. However, application of this formula is problematic in the case of strong particle grouping, as it may be difficult to identify the separate impacts. For the case of force-method impact calculation, the collisional change of momentum is

$$m_{>\delta c_{\beta>}} = \int_{T_{dur}} F_{\beta>} dt, \quad (1.80)$$

where  $F_{\beta>}$  denotes the impact force felt by the particle with the larger  $r_\alpha$  coordinate, and  $T_{dur}$  is the duration of the impact. By defining

$$F_{\beta>} = \sum_i \sum_{j: (r_\alpha)_j > (r_\alpha)_i} \vec{F}_{\beta}^{ij}, \quad (1.81)$$

where  $\vec{F}^{ij}$  stands for the impact force exerted by particle  $i$  on the particle  $j$ , with  $\vec{F}^{ij} \neq 0$  for colliding, overlapping pairs, and zero otherwise, the integral (1.80) can be extended to the whole interval  $\Delta t$ , also covering the possibility of particles experiencing multiple simultaneous impacts, or even a permanent sticking of particles. Summing over all particles



then gives an equation corresponding to Eq. (1.79),

$$P_{\alpha\beta}^{nl} = \frac{1}{A_o} \left\langle \sum_i \sum_{\substack{j \\ (r_\alpha)_j > (r_\alpha)_i}} ((r_\alpha)_j - (r_\alpha)_i) F_{\beta}^{ij} \right\rangle, \quad (1.82)$$

where the average is taken over an arbitrary time interval. Furthermore, Eq. (1.82) can obviously be generalized to the momentum flow due to long-range forces, e.g in the case of self-gravity,

$$P_{\alpha\beta}^{grav} = \frac{1}{A_o} \left\langle \sum_i \sum_{\substack{j \\ (r_\alpha)_j > (r_\alpha)_i}} -Gm_i m_j \frac{((r_\alpha)_j - (r_\alpha)_i)((r_\beta)_j - (r_\beta)_i)}{|\vec{r}_j - \vec{r}_i|^3} \right\rangle. \quad (1.83)$$

Likewise,  $\vec{F}^{ij}$  can be identified with adhesive forces, Eq. (1.82) then giving their contribution to the nonlocal pressure. In the case of well defined separate impacts, Eqs. (1.79) and (1.82) give identical results for the nonlocal pressure tensor.

The corresponding contributions to the (vertically integrated) dynamic shear viscosity are readily evaluated from  $\eta = -\frac{1}{s} P_{12}$ . In the case of Keplerian shear,  $s = -\frac{3}{2}n$ , and we have

$$\eta_{local} = \frac{2}{3n} n \langle \overline{m c_x c_y} \rangle, \quad (1.84)$$

$$\eta_{nl} = \frac{2}{3n} \frac{1}{A_o \Delta t} \sum_{impacts} m_{>\Delta x} \langle \delta c_y \rangle, \quad (1.85)$$

$$= \frac{2}{3n} \frac{1}{A_o} \left\langle \sum_i \sum_{\substack{j \\ x_j > x_i}} \Delta x \langle F_y^{ij} \rangle \right\rangle, \quad (1.86)$$

$$\eta_{grav} = \frac{2}{3n} \frac{1}{A_o} \left\langle \sum_i \sum_{\substack{j \\ x_j > x_i}} -Gm_i m_j \frac{(x_j - x_i)(y_j - y_i)}{|\vec{r}_j - \vec{r}_i|^3} \right\rangle. \quad (1.87)$$

The kinematic shear viscosities are obtained from these, dividing by the surface mass density of the system  $\Sigma = n\bar{m}$ . In particular, in the case of identical particles (Wisdom and Tremaine, 1988)

$$\nu_{local} = \frac{2}{3n} \overline{c_x c_y}, \quad (1.88)$$

$$\nu_{nl} = \frac{2}{3n} \frac{1}{N \Delta t} \sum_{impacts} \Delta x \langle \delta c_y \rangle. \quad (1.89)$$

The above formula for gravitational viscosity is identical to that in Daisaka et al. (2001). Fig. 1.7 shows the contributions to the integrand of Eq. 1.87, arising from different relative locations  $\Delta x = x' - x$ ,  $\Delta y = y' - y$ . Largest gravitational torques are exerted by material within  $\sim 0.25\lambda_T$ , and almost all of  $\nu_{grav}$  is due to particles within one  $\lambda_T$ .

The velocity dispersion tensor is collected by sampling the random velocity components of each particle with short intervals and tabulating the averages values as a function of simulation time. In particular, in Sect. 1.6 we will use the time-averaged 1-d velocity dispersion  $c$  to characterize the

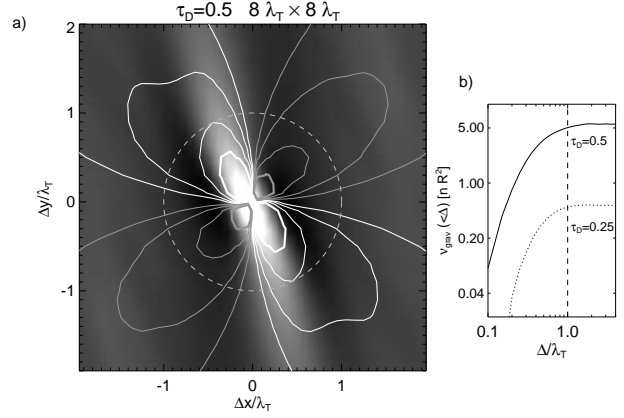


**Figure 1.7** a) The contributions to gravitational viscosity (Eq. 1.87). The contours indicate the mean torque density exerted from relative location  $(\Delta x, \Delta y)$ : positive (white contours) by the particles on the trailing quadrants and negative (gray contours) from the leading quadrants. The gray scale background image is the 2D auto-correlation function (Eq. 1.93) for the same simulation. Note the slightly larger positive net torques arising due to overdensities in the trailing quadrants. In b) the cumulative gravitational viscosity due to material within a cylindrical radius  $\Delta$  is shown as a function of  $\Delta/\lambda_T$ .

dynamical 'temperature' of the system

$$c^2 = \frac{1}{3} \langle \overline{c_1^2 + c_2^2 + c_3^2} \rangle = \frac{1}{3} \frac{tr \hat{P}^{local}}{\Sigma} \quad (1.90)$$

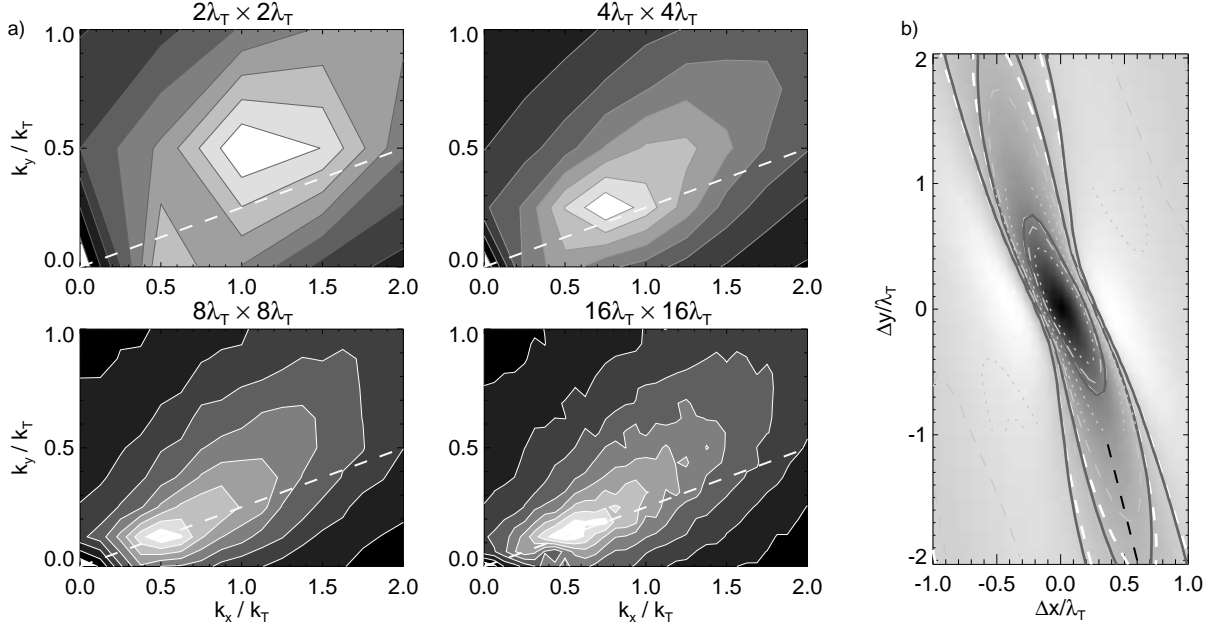
where  $c_1, c_2$ , and  $c_3$  are the principal axis components of the velocity dispersion tensor. At the low optical depth the largest principal axis points to the radial direction: at this limit  $c_2/c_1 = c_y/c_x = 0.5$  and  $c_3/c_1 = c_z/c_x \approx 0.65$ . The vertical thickness is defined as

$$H = \sqrt{12z^2}, \quad (1.91)$$

which corresponds to the full thickness of a uniform layer with the same vertical dispersion as the simulated particle field. At  $\tau_D \sim 0$ , we have  $H \approx 3c/n$ . The vertical distribution can be further characterized by tabulating the vertical density profile of the simulation particles. This can be based on the locations of particle centers (Wisdom and Tremaine, 1988), or by  $D_3(z)$  indicating the fraction of volume filled by particles as a function of  $z$  (Salo and Karjalainen, 2003). In particular, the filling factor at the equatorial plane  $D_3(z=0)$  (often denoted as  $FF(0)$ ) is useful in comparison to theoretical treatments of dense rings (Araki and Tremaine, 1986; Araki, 1991).

Other hydrodynamic quantities besides  $\nu$  can also be extracted from simulations, like the radial heat conductivity and bulk viscosity, and the temperature derivatives of pressure, shear viscosity and energy dissipation. Such tabulations were made in Salo et al. (2001) for non-gravitating simulations assuming three different values of  $n_z/n$ . However, compared to the shear viscosity that can be extracted at the steady-state, these other quantities require that the system is perturbed and the measurement is carried out while the system relaxes back toward the uniform steady-state. Besides the technical difficulties involved, the exact relation of





the derived quantities to their hydrodynamic interpretation is not clear. Mainly this is due to the non-isotropic velocity distribution (see Fig. 1.14e) following from particle's orbital motion around the planet. Such a distribution has more degrees of freedom than taken into account in hydrodynamical treatment. Nevertheless, such 'fitted' quantities applied to hydrodynamic stability analysis are quite successful in describing the viscous stability properties of larger-scale simulations (Schmidt et al., 2001; Schmidt and Salo, 2003).<sup>3</sup>

### 1.5.2 Characterization of self-gravity wakes

Examples of self-gravitating simulations were shown in Fig. 1.5 comparing snapshots from simulations with different sized calculation regions, while keeping other parameters the same. The snapshots indicated that the typical appearance of wake structure is evident even for calculation regions as small as  $2\lambda_T \times 2\lambda_T$ . However, comparison of gravitational viscosity (see Sect. 1.5) indicates that the strength of wakes is not fully developed unless a few times larger region, say  $8\lambda_T \times 8\lambda_T$  is simulated. Similarly, the spacing and pitch angle of wakes is affected by the periodic boundaries: this is illustrated in Fig. 1.8a in terms of 2D Fourier decomposition of surface density<sup>4</sup>

$$\Sigma(x, y) = \Sigma_0 \sum_{l, m} \tilde{\Sigma}_{l, m} \exp\left(i \frac{2\pi l}{L_x} x + i \frac{2\pi m}{L_y} y\right) \quad (1.92)$$

where  $|\tilde{\Sigma}_{l, m}|$  gives the normalized amplitude corresponding to the radial and tangential wavelengths  $\lambda_x = L_x/l$  and

<sup>3</sup> Isothermal hydrodynamical models which ignore bulk viscosity and temperature derivatives (Schmit and Tscharnuter, 1995) give qualitatively correct picture of viscous behavior but fail to predict quantitatively the correct regime of viscous overstability.

<sup>4</sup> A convenient way to calculate the amplitudes is to perform 2D FFT on the system whenever the image regions happen to be aligned along the x-axis, which takes place  $3\pi L_x/L_y$  times per orbit; at these instants FFT can be readily applied as  $\Sigma$  is periodic in both x and y.

**Figure 1.8** a) Fourier amplitudes  $|\tilde{\Sigma}_{l, m}|$  (see Eq. 1.92) in the simulations of Fig. 1.5, as a function of wavenumbers  $k_x = 2\pi/\lambda_x$  and  $k_y = 2\pi/\lambda_y$ , where  $\lambda_x$  and  $\lambda_y$  are the radial and tangential wavelengths. The contours indicate amplitude levels 0.1,...0.9 times the maximum amplitude. The dashed line indicates  $k_y = 0.25k_x$ , corresponding to a pitch angle  $\approx 14^\circ$ . In b) time averaged 2D auto-correlation functions of the same simulations (Eq. 1.93). Solid black and dashed white contours correspond to  $16\lambda_T \times 16\lambda_T$  and  $8\lambda_T \times 8\lambda_T$  simulations. Dashed black line indicates a  $14^\circ$  asymptotic pitch angle.

$\lambda_y = L_y/m$ . In the  $2\lambda_T \times 2\lambda_T$  simulation the peak amplitude occurs at  $(\lambda_x, \lambda_y) = (1, 2)\lambda_T$ , but when the region is increased,  $(\lambda_x, \lambda_y)$  approaches  $(2, 8)\lambda_T$ . This corresponds to a pitch angle  $\tan^{-1}(\lambda_x/\lambda_y) \approx 14^\circ$  between tangential direction and the the average direction of wakes.

The shape and orientation of the wakes is best illustrated in terms of 2D auto-correlation function of surface density,

$$\zeta_{2d}(\Delta x, \Delta y) = \frac{1}{\Sigma_0^2 A_0} \iint \Sigma(x + \Delta x, y + \Delta y) \Sigma(x, y) dx dy \quad (1.93)$$

Taking the time average of this describes the typical density structure the particle sees around its location. It can be calculated directly from stored particle snapshots (e.g. Salo 1995), or more conveniently (e.g. Toomre and Kalnajs 1991) with the FFT, by taking the inverse Fourier transform of the squared density amplitudes,  $\tilde{\zeta}_{2d} = |\tilde{\Sigma}_{l, m}|^2$ . Figure 1.8b displays the auto-correlation functions, together with a line corresponding to  $14^\circ$  pitch angle.

### 1.5.3 Energy budget in local simulations

In the steady-state, the energy dissipation rate is connected to momentum flow by

$$\dot{E}_{diss} - sP_{12} = 0 \quad (1.94)$$

where  $\dot{E}_{diss}$  is the energy loss in impacts, per unit time and unit area. Although this formula is valid for any shear flow, it is instructive to check how the formula actually arises in a local calculation region with periodic boundaries.

As mentioned in section 1.2, the quantity (Eq. 1.11)

$$E = E_{kin} + E_{pot} + E_{grav} \quad (1.95)$$

with

$$E_{kin} = \sum_i \frac{1}{2} m_i (\dot{x}_i^2 + \dot{y}_i^2 + \dot{z}_i^2) \quad (1.96)$$

$$E_{pot} = \sum_i m_i (ns x_i^2 + \frac{1}{2} n_z^2 z_i^2) \quad (1.97)$$

$$E_{grav} = -\frac{1}{2} G \sum_i \sum_{j \neq i} \frac{m_i m_j}{|\vec{r}_j - \vec{r}_i|} \quad (1.98)$$

is conserved along the orbital motion of particles. On the other hand,  $E$  changes both due crossing of radial boundaries and due impacts, via changes in  $E_{kin}$ , while both  $E_{pot}$  and  $E_{grav}$  remain unchanged<sup>5</sup>.

The above expression for  $E_{kin}$ , using the actual velocities of the simulation particles, includes both, the kinetic energy associated to their random motions,  $E_{rnd}$ , and the kinetic energy associated to the systematic shear flow  $E_{shear}$ ,

$$E_{kin} = E_{rnd} + E_{shear} \quad (1.99)$$

where

$$E_{rnd} = \frac{1}{2} \sum_i m_i \vec{c}_i^2 = \sum_i \frac{1}{2} m_i [\dot{x}_i^2 + (\dot{y}_i - s x_i)^2 + \dot{z}_i^2], \quad (1.100)$$

$$E_{shear} = \frac{1}{2} \sum_i m_i [2s x_i (c_y)_i + s^2 x_i^2] \quad (1.101)$$

Since  $E_{rnd}$ , rather than  $E_{kin}$  is of interest in many applications, we next look how it evolves in local simulations, subject to periodic boundaries, collisions, and gravitational forces.

In crossing of boundaries, the random velocity relative to mean flow is unaffected, so that  $\Delta E_{rnd}$  remains constant, the change of  $E_{kin}$  being associated solely with  $E_{shear}$ . In an impact of a particle pair

$$\begin{aligned} \frac{1}{2} \delta(m_1 \vec{v}_1^2 + m_2 \vec{v}_2^2) &= \frac{1}{2} \delta(m_1 \vec{c}_1^2 + m_2 \vec{c}_2^2) \\ &+ s [m_1 x_1 (\delta c_y)_1 + m_2 x_2 (\delta c_y)_2], \end{aligned} \quad (1.102)$$

where the last term can be combined to  $s m_2 (\delta c_y)_2 (x_2 - x_1)$ , using the conservation of momentum (the subscript 2 labels the particle with the larger radial coordinate). Summing over all impacts during the time interval  $\Delta t$  we have

$$(\Delta E_{rnd})^{coll} = \Delta E_{diss} - s \sum_{impacts} m_{>} (\delta c_y)_{>} \Delta x_{>}. \quad (1.103)$$

<sup>5</sup> Assuming that gravitational forces are constructed using the nearest image pairs, in which case the distances  $|\vec{r}_i - \vec{r}_j|$ 's are not affected.

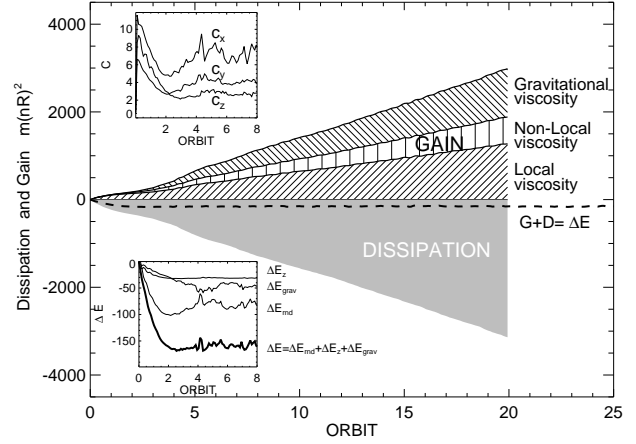


**Figure 1.9** Energy balance in the  $4\lambda_T \times 4\lambda_T$  simulation of Fig 1.5. Different contributions to viscous gain are shown separately: in the steady-state they balance the collisional dissipation. The small negative net value of the cumulative sum of gain and dissipation ( $G+D$ , dashed curve) equals the change in the total energy ( $\Delta E = \Delta E_{rnd} + \Delta E_{grav} + \Delta E_z$ ) when the system settled toward steady-state values from an initially 'hot' state: the upper insert shows the random velocity components, and the lower insert the various components of energy change. The energies are shown in units of  $m(nR)^2$ , where  $m$  is the total mass of simulation particles.

To obtain the change of  $E_{rnd}$  due to self-gravity and orbital motion, we use Eqs. (1.95) and (1.99) to write

$$\begin{aligned} E_{rnd} &= E - E_{grav} - E_{pot} - E_{shear} \\ &= E - E_{grav} - E_z \\ &- \sum_i m_i [(ns + \frac{1}{2} s^2) x_i^2 + s x_i (\dot{y}_i - s x_i)] \end{aligned} \quad (1.104)$$

where

$$E_z = \frac{1}{2} \sum_i m_i n_z^2 z_i^2 \quad (1.105)$$

denotes the potential energy associated with vertical motions. Since  $E$  is conserved during orbital motion, the change of  $E_{rnd}$  during time interval  $\Delta t$  equals

$$\begin{aligned} (\Delta E_{rnd})^{orb} &= -\Delta(E_{grav} + E_z) \\ &- \int_t^{t+\Delta t} \sum_i m_i \left[ (2ns + s^2) x_i \dot{x}_i \right. \\ &\left. + s \dot{x}_i (\dot{y}_i - s x_i) + s x_i (\ddot{y}_i - s \dot{x}_i) \right] dt. \end{aligned} \quad (1.106)$$

Substituting  $\ddot{y} = -2n\dot{x} + (F_y)_i/m_i$  from the equation of motion, where  $(F_y)_i/m_i$  is the y-component of the gravitational force felt by particle  $i$ , and taking into account that  $c_x = \dot{x}$ ,

$$\begin{aligned} (\Delta E_{rnd})^{orb} &= -\Delta(E_{grav} + E_z) \\ &- s \Delta t \left\langle \sum_i m_i (c_x)_i (c_y)_i + \sum_i x_i (F_y)_i \right\rangle \end{aligned} \quad (1.107)$$

Adding  $(\Delta E_{rnd})^{coll}$  and  $(\Delta E_{rnd})^{orb}$ ,

$$\Delta E_{rnd} = \Delta E_{diss} - \Delta(E_{grav} + E_z) - s \sum_{impacts} m_i (\delta c_y) \Delta x - s \Delta t \left\langle \sum_i m_i (c_x)_i (c_y)_i \right\rangle - s \Delta t \left\langle \sum_i x_i (F_y)_i \right\rangle \quad (1.108)$$

Clearly, the summation in the last term in the right-hand side can be arranged to a form involved in the formula for gravitational viscosity Eq. (1.87), while the two other sums correspond to non-local and local viscosities. Dividing by  $\Delta t$  and  $A_o$  thus gives

$$\dot{E}_{rnd} + \dot{E}_{grav} + \dot{E}_z = \dot{E}_{diss} - s P_{xy} = \dot{E}_{diss} + s^2 \eta \quad (1.109)$$

where the total viscous gain  $-s P_{xy}$  consists of local, nonlocal and gravitational viscosity contributions

$$P_{xy} = P_{xy}^{local} + P_{xy}^{nl} + P_{xy}^{grav} \quad (1.110)$$

In the steady-state the left hand side of Eq. (1.109) is zero, leading to the anticipated result in Eq. (1.94).

An example of energy balance in simulations is shown in Fig. 1.9 for a system that starts with a velocity dispersion exceeding the steady-state value. Initially both  $\dot{E}_{rnd}$  and  $\dot{E}_z$  are negative as the system cools and flattens down toward steady-state. Also the negative contribution of gravitational energy increases when the particles collect to dense wakes. In steady-state, the left-hand side of Eq. (1.109) vanishes and the rates of viscous gain and dissipation balance each other exactly.

## 1.6 Survey of simulation results

This Section collects simulation examples illustrating the intrinsic local dynamics of planetary ring systems. We start by discussing the simplest case of identical, non-selfgravitating particles, and demonstrate how the characteristics of the system's steady-state, e.g. the frequency of impacts and the velocity dispersion, depend on the coefficient of restitution and particle size. We show that the simulation results are consistent with heuristic hydrodynamical estimates. Particles' spin rotation, induced by surface friction and irregularities, is also briefly examined. We then proceed to systems with a distribution of particle sizes, and finally also include the particles' mutual self-gravity.

Our main goal is to understand how the dynamic viscosity varies with surface density, and how this relation depends on particles' physical properties. As mentioned above, this  $\eta(\Sigma)$  relation is crucial for the large-scale viscous stability properties of the particle ensemble. For non-gravitating systems the surface density is replaced with optical depth and dynamic viscosity then corresponds to  $\eta = \nu \tau_D$ . Two models (Fig. 1.10) for velocity-dependent coefficient of restitution are systematically compared, corresponding to laboratory measurements made by Bridges et al. (1984; 'frosty' ice) and Hatzes et al. (1988; 'smooth' ice). The former model, with a steeper drop of  $\epsilon_n$  with impact velocity leads to an energy balance where the velocity dispersion corresponds to ring

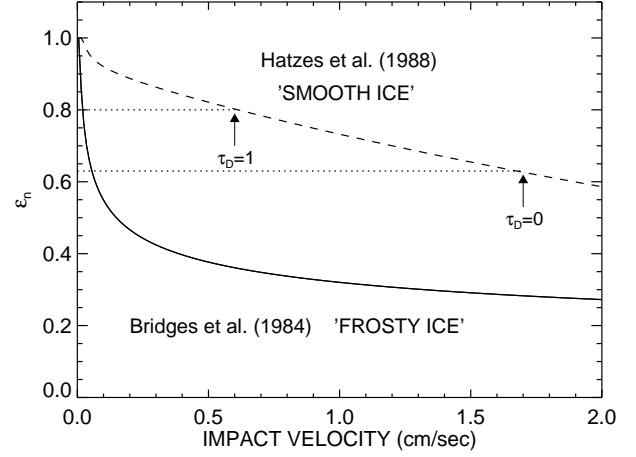


**Figure 1.10** Two velocity-dependent elasticity models describing laboratory measurements of icy particles. The curve labeled 'frosty' is for frost-covered ice (Bridges et al., 1984),  $\epsilon_n(v_n) = 0.32(v_n)^{-0.234} < 1$ , while the curve 'smooth' refers to particles with compacted-frost surfaces (Hatzes et al., 1988),  $\epsilon_n(v_n) = 0.90e^{-0.22v_n} + 0.01v_n^{-0.6}$ . The normal component of impact velocity  $v_n$  is expressed in cm/sec. The Bridges et al. (1984) model can also be written as  $\epsilon_n = (v_n/v_c)^{-0.234}$ , with  $v_c = v_B = 0.0077 \text{ cm/s}$ .

vertical thickness  $H \sim 10$  meters, (when assuming 1 meter ring particles), while the latter model implies a much hotter multilayer ring with  $H \sim 100$  meters: these two models serve to illustrate the uncertainty in ring particles' elastic properties. The viscosity versus density relation is constructed from small-scale simulations whose radial size is smaller than the shortest unstable wavelength so that no viscous perturbations can grow. It turns out that the two models predict drastically different viscous behavior: viscous instability in the case of thick rings and overstability in the case of flattened rings. Indeed, when the size of the simulation system is made sufficiently large both viscous instabilities and overstabilities can be directly verified in simulations (see Sect 1.7).

### 1.6.1 Simulations of non-selfgravitating systems

#### 1.6.1.1 Impact frequency

The ring system rapidly establishes an energy balance where the collisional dissipation is compensated by the viscous transfer of energy from the systematic orbital motion to random motions (Sect. 1.5.3). The time scale to reach this steady-state is determined by the frequency of particles' mutual impacts,  $\omega_c$ . As expected, the impact frequency increases proportional to optical depth  $\tau_D$ . An important peculiarity of planetary ring dynamics is that the steady-state  $\omega_c$  is practically independent from the velocity dispersion. This results from the partitioning of vertical and horizontal random motions via impacts. Thus for example an increase in velocity dispersion, which in itself would enhance  $\omega_c$ , is compensated by a corresponding vertical thickening and

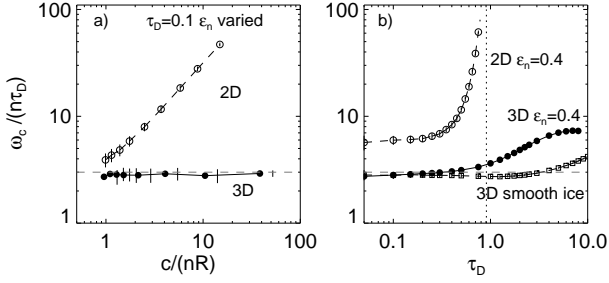


**Figure 1.11** Impact frequency  $\omega_c$  in 3D and 2D simulations, normalized to  $n\tau_D$ . In a) simulations with fixed  $\tau_D = 0.1$  are compared as a function of velocity dispersion  $c$ , normalized to  $nR$ ; the points correspond to steady-state values in simulations with different coefficient of restitution. In b)  $\omega_c$  as a function of optical depth for simulations with constant  $\epsilon_n = 0.4$  (circles) and using the Hatzes et al. (1988) velocity-dependent  $\epsilon_n$  (see Fig. 1.10). The vertical line indicates the  $\tau_{D\max}$  for 2D systems.

thereby reduced space density.<sup>6</sup> Analytic treatments taking into account the anisotropic distribution of impact directions and a Gaussian vertical profile (e.g Hämeen-Anttila, 1978), indicate

$$\omega_c \sim 3n\tau_D \sim 20\tau_D \text{ impacts/orbit}, \quad (1.111)$$

The independence of  $\omega_c$  on velocity dispersion is illustrated in Fig. 1.11a, together with the approximation of Eq. 1.111 (dashed line). For comparison, the figure also shows  $\omega_c$  in a 2D simulation where the motion of particles is limited to the central plane. In this case no adjustment between velocity dispersion and space density is possible and the explicit velocity dispersion dependence in  $\omega_c$  is retained. As discussed in Salo and Schmidt (2010) this leads to fundamental differences in the viscosity versus density relations and thus the stability properties of 2D and 3D simulation systems.

The linear dependence of  $\omega_c$  on  $\tau_D$  breaks down for flattened systems ( $\epsilon_n = 0.4$ , yielding  $H/R \sim 1$ ) when  $\tau_D \gtrsim 1$ , in which case the particles' own volume limits the free space available for motion (Hämeen-Anttila 1978). Similarly in a 2D system the impact frequency increases dramatically when the maximum 2D packing limit (maximum  $\tau_D = \pi/\sqrt{12} \approx 0.907$  for identical particles) is approached. On the other hand, for a hot 3D multilayer ring ('smooth' ice,  $H/R \gg 1$ ) the simple approximation holds quite well even for  $\tau_D > 1$ .

### 1.6.1.2 Establishment of Local Energy balance

Figure 1.12 displays the time evolution of the velocity dispersion  $c$  in simulations with different elasticity models. For

<sup>6</sup> The basic formula is  $\omega_c \propto N_3 c_1 \sigma_c$ , where  $N_3$  is the volume number density,  $c_1$  is the 1-dimensional velocity dispersion and  $\sigma_c$  the collisional cross-section:  $\sigma_c = 4\pi R^2$  assuming identical particles with radius  $R$ . The volume number density  $N_3 \approx N_2/H$ , where  $N_2 = \tau_D/(\pi R^2)$  is the surface number density and  $H$  the vertical thickness. Due to collisional coupling of horizontal and vertical motions,  $c_z \sim c_1$ , while due to orbital motion  $H \propto c_z/n$ . The explicit  $N_3$  and  $c_1$  dependencies thus cancel out, leading to the formula 1.111,

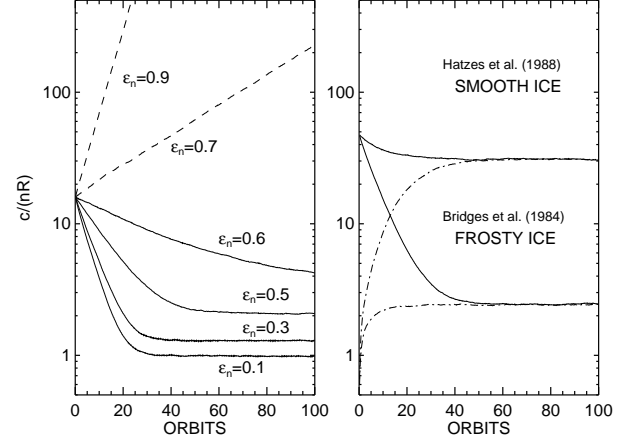


**Figure 1.12** a) Evolution of velocity dispersion in simulations with different value of constant coefficient of restitution  $\epsilon_n$ , for optical depth  $\tau_D = 0.1$ . The critical value  $\epsilon_n \approx 0.65$  separates the thermally stable (solid) and unstable (dashed) systems. (b) Simulations with two velocity dependent elasticity models of Fig. 1.10, starting from different initial states. Now the system attains a steady-state with the final velocity dispersion depending on the  $\epsilon_n(v_n)$  relation: the 'smooth' ice model with a shallower drop of elasticity with  $v_n$  leads to a much hotter steady-state than the 'frosty' ice model where  $\epsilon_n$  drops very fast with  $v_n$ .

a constant  $\epsilon_n$  sufficiently close to unity  $c$  increases exponentially with time, and clearly no steady-state is achieved<sup>7</sup>. A constant  $\epsilon_n$  closer to zero leads to an exponential drop until  $c$  levels at a few times  $nR$ , corresponding to a few particle diameter thick ring. On the other hand, in the case of  $\epsilon_n(v_n)$  the steady-state depends on the functional form of the relation. The Bridges et al. (1984) model ('frosty' ice) leads to a flattened system very similar to  $\epsilon_n \approx 0.5$ , whereas the Hatzes et al. (1988) model ('smooth' ice) leads to a multilayer ring. Fig. 1.12b also illustrates the rapid time scale of evolution: here the system forgets the initial conditions in roughly 50 orbital periods, which for the used  $\tau_D = 0.1$  corresponds to about 100 impacts/particle.

The above velocity evolution can be qualitatively explained with a simple heuristic description of the energy balance between dissipation and viscous gain (see Stewart et al (1984), Schmidt et al. (2009)). According to Eq. (1.109), the rate of kinetic energy change/unit mass is

$$\dot{E}_{rnd}/\Sigma + \dot{E}_z/\Sigma = \dot{E}_{diss}/\Sigma + s^2\nu \quad (1.112)$$

Inserting the Keplerian shear rate  $s = -\frac{3}{2}n$  and averaging the energy dissipation in individual impacts (Eq. 1.43; keeping just the  $\epsilon_n$  contribution, and absorbing the term  $\dot{E}_z$

<sup>7</sup> These simulations were carried out with the instantaneous impact method, since the force method would in any case require very small  $T_{dur}$  for such dynamically very hot simulations, in order to keep  $\xi_{max} \ll R$ .



which relates to vertical flattening into  $\dot{E}_{rnd}$ ), we can write

$$\begin{aligned} \frac{1}{2} \frac{dc^2}{dt} &= -k_1 \omega_c c^2 (1 - \epsilon_n^2) \\ &+ \frac{9}{4} n^2 \left[ \underbrace{k_2 c^2 \frac{\omega_c}{\omega_c^2 + n^2}}_{\nu_{local}} + \underbrace{k_3 \omega_c R^2}_{\nu_{nl}} \right], \end{aligned} \quad (1.113)$$

where the viscosity has been written as a sum of local and nonlocal contributions, and  $k_1, k_2, k_3$  are all constants of the order of unity. The basic expression for local viscosity is  $\nu_{local} = \omega_c \lambda^2$ , where  $\lambda$  is the radial mean free path between impacts. In the high impact frequency regime the impacts limit the mean free path to  $\lambda \sim c/\omega_c$  while for low  $\omega_c$  an upper bound is set by the amplitude of epicyclic excursions,  $\lambda \sim c/n$ . Combining these estimates (Goldreich and Tremaine, 1978b) leads to the form in Eq. (1.113). For the non-local term the  $\lambda$  is set equal to the particle radius  $R$ .

The Eq. (1.113) describes qualitatively quite well the simulated behavior for a given elasticity of particles. In particular, if the system is very hot,  $c/(nR) \gg 1$ , the nonlocal gain term can be ignored. In this case both the gain and dissipation terms in the right hand side are proportional to  $c^2$ . Thus, no balance is possible unless  $\epsilon_n$  equals a critical value  $\epsilon_{cr}$ , which (approximating  $\omega_c \sim n\tau_D$ ) depends on the optical depth via the well-known Goldreich-Tremaine formula

$$(1 - \epsilon_{cr}^2)(1 + \tau_D^2) = \frac{9k_2}{4k_1} \approx 0.61. \quad (1.114)$$

If the constant  $\epsilon_n > \epsilon_{cr}$ , velocity dispersion increases continuously, as the dissipation is too weak to balance the local viscous gain. Similarly, if the constant  $\epsilon_n < \epsilon_{cr}$ , then dissipation exceeds the local viscous gain, leading to reduced  $c$ . The eventual steady-state is determined by the nonlocal gain implying a final  $c \propto nR$ . According to Eq. (1.114),  $\epsilon_{cr} \approx 0.65$  for  $\tau_D \rightarrow 0$ , in good agreement with the low  $\tau_D$  simulations of Fig. 1.12. In the case of velocity dependent  $\epsilon_n$ , the behavior is different, since the effective value of  $\epsilon_n$  depends on the average impact velocity  $\sim c$ . In the limit  $\nu_{local} \gg \nu_{nl}$  (equivalent to  $c \gg nR$ ), the steady state  $c$  would be adjusted to a value that yields  $\epsilon_{eff} = \epsilon_{cr}$ , where  $\epsilon_{eff}$  is the weighted mean of  $\epsilon_n(v_n)$  in impacts.

Figure 1.13 shows the Goldreich-Tremaine  $\epsilon_{cr}$  as a function of  $\tau_D$ , delineating the thermally stable ( $\epsilon_n < \epsilon_{cr}$ ) and unstable ( $\epsilon_n > \epsilon_{cr}$ ) regimes. When  $\tau_D$  is increased, less and less dissipation is allowed for a thermally stable state to exist, so that  $\epsilon_{cr}$  approaches unity. This follows from the weakening of the local contribution to viscous gain, due to reduced mean free path  $\lambda$  as  $\tau_D$  increases. Similarly, in the case of a reduced central shear rate, the  $\epsilon_{cr}$  would rise toward unity in order to compensate for the less effective viscous gain (for example  $\epsilon_{cr} \approx 0.85$  at  $\tau_D \rightarrow 0$  for a flat rotation curve with  $s = -n$ ).

Also shown in the Fig. 1.13 are mean values of  $\epsilon_n$  measured from simulations. Open symbols show simulations which lead to a dynamically hot steady-state with  $c \gg nR$ , thus mimicking the conditions leading to Eq. (1.114). In this case the agreement with theoretical approximation is quite obvious. For comparison, filled circles show mean  $\epsilon_n$  in simulations which lead to a steady-state with  $c/(nR)$  not far from

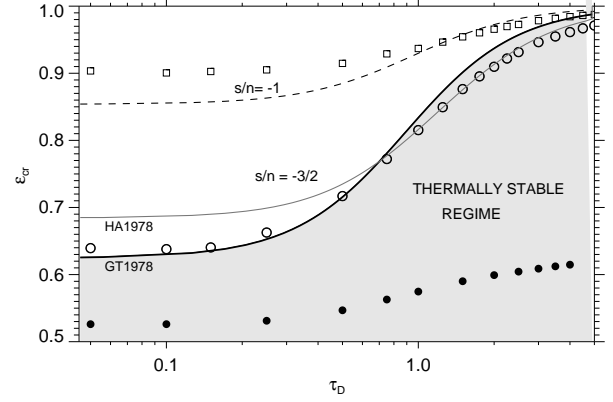


**Figure 1.13** Thick solid line is the Goldreich-Tremaine  $\epsilon_{cr}(\tau_D)$  relation; thin solid line is the  $\epsilon_{cr}$  from (Hämeen-Anttila, 1978). Systems with constant  $\epsilon_n < \epsilon_{cr}(\tau_D)$  (shaded region) flatten toward a stable near-monolayer state, while those with  $\epsilon_n > \epsilon_{cr}(\tau_D)$  disperse via growing random velocities. Dashed line shows an approximate critical curve for a flat velocity field with  $s/n = -1$  (obtained by replacing  $9/4$  with  $1$  in 1.114). Open symbols indicate effective mean values of  $\epsilon_n$  in dynamically hot simulations with  $c/(nR) \gg 1$  (Bridges-type elasticity formula with  $vc = 100v_B = 0.77$  cm/sec). For comparison, solid symbols indicate effective  $\epsilon_n$  in simulations with the original Bridges elasticity law. Note that the effective mean of  $\epsilon_n$  depends on how impacts are weighted (Salo, 1987b); here we use  $\epsilon_{eff} = \langle \epsilon_n(v_n) v_n^2 \rangle / \langle v_n^2 \rangle$ .

unity: in this case both local and nonlocal viscous gains are important, and the steady-state dissipation rate is larger (mean  $\epsilon_n$  closer to zero) than implied by the Goldreich-Tremaine formula which takes into account only the local viscous gain.

### 1.6.1.3 Steady-state as a function of optical depth

Figure 1.14 collects the various steady state properties as a function  $\tau_D$ , for the above two  $\epsilon_n(v_n)$  models. As mentioned earlier, the main difference between the models is the about 10-fold larger velocity dispersion for the smooth ice model at the low  $\tau_D$  regime. This follows from the shallower slope in the  $\epsilon_n(v_n)$  relation, indicating that on the average must faster impacts are needed to yield the required dissipation rate. When optical depth increases, there is a strong drop in the  $c$ : this results from the above mentioned reduced local viscous gain: energy dissipation rate adjust by reducing the average impact velocities. This was illustrated in Fig. 1.10 by indicating the effective  $\epsilon_n$  values a hot system adjusts to when  $\tau_D = 0$  and  $\tau_D = 1$ , implying a factor  $\sim 3$  difference in average impacts velocities - this corresponds to the drop of  $c$  in Fig. 1.14. For the 'frosty ice' model there is hardly any change of  $c$  with  $\tau_D$ : this is because the local gain term dominates for all  $\tau_D$ 's. For the 'smooth ice' model the large drop in  $c$  reflects also in the strong flattening of the system and the drop of local kinematic viscosity.

The resulting viscosity versus density relations is quantified in Fig. 1.14d where the slope  $\beta = d \log \nu / d \log \tau_D$  is displayed. Values of  $\beta < -1$  correspond to negative  $d\eta/d\tau_D$ ,



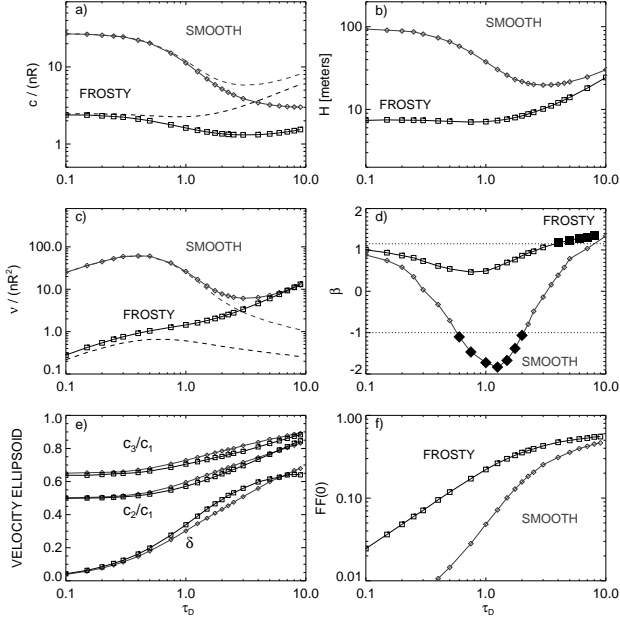


**Figure 1.14** Steady-state quantities as a function of  $\tau_D$  in simulations with velocity-dependent coefficient of restitution: a) the velocity dispersion  $c$  (dashed lines include also the contribution from nonlocal pressure, obtained by using  $\hat{P}^{nl}$  in Eq. (1.90)), b) the vertical thickness  $H$ , c) the kinematic viscosity (dashed lines indicate the local contribution), and d) the slope of  $\nu \propto \tau_D^\beta$  relation; the values of  $\beta < -1$  predict viscous instability and  $\beta \gtrsim 1$  viscous overstability (large filled symbols), e) shows the axial ratios of the velocity ellipsoid  $c_2/c_1$  and  $c_3/c_1$ , and the angle  $\delta$  between the radial direction and the largest principal axis component, and f) the central plane volume filling factor  $FF(0)$ .

the condition for *viscous instability* (collision-induced momentum flux tends to enhance density fluctuations; see Fig. 1.25 for a schematic illustration). In principle  $\beta > -1$  indicates viscous stability (collisions smooth density fluctuations). However, particle simulations (Salo et al. 2001) and hydrodynamical models (Schmidt et al 2001) indicate that for  $\beta > 1$  the system may be prone to *viscous overstability*. The 'smooth ice' elasticity model implies instability for  $0.7 \lesssim \tau_D \lesssim 2$ , while the 'frosty ice' fulfills condition for overstability if  $\tau_D \gtrsim 4$ . We check these predictions in Section 1.7 with radially more extended simulations.

The lowermost row in Fig. 1.14 shows the shape and orientation of the velocity ellipsoid. Regardless of the large difference in the steady-state velocity dispersion, the principal axial ratios are not very different for the two models. At the limit  $\tau_D \rightarrow 0$  the ratio  $c_2/c_1 \rightarrow 0.5$  for both models, being determined solely by the systematic gradient in the Keplerian velocity field. On the other hand, the ratio  $c_3/c_1$  depends somewhat on the effectivity of collisions in transferring energy from horizontal to vertical motions: this ratio is smaller in the case of more inelastic models yielding flatter systems. With increased  $\tau_D$ , both  $c_2/c_1$  and  $c_3/c_1$  increase toward unity, though even at the largest stud-

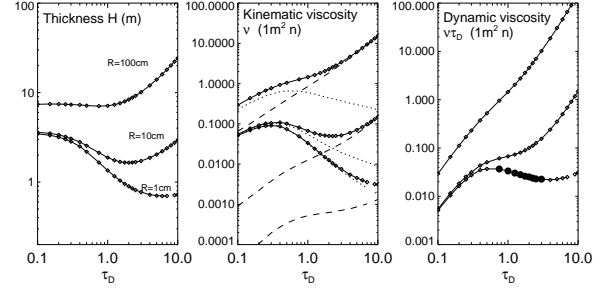


**Figure 1.15** Dependence of a) geometric thickness  $H$ , b) kinematic viscosity  $\nu$ , and c) dynamic viscosity  $\eta = \nu \tau_D$  on optical depth  $\tau_D$ , for the 'frosty' ice model of the previous figure, but with different sized simulation particles. Large solid circles in c) indicate viscously unstable regime. In b) dotted and dashed lines indicate separately the local and nonlocal contributions.

ied value,  $\tau_D = 10$ , the velocity ellipsoid is still far from isotropic, even if the impact frequency already corresponds to over 100 impacts/orbital period. Likewise, the deviation  $\delta$  of the longest principal axis from the radial direction, increases with  $\tau_D$ , but is still below the hydrodynamical limit  $\pi/4$  even at  $\tau_D = 10$ . Also shown is the central plane volume filling factor of the two models: for the 'frosty' ice model,  $FF(0)$  exceeds 0.2 for  $\tau_D > 1$ , while for the 'smooth ice' model the same requires  $\tau_D > 3$ . Comparison to Fig. 1.11 indicates that this is roughly the regime where the nonlinearity of  $\omega_c$  versus  $\tau_D$  becomes apparent.

The above simulation survey for 'frosty' and 'smooth' elasticity models was done using 1 meter particles at the distance of 100 000 km. In this case the 'smooth ice' model was dominated by local viscosity at low  $\tau_D$ , while with the 'frosty' ice model nonlocal viscosity dominated at all  $\tau_D$ 's. Consequently, the former model is susceptible for viscous instability while the latter model is not. To remind that this behavior depends on the assumed particle size/elasticity model combination, Fig 1.15 compares the expected behavior of the 'frosty ice' model when using particles sizes of 0.01, 0.10 and 1 meters. For a rough estimate of the relative importance of local and nonlocal contributions, note that at  $\tau_D \rightarrow 0$  the local contribution tries to establish a state with a mean  $\epsilon_n \approx 0.65$ . For the Bridges et al. (1984) frosty ice model this corresponds to  $c_{\text{local}} \approx 0.05$  cm/s. On the other hand, the nonlocal contribution maintains a minimum  $c_{\text{nonlocal}} \approx nR = 0.2$  cm/sec with the nominal values of the previous figures. Thus with 1 meter particles  $c_{\text{nonlocal}}$  exceeds  $c_{\text{local}}$  by a factor of 4. However, with 1 cm simulation particles,  $c_{\text{nonlocal}} \ll c_{\text{local}}$ , and a strong drop in the steady-state  $c$  around  $\tau_D \sim 1$  is again present. This would again lead to viscously unstable behavior for intermediate  $\tau_D$ 's.

#### 1.6.1.4 Surface friction and Particle spins

In contrast to the normal coefficient of restitution, relatively few measurements exist for the friction of icy particles. Ac-

cording to Supulver et al. (1995) experiments, friction is weak, corresponding to tangential coefficient of restitution  $\epsilon_t \sim 0.9$  in the case of relatively smooth ice surfaces at temperatures near 100 K. Nevertheless, to illustrate the possible effects of tangential friction we will briefly examine the whole allowable range of  $1 \geq \epsilon_t \geq -1$ , the latter extreme corresponding to the case where friction is able to reverse the tangential relative velocity in impact. Also, as discussed in Section 1.3, a consistent treatment of tangential friction between freely moving particles requires the inclusion of particle spins, which allows for energy transfer between random and rotational motions.

With the addition of frictional dissipation the steady-state velocity dispersion is reduced, the importance of this reduction depending on both the value of  $\epsilon_t$  and the model for  $\epsilon_n$ . This is illustrated in Fig. 1.16, comparing different  $\epsilon_t$  values for 'frosty' and 'smooth' ice elasticity models. A fixed  $\tau_D = 0.5$  is studied, but the relative effects is only weakly dependent on  $\tau_D$ . The influence of  $\epsilon_t$  is much more pronounced for the dynamically hot 'smooth' ice model. This follows since the energy gain is then determined by the local viscosity. Inclusion of friction adds a dissipation term proportional to  $\omega_c c^2(1 - \epsilon_t^2)$  to Eq. (1.113), which means that the effective  $\epsilon_n$  required for thermal balance can be closer to unity (Salo, 1987a,b; Araki, 1988, 1991; Ohtsuki, 2006), thus indicating smaller  $c$ . The extra dissipation is most pronounced when  $\epsilon_t$  is close to zero, leading to minimum of  $c$  near this value. On the other hand, a much smaller adjustment in  $c$  is possible when the balance is dominated by nonlocal viscosity ('frosty' ice model in the figure).

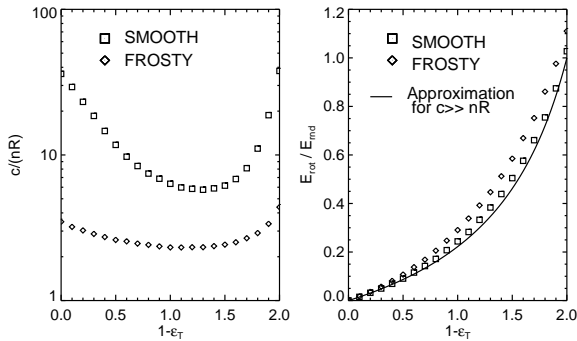


**Figure 1.16** Effect of tangential coefficient of restitution  $\epsilon_t$  on a) the steady-state velocity dispersion, and b) the energy ratio between the rotation and random velocities. The 'frosty' and 'smooth' ice elasticity models are compared for  $\tau_D = 0.5$ . The solid line is the theoretical approximation (Eq. 1.117) for the energy ratio in the limit  $c \gg nR$ .

Friction also induces spin motion of particles, which provides a feedback of energy from rotation to random motions (explains why the minimum of  $c$  is not exactly at  $\epsilon_t = 0$ ). An equilibrium ratio between random and rotational energies is established when the net transfer equals zero. In practice the

equilibrium implies that the dispersion of the surface velocities due to spins follows the dispersion of random velocities

$$\overline{(R\omega)^2} = k \overline{c^2}, \quad (1.115)$$

the proportionality factor  $k$  depending mainly on  $\epsilon_t$ , and to lesser degree on  $\epsilon_n$  and  $\tau_D$ . For a thick multilayer system the resulting equilibrium ratio of spin and random energies can be estimated by averaging the formula for the change of spin energy in individual impacts (Eq. 1.43), and by assuming an isotropic distribution of impact directions (should be valid in the case  $c \gg nR$ ). For homogeneous spheres with

$$E_{rot} = \frac{1}{5}m(q_1^2 + q_2^2 + q_3^2), \quad (1.116)$$

$$E_{rnd} = \frac{1}{2}m(c_1^2 + c_2^2 + c_3^2),$$

this yields (Salo 1987a,b, Morishima and Salo (2006))

$$\frac{E_{rot}}{E_{rnd}} \approx \frac{2(1 - \epsilon_t)}{14 - 5(1 - \epsilon_t)}, \quad (1.117)$$

indicating that the energy ratio grows roughly proportional to  $1 - \epsilon_t$  for  $\epsilon_t$  close to unity. At the limit  $\epsilon_t \rightarrow -1$  a total equipartition between rotation and random energies is predicted, in agreement with Shu and Stewart (1985). Based on Fig. 1.16, the Eq. (1.117) holds quite well for the 'smooth' ice model, especially in the limit  $|\epsilon_t| \rightarrow 1$  where the system has the largest velocity dispersion. For a more flattened system ('frosty') the simulated  $E_{rot}/E_{rnd}$  ratio is somewhat larger, reflecting the non-isotropic orientations of impact directions.

In addition to dispersion of spins, the particles also acquire a small residual mean vertical spin

$$\overline{\omega_z} \sim (0.2 - 0.3)n \quad (1.118)$$

(Salo, 1987a,b; Richardson, 1994; Ohtsuki and Toyama, 2005; Morishima and Salo, 2006). This mean value is only weakly dependent on  $\epsilon_t$ ,  $\epsilon_n$  or  $\tau_D$ . Since  $\sqrt{\omega_z^2}$  is proportional to  $c/R$  while  $\overline{\omega_z}$  is independent of  $c$ , the ratio  $\overline{\omega_z}/\sqrt{\omega_z^2}$  can be significantly non-zero only for very flattened systems with small  $c/(nR)$ .

#### 1.6.1.5 Surface irregularity/deviations from spherical shape

Almost all planetary ring simulations have assumed spherical particles. Mainly this is due to the technical simplifications it affords for detection and modeling of impacts. Also, the need for more complicated models is not obvious, since in many respects the effect of small deviations from spherical shape can be expected to average out, or to be accommodated by the uncertainties in the other model parameters like the elasticity of particles. However, irregular shape may have a significant contribution to particle spins, even if the tangential friction is small.

The effect of slightly non-spherical shape in promoting spin dispersion is illustrated in Figure 1.17, in terms of the energy ratio between rotation and random motions. The simulations use the irregularity model of Salo (1987a,b), where the normal vector of the local tangent plane of impact ( $\vec{k}^*$ ) deviates slightly from the direction vector joining the

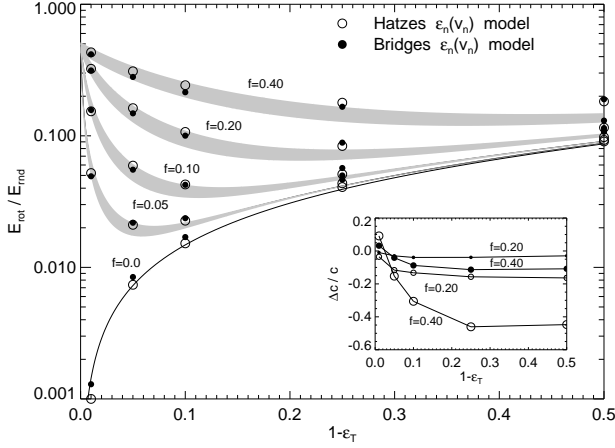


**Figure 1.17** The effect of small irregularities/deviation from spherical shape on the energy ratio between rotation and random motions. Simulations with different  $f$  (the maximum local tilt of the impact plane, see the text) are compared as a function of  $\epsilon_t$  for two  $\epsilon_n(v_n)$  models. The optical depth  $\tau_D = 0.5$ . The theoretical energy ratio for mass point systems, Eq (1.119) applies to a constant  $\epsilon_n$ : the gray filled areas correspond to this approximation with  $\epsilon_n = 0.5 - 0.8$ . The insert shows the relative change in velocity dispersion  $c$  compared to the case  $f = 0$ . Two values of  $f$  are compared (larger symbols  $f = 0.4$ , smaller symbols  $f = 0.2$ ).

particle centers ( $\vec{k}$ ). In the figure the tilts  $\gamma_a$  and  $\gamma_b$  in Eq. (1.44) are assumed to get independent random values uniformly from the interval  $[-f, f]$ : the maximum studied value  $f = 0.4$  corresponds to rms tilt angle  $\sim 10^\circ$ . Such a model is very efficient in inducing spin rotation even if the particles are almost frictionless: for example  $\epsilon_t = 0.99$ ,  $f = 0.05$  (corresponds to  $\sim 1^\circ$  rms tilt) gives about the same amount of spin rotation than  $\epsilon_t = 0.5$  for spherical particles with  $f = 0$ . Curiously enough, the energy ratio at the limit  $\epsilon_t \rightarrow 1$  is independent of  $f$ . The figure also shows an estimate of the equilibrium energy ratio (again setting the net transfer to zero; Salo 1987a), which is in good agreement with the simulation results,

$$\frac{E_{rot}}{E_{rnd}} = \frac{2}{7} \frac{\frac{2}{3}f^2(\epsilon_t + \epsilon_n)(1 + \epsilon_n) + \frac{1}{2}(1 - \epsilon_t)^2}{(1 - \epsilon_t) + \frac{2}{3}f^2(\epsilon_t + \epsilon_n) - \frac{5}{14}(1 - \epsilon_t)^2}. \quad (1.119)$$

The theoretical estimate is for a constant  $\epsilon_n$ , but the dependence on  $\epsilon_n$  is weak (see Fig. 1.17) This agrees with the fact that the simulated  $E_{rot}/E_{rnd}$  are very similar for both studied  $\epsilon_n(v_n)$  models. At the limit  $\epsilon_t = 1$  this approximation predicts  $E_{rot}/E_{rnd} = \frac{2}{7}(1 + \epsilon_n) \sim 0.5$ .

Irregularity also affects the equilibrium velocity dispersion, the effect depending on  $\epsilon_t$  and  $\epsilon_n$  (see the insert in Fig. 1.17). In the case of a hot system ('smooth' ice  $\epsilon_n(v_n)$  model), the reduction in  $c$  for  $f = 0.4$  is close to 50% for  $\epsilon_t < 0.8$ . However, for  $\epsilon_t$  very close to unity, irregularity may also slightly increase  $c$  due to feedback of energy from rotation (Salo 1987b). For a cool system ('frosty' ice  $\epsilon_n(v_n)$  model) the effect of irregularity, like that of friction, is much smaller.

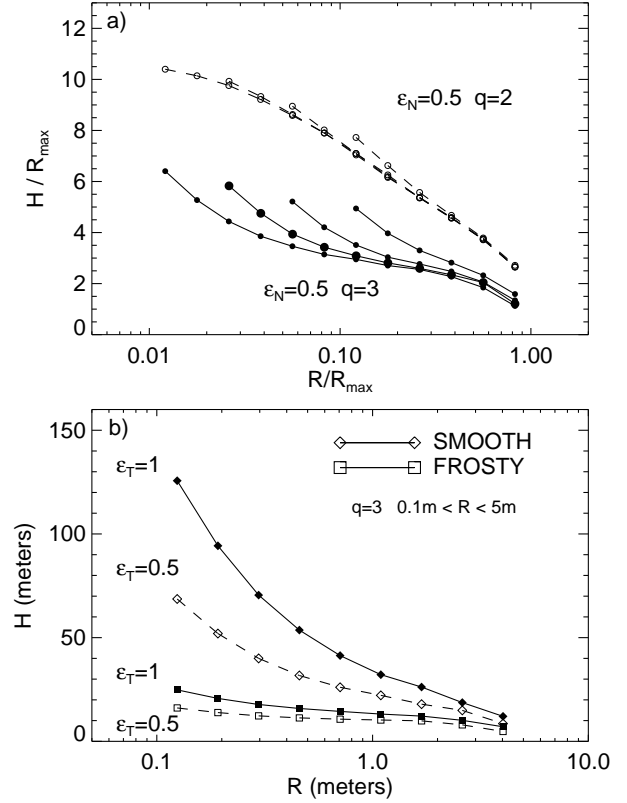


**Figure 1.18** In a) the geometric thickness as a function of particle size in simulations with a power law size distribution,  $dN/dr \propto r^{-q}$ , for  $R_{min} < R < R_{max}$ . Different widths of the distribution,  $W = R_{max}/R_{min}$ , in the range  $W = 4.64 - 100$  are compared, both for  $q = 2$  and  $q = 3$ . In each case  $\tau_D = 1.0$  and a constant  $\epsilon_n = 0.5$  is used. In b) two different  $\epsilon_n(v_n)$  models are compared for the same size distribution. Dashed lines show the effect of friction with  $\epsilon_t = 0.5$ .

#### 1.6.1.6 Size distribution

So far all our simulation examples have assumed identical particles. In the more realistic case of size distribution, the energy balance is modified by the energy transfer in impacts (and via gravitational encounters) from larger to smaller particles (see Stewart et al. (1984), Hämeen-Anttila (1984)). However, in contrast to gas dynamical systems this tendency toward energy equipartitioning is opposed by the inelasticity of impacts: simulations indicate that near equipartition is possible only for particle mass ratios below about 10 (Ohtsuki 1991, Salo 1992a). In practice the ratio between velocity dispersion of smallest and largest is less than about five, the maximum ratio depending on the functional form of the size distribution and the elasticity model.

Figure 1.18a shows how the vertical thickness  $H$  of different sized particles depends on the width  $W = R_{max}/R_{min}$  and index  $q$  of the power-law size distribution with  $dN/dR \propto R^{-q}$ . A constant  $\epsilon_n = 0.5$  is used, in which case all simulation quantities scale with the assumed maximum particle size. Therefore, quantities normalized to  $R_{max}$  are shown. For  $q = 3$  the maximum ratio in the vertical thickness of the

bin of smallest and largest particles ( $H_{\text{small}}/H_{\text{large}}$ ) depends only weakly on  $W$ , while for  $q = 2$  it slightly increases with  $W$ . For  $q = 2$  most of the mass is on the largest particles: consequently the influence of small particles on the largest particles is small and  $H_{\text{large}}$  is independent of  $W$ . For  $q = 3$  each logarithmic size increment corresponds to same fraction of total mass, and increasing the width  $W$  pushes  $H_{\text{large}}$  down. The lower panel of Fig. 1.18 compares the two different  $\epsilon_n(v_n)$  models for  $q = 3, W = 50, R_{\text{max}} = 5\text{m}$ , emphasizing how the difference between small and large particles becomes stronger for hot systems. In terms of steady-state velocity dispersion, the  $c_{\text{small}}/c_{\text{large}} \approx H_{\text{small}}/H_{\text{large}} \approx 10$  for the 'smooth' model, and about 3 for the 'frosty' ice. For comparison, for a constant  $\epsilon_n \rightarrow 0$ , the  $c_{\text{small}}/c_{\text{large}} \approx 1.5$ . All simulations of Fig. 1.18 have  $\tau_D = 1.0$ , but the results are only weakly dependent on  $\tau_D$  (Salo 1992a).

The effect of friction on  $c$  is roughly the same on all particle size bins (dashed lines in Fig. 1.18b). Also the equilibrium dispersion of surface spin velocities,  $(R\omega)^2$  scales with  $c^2$  of the size bin. The relatively weak dependence of  $c$  on  $R$  thus indicates that the spin dispersion  $\sqrt{\omega^2}$  is roughly inversely proportional to the particle radius. Therefore, small particles spin much faster than the large ones. On the other hand, the residual mean spin is always a fraction of  $n$  independent of particle size. Therefore, while the mean spin of the largest particles can be significant compared to its dispersion, the spin axis of the smallest ones are always practically randomly distributed. For an illustration of progradely rotating large particles embedded in a population of randomly oriented small particles, see Salo(1987b).

### 1.6.2 Self-Gravitating simulations

At low optical depth the main effect of self-gravity is through 2-body scattering in close binary encounters. Although they correspond to completely elastic impacts in the sense that the kinetic energy of the encountering pair is conserved, the deflection of the orbits during encounter leads to energy transfer from systematic to random motions. This extra heating increases  $c$  until it becomes roughly comparable to the 2-body escape velocity of the particles (Safranov, 1969; Hämeen-Anttila, 1978; Cuzzi et al., 1979). For larger surface densities, the collective effects become increasingly important. For example, in Saturn's dense B the vertical self-gravity may exceed the vertical component of the central force by a large factor (Wisdom and Tremaine, 1988). Nevertheless, then also the planar components of gravity need to be taken into account, leading to a strongly non-uniform density distribution.

#### 1.6.2.1 Formation of self-gravity wakes

Figure 1.19 compares different ways to approximate ring self-gravity: using in b) the factor  $n_z/n > 1$  to mimic the increased vertical field and in d) the self-consistently calculated  $F_z$ . Clearly, a right choice of  $n_z/n > 1$  (depending on the surface density) would capture quite well the effects of vertical gravity: the flattening of the ring and the strongly enhanced impact frequency. However, with the inclusion of

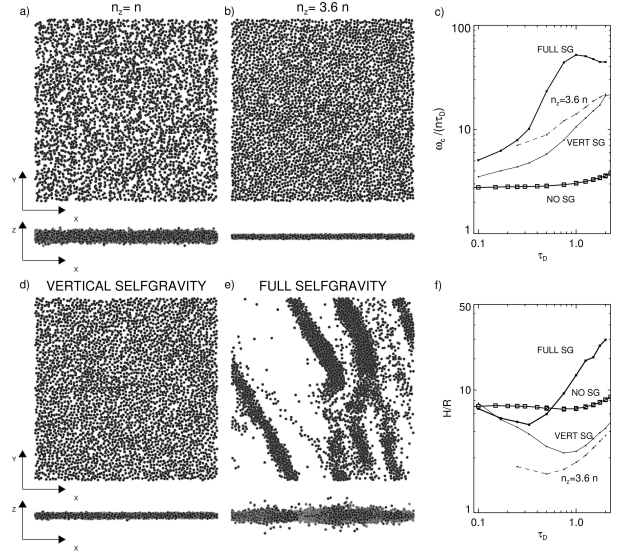


**Figure 1.19** Snapshots from  $2\lambda_T \times 2\lambda_T$  simulations with  $\tau_D = 0.75$ , using the 'frosty' ice elasticity model. In the upper row non-gravitating simulations with a)  $n_z/n = 1$  and b)  $n_z/n = 3.6$ . In the lower left, in d) the vertical component of self-gravity is self-consistently included, while e) the full self-gravity is taken into account. The internal density  $\rho = 900\text{kgm}^{-3}$  which corresponds to  $r_h = 0.82$  at the simulated Saturnocentric distance 100 000 km (see Eq. 1.124). Also shown in c) is the impact frequency (normalized by  $\tau_D n$  and in f) the vertical thickness (averaged over the whole system) as a function of optical depth.

full self-gravity (Fig. 1.19e) the picture is completely different from that when only the vertical component of self-gravity is taken into account. The system now forms gravitational condensations which shear into elongated trailing density enhancements. Such structures, in the context of Saturn's rings, were first simulated in Salo (1992a). However, the phenomenon itself was envisioned already a few decades earlier, in the context of galaxy disks.

Toomre (1964) showed that a self-gravitating differentially rotating disk is locally unstable against the growth of axisymmetric disturbances if its radial velocity dispersion  $c_x$  falls below a critical value  $c_{cr}$ . The closeness to the stability boundary is measured by the Toomre  $Q_T$  parameter

$$Q_T = \frac{c_x}{c_{cr}} = \frac{c_x \kappa}{3.36 G \Sigma} \quad (1.120)$$

While  $Q_T \geq 1$  guarantees stability against the growth of *axisymmetric* perturbations, already for  $Q_T \lesssim 2-3$  the system is susceptible to the growth of local *non-axisymmetric* disturbances (Julian and Toomre, 1966; Goldreich and Lynden-Bell, 1965). Such a near-instability manifests as an emergence of trailing filamentary density enhancements just as those seen in the self-gravitating simulations. As was illustrated in Sect. 1.4, in Keplerian velocity field such wakes form  $\sim 15^\circ - 20^\circ$  angle with respect to the tangential direction, and their radial separation is of the order of Toomre's critical wavelength

$$\lambda_T = 4\pi^2 G \Sigma / \kappa^2. \quad (1.121)$$



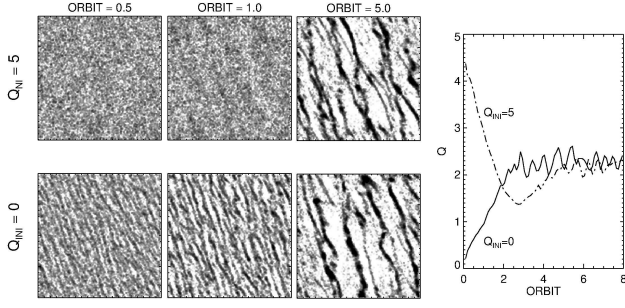


**Figure 1.20** Establishment of statistical steady-state in  $8\lambda_T \times 8\lambda_T$  simulations starting from a hot ( $Q_T = 5$ ) and cold ( $Q_T = 0$ ) uniform initial state. The parameters are  $\tau_D = 0.5$ ,  $r_h = 0.82$ ,  $\epsilon_n = 0.5$ .

Individual filaments are rapidly destroyed by shear, but new condensations are continuously generated. Due to enhanced densities and systematic motions associated with the wakes, the  $\omega_c$  is even more strongly enhanced than in the case of vertical gravity (Fig. 1.19c). Also, the vertical thickness increases as the scattering by wakes more than compensates the flattening caused by the enhanced vertical field (Fig. 1.19f).

Figure 1.20 illustrates the role of wakes/impacts in establishing a ‘thermostat’ which keeps the system near a constant  $Q_T$  regardless of the initial state of the system. In the case of stellar disks, the gravitational scattering accompanying the growing disturbances would heat the system so that the wakes are eventually suppressed. In the case of particulate rings, the collisional dissipation provides a physical regulating mechanism which makes it possible to reach and maintain a statistical steady-state with sufficiently low  $Q_T$ , so that new structures continuously emerge and dissolve in a timescale comparable to the orbital period. As emphasized by Toomre and Kalnajs (1991), the gravity wakes do not represent an instability in the sense that there would be a strict threshold for the emergence of the wakes - rather they manifest the enhanced reactivity of the selfgravitating disk whenever  $Q_T$  is sufficiently small. In particular, any small leading perturbation, while evolving into a trailing one due to shear, is significantly amplified by the interplay of gravity and differential rotation (the ‘swing amplification’ mechanism (Toomre, 1981; Goldreich and Lynden-Bell, 1965).

The self-gravity structures seen in simulations can be interpreted as a superposition of numerous individual Julian and Toomre (1966) wakes, excited by each particle when other particles flow past it - this justifies the name (‘wake’) commonly adopted to the phenomenon. This identification is supported by the 2D auto-correlation analysis of the simulated structures (Toomre and Kalnajs, 1991; Salo, 1995; Salo et al., 2004). To further strengthen the argument, Fig. 1.21 compares auto-correlation functions from ring simulations with the Julian and Toomre (1966) theoretical calculations of the density response around an orbiting mass enhancement, performed for different central shear rates. The trend in the pitch angle of the density crest as a function of  $s/n$  is strikingly similar. Also as expected, the scale of structures is

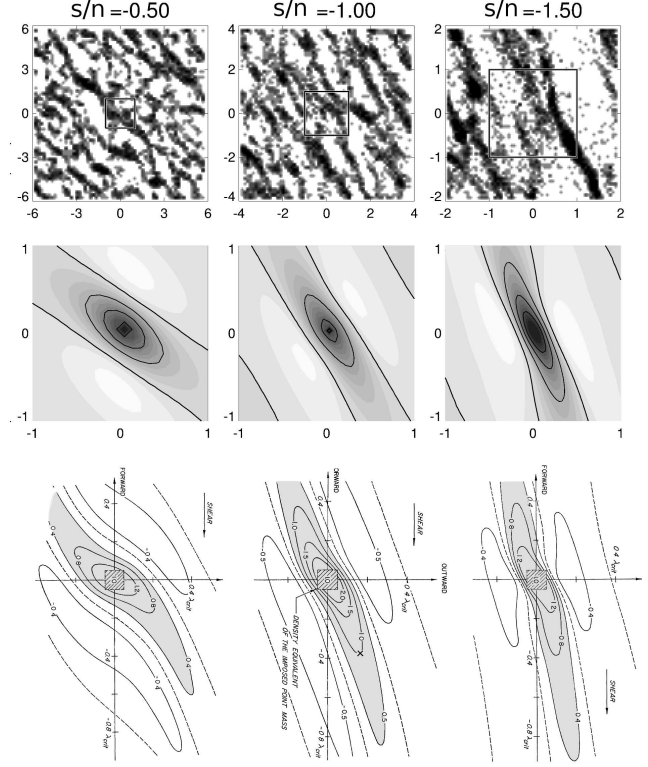


**Figure 1.21** The upper row shows snapshots from simulation with different shear rates  $s$ : the physical width of the calculation region is fixed ( $\sim 170$  particle radii) and corresponds to  $12, 8$ , and  $4\lambda_T$  for  $s/n = -0.5, -1.0$  and  $-1.5$ . The middle row shows 2D auto-correlation plots from the same simulations, covering  $2\lambda_T \times 2\lambda_T$ . The lowermost row shows Julian-Toomre (1966) analytic calculations for the same shear rates of the wake response around an orbiting point mass-point: their graphs have been rotated to same orientation as our simulation plots. In the simulations  $\tau_D = 0.5$ , constant  $\epsilon_n = 0.5$ ,  $r_h = 0.82$ .

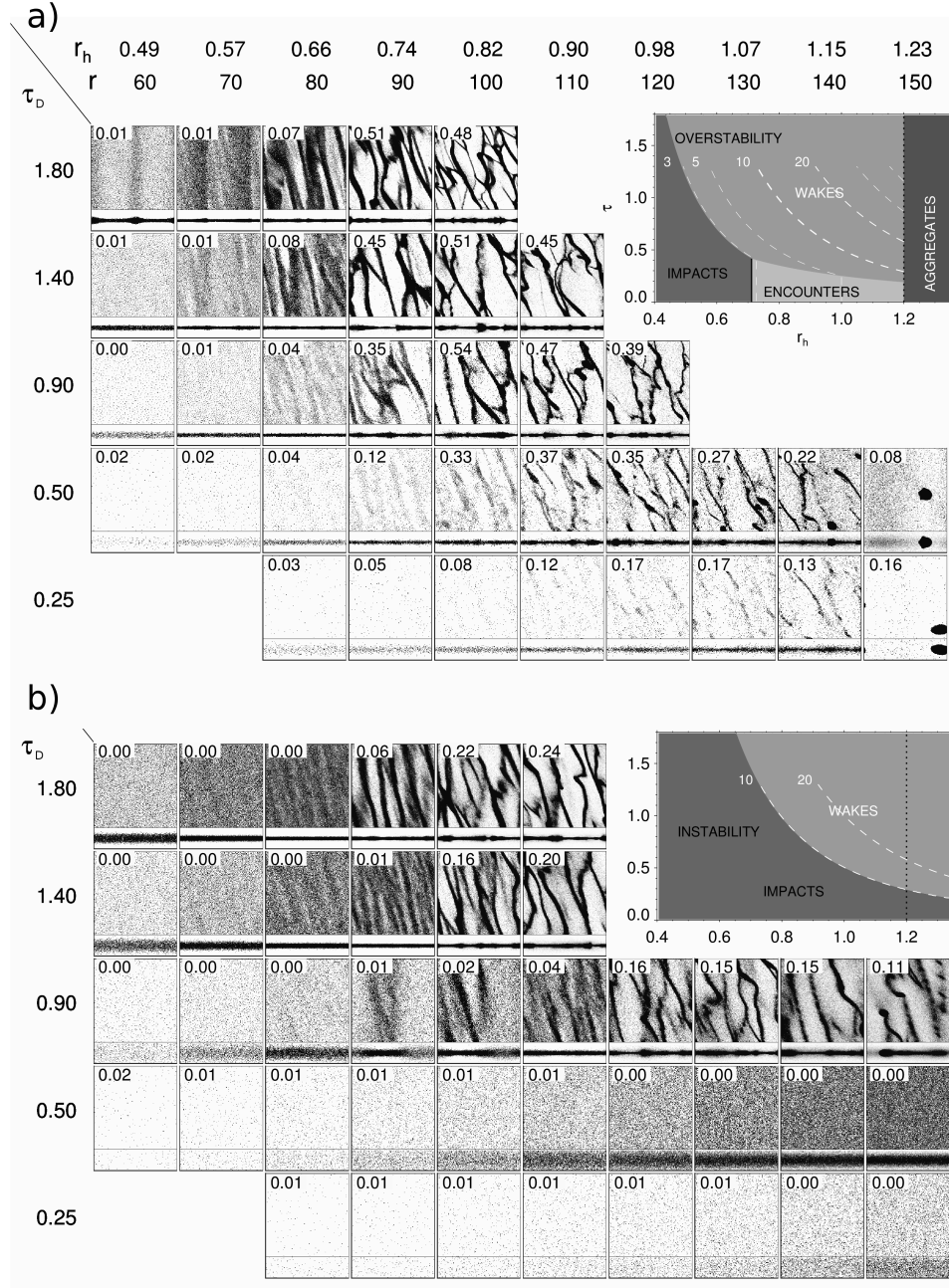
in all cases proportional to  $\lambda_T$ , which is different by a factor of 3 for the studied shear rates ( $\lambda_T \propto (2s/n + 4)^{-1}$ ) according to Eqs. (1.6 and 1.121). A more quantitative comparison is not attempted, since the Julian and Toomre (1966) response-calculations assumed a fixed  $Q_T$  for the disk and did not account for the finite particle size - in simulations of Fig. 1.21 the velocity dispersions adjusts self-consistently to balance the dissipation and viscous gain.

### 1.6.2.2 Survey of self-gravity wakes

In the non-gravitating case the optical depth  $\tau_D$  and the elasticity model determine the ring steady-state for a given particle size distribution (see Sect. 1.6). When self-gravity is included, just one additional parameter is required to characterize both the pairwise and collective gravitational effects. This is the  $r_h$  parameter, the ratio of the mutual Hill-radius for a pair of particles to the sum of their physical radii,

$$r_h(\mu) = \frac{R_H}{R_1 + R_2} = \left( \frac{\rho}{3\rho_{plan}} \right)^{\frac{1}{3}} \left( \frac{r}{r_{plan}} \right) \frac{(1 + \mu)^{\frac{1}{3}}}{1 + \mu^{\frac{1}{3}}}, \quad (1.122)$$





where  $\rho$  is the internal density of the particles, and  $\mu = M_1/M_2 = (R_1/R_2)^3$  is their mass ratio. Here

$$R_H = ((M_1 + M_2)/3M_P)^{1/3} r \quad (1.123)$$

is the radius of the Hill-sphere, inside which the pair's mutual gravity dominates over the tidal pull from the planet at the distance  $r$ . When  $r_h$  decreases, the particle pair extends more and more out from its Hill-sphere:  $r_h = 0$  corresponds to the non-gravitating case, while if  $r_h = 1$  the attraction between two synchronously rotating, radially aligned ring particles in contact equals the disruptive tidal force. For a pair of identical particles  $\mu = 1$ , and inserting the typical

**Figure 1.22** Survey of self-gravity wakes as a function of  $r_h$  and  $\tau_D$ . The labels  $r$  indicate the Saturnocentric distance (in units of 1000 km) for particles with solid ice internal density: for other densities the distances scale  $\propto (\rho/900\text{kgm}^{-3})^{-1/3}$ . The size of the simulation system is  $4\lambda_T \times 4\lambda_T$ , with  $\lambda_T/R \approx 150\tau_D r_h^3$ ; the side view covers  $4\lambda_T \times 1\lambda_T$ . The number of simulation particles  $N \approx 116 \cdot 10^3 \tau_D^3 r_h^6$ . In a) the 'frosty' ice and in b) the 'smooth' ice elasticity model is used. The inserts sketch the regimes where various physical factors dominate, based on the estimates given in the text. The dashed curves indicate what is the radial velocity dispersion which corresponds to  $Q_T = 2$ . In a) the boundary between wakes and impacts is drawn at  $c_r/(nR) = 3$ , while in b)  $c_r/(nR) = 10$  is assumed. Note the region  $\tau_D \gtrsim 1$  and  $r_h \lesssim 0.6$  in a) leading to viscous overstability (see Sect. 1.7.1). Similarly in b) simulations with  $\tau_D = 0.9$ ,  $r_h \sim 0.8$  show viscous instability (see Sect. 1.7.2). The numbers in the frames indicate the amplitude of azimuthal brightness asymmetry for the simulation (see Sect. 1.8.4)

numerical values for Saturn's rings gives

$$r_h(\mu = 1) = 0.82 \left( \frac{M_P}{5.69 \cdot 10^{26} \text{ kg}} \right)^{-\frac{1}{3}} \left( \frac{\rho}{900 \text{ kgm}^{-3}} \right)^{\frac{1}{3}} \left( \frac{r}{100 \text{ 000 km}} \right). \quad (1.124)$$

We will denote  $r_h(\mu = 1)$  simply by  $r_h$ . For  $\mu = 0$  or  $\mu \rightarrow \infty$  (a test particle attached to surface of a large particle), the  $r_h$  would be a factor  $2^{2/3} \approx 1.59$  larger. With the formula 1.124, the simulation results for a given  $r_h$  can be scaled to any other  $\rho^{1/3}r$  combination.<sup>8</sup>

To demonstrate that  $r_h$  is the only additional parameter needed to characterize self-gravity wakes, we may write the Toomre critical wavelength and velocity dispersion as

$$\frac{\lambda_T}{R} = 48\pi \tau_D r_h^3, \quad (1.125)$$

$$\frac{c_{cr}}{nR} = 12.8 \tau_D r_h^3. \quad (1.126)$$

Here we have assumed identical particles; in case of size distribution the numerical pre-factors would depend on  $dN/dR$ . Similarly, the minimum velocity dispersion maintained by gravitational encounters,  $c_{enc} \sim v_{esc}$ , where  $v_{esc} = \sqrt{2GM/R}$  is the 2-body escape speed, can be expressed as

$$\frac{c_{enc}}{nR} = 4.9 r_h^{3/2} \quad (1.127)$$

Figure 1.22a depicts a simulation survey of wake structures for the 'frosty' ice elasticity model. The strength of wakes increases when the optical depth  $\tau_D$ , or the distance (measured with  $r_h$ ) increases. The wakes get clumpier and eventually degrade into semi-permanent gravitational aggregates for  $r_h \gtrsim 1.2$ . Same takes place at low  $\tau_D$  via pairwise accumulation. The exact boundary for aggregate formation depends on the elasticity of particles and also the particle size distribution (Salo, 1995; Karjalainen and Salo, 2004). The fact that  $r_h > 1$  is required for stable aggregates to form is because not only shear, but also particle impacts and velocity dispersion act to destroy any forming condensations.

The insert in Fig. 1.22a sketches the parameter regimes where different factors (impacts, encounters, wakes) dominate the dynamics, based on the velocity dispersion this factor alone would be able to maintain (Salo, 1995; Ohtsuki and Emori, 2000). For the frosty ice model (or constant  $\epsilon_n \lesssim 0.5$ ) the minimum velocity dispersion due to impacts is

$$\frac{c_{imp}}{nR} \sim 2 - 3 \quad (1.128)$$

Comparing to Eq. (1.127), we may expect that velocity dispersion is governed by gravitational encounters rather than by physical impacts for  $r_h \gtrsim 0.7$ . A rough criterion for the

<sup>8</sup> This is strictly valid only in the case of constant  $\epsilon_n$ . If  $\epsilon_n = \epsilon_n(v_n/v_c)$ , with a scale parameter  $v_c$ , then the ratio  $nR/v_c$  which determines the relative magnitudes of local and nonlocal viscous gains (see Fig. 1.15) will depend on distance via  $n$ . However, for example for the frosty ice model this dependence is weak and the  $r_h$  scaling works well (see Karjalainen and Salo (2004)).

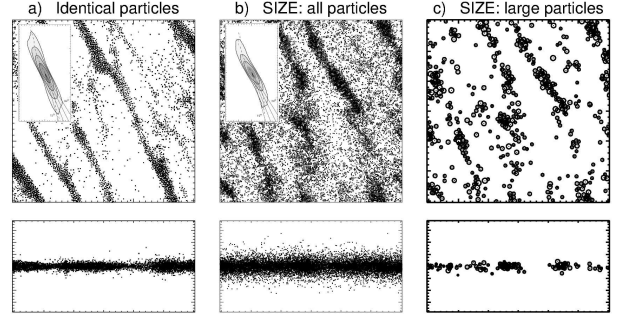


**Figure 1.23** a) Identical particle simulation with  $\tau_D = 0.5$ ,  $r_h = 0.85$ , using 'frosty' particle elasticity model and  $4\lambda_T \times 4\lambda_T$  calculation region. b) Simulation with same parameters, except having a  $q = -3$  power-law size distribution with  $R_{max}/R_{min} = 10$ . c) Particles with  $R > R_{max}/2 = 2.1$  meters are shown separately: they comprise 30% of the optical depth and 55% of surface mass density. The inserts in a) and b) display 2D auto-correlation for the simulations, indicating about  $5^\circ$  larger average pitch angle of wakes in the size distribution simulation.

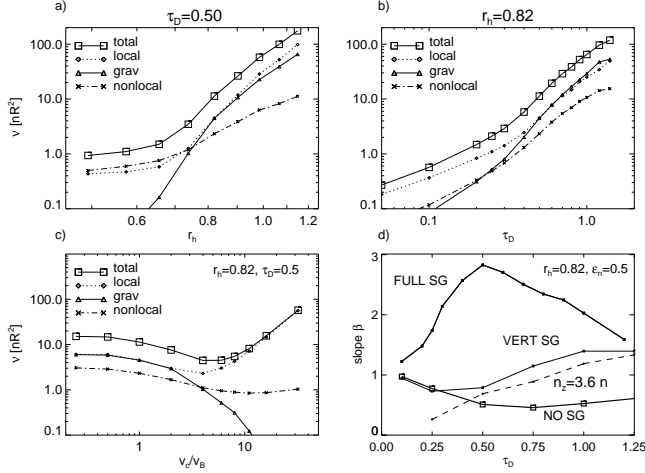
emergence of collective wake-structure is obtained by assuming that wakes become apparent whenever the minimum velocity dispersion drops below  $c_{wake} = Q_T c_{cr}$  with  $Q_T \sim 2$ . According to Eqs. (1.126) and (1.128) this corresponds to  $\tau_D r_h^3 \gtrsim 0.1$ . In the insert figure the condition  $c_{wake} > c_{imp}$  (and  $c_{wake} > c_{enc}$ ) defines the sketched boundary between wakes and impacts (or wakes and encounters). The other dashed curves in the insert indicate where  $Q_T = 2$  corresponds to  $c/(nR) = 5, 10, 20$ .

Figure 1.22b shows a similar survey, except with the 'smooth ice' elasticity model. No wake structures are visible for optical depths  $\tau_D = 0.25$  or  $\tau_D = 0.50$  for any  $r_h$ , but for higher  $\tau_D$  the picture is very similar to that in a). The reason for the suppression of wakes at low  $\tau_D$  is the high velocity dispersion maintained by impacts alone: according to Fig. 1.14, we have  $c/(nR) > 10$  for  $\tau_D \lesssim 1$ . In the inset figure this value is used to delineate the boundary between impacts and wakes. Now the velocity dispersion of the system is too high to allow for bound aggregates to form at any of the studied  $r_h$  values.

The wake structure is also affected by the particle size distribution (Fig. 1.23). For example, the average pitch angle increases when size distribution is included (Salo et al., 2004; French et al., 2007b; Michikoshi et al., 2015). Also, although the large particles still form distinct wakes, the overall contrast is reduced due to the more uniform distribution of small particles. This implies that at least in principle a system can exhibit dynamically significant wake structure, though it might be almost hidden in photometric observations (Salo et al., 2004).

### 1.6.2.3 Gravitational viscosity

The effect of gravity wakes on viscosity is depicted in Fig. 1.24. The upper row compares self-gravitating simulations with constant  $\epsilon_n = 0.5$  as a function of  $r_h$  and  $\tau_D$ . For



**Figure 1.24** Comparison of various contributions to total viscosity, in a) as a function of  $r_h$  and b) as a function of  $\tau_D$ . They are from a constant  $\epsilon_n = 0.5$  simulations similar to Fig. 1.22. In c) the viscosity as a function of scale parameter  $v_c$  in velocity-dependent elasticity model  $\epsilon_n(v_n) = (v_n/v_c)^{-0.234}$ ; with  $v_c = v_B = 0.000077 \text{ m/s}$  this corresponds to the Bridges et al. (1984) ‘frosty’ ice model. Frame d) displays the slope of  $\nu \propto \tau_D^\beta$  in simulations of frame b), reaching values  $\beta \approx 2 - 3$  in selfgravitating simulations; also non-gravitating simulations and simulations including only the vertical self-gravity are shown.

$\tau_D \gtrsim 0.5$  and  $r_h \gtrsim 0.75$ , the  $\nu_{grav}$  contribution associated with the gravitational torques from inclined wakes becomes dominant (Daisaka et al., 2001; Tanaka et al., 2003). Also  $\nu_{local}$  is strongly enhanced due to systematic motions associated with the wakes, whereas the  $\nu_{nl}$  has less significance. The results of Fig. 1.24 agree with the trend originally found in Daisaka et al. (2001),

$$\nu_{tot} \approx (\nu_{grav} + \nu_{local}) \approx 2\nu_{grav} \propto \frac{r_h^5 G^2 \Sigma^2}{n^3}. \quad (1.129)$$

The  $\Sigma^2$  ( $\propto \tau_D^2$  in the figure) dependence is similar to the standard continuum fluid formula for spiral torques in galaxy disks (Lynden-Bell and Kalnajs, 1972), while the  $r_h$  dependence can be interpreted as an extra effect related to the finite size of particles: the smaller the  $r_h$ , the closer is the scale of wakes compared to physical size of particles (see Eq. 1.125). This limits the maximum contrast the wakes can attain as the density of wakes is limited by the internal density of particles. The estimates of Saturn’s ring viscosity in Tiscareno et al. (2007), based on the damping of A ring satellite density waves are in good agreement with Eq. (1.129).

The slope of  $\nu(\tau_D)$  relation is shown in more detail in Fig. 1.24d and also compared with non-gravitating simulations and to simulations including only the vertical component of self-gravity (compare to Fig. 1.19). With the inclusion of self-consistent vertical gravity the slope  $\beta \gtrsim 1$  for  $\tau_D \gtrsim 1$ , which is higher than in the non-gravitating case ( $\beta \approx 0.5$ ), but clearly smaller than with full-self-gravity ( $\beta \approx 2$ ). Note that when using  $n_z/n$  to mimic vertical gravity, the value of  $\beta$  can be increased by choosing a larger enhancement factor.

Based on Fig. 1.22 it is clear that the gravitational viscosity depends strongly on the adopted elasticity model. In Fig. 1.24c this is illustrated by comparing simulations with different  $\epsilon_n(v_n)$  models, parameterized by the velocity scale factor in the Bridges et al. (1984) type elasticity law (‘frosty ice’ model has  $v_c/v_B = 1$ ; the ‘smooth ice’ model would correspond to  $v_c/v_B \sim 30$ ). The more inelastic the impacts are, the larger is the contribution from gravitational viscosity. For the simulated  $\tau_D = 0.5$ , the gravitational viscosity is completely negligible for  $v_c/v_B = 30$ , in agreement with the total absence of wake structure in the simulations depicted in 1.22b. At the same time for very elastic impacts the local viscosity increases proportional to  $(v_c/v_B)^2$ . This follows as the system tries to establish a thermal balance with a mean elasticity whose value depends on the optical depth via the Goldreich-Tremaine formula. The resulting steady-state  $c$  is proportional to  $v_c$  and thus  $\nu_{tot} \approx \nu_{local} \propto v_c^2$ . Because of the opposite trends of  $\nu_{local}$  and  $\nu_{grav}$ , and the relatively insignificant role of  $\nu_{nl}$ , the total viscosity has a minimum at intermediate  $v_c/v_B \approx 3$ .

## 1.7 Viscous instability and overstability

The Voyager and Cassini data have revealed overwhelming amount of structure in Saturn’s rings. Some of the structure is unambiguously connected to resonance perturbations by external satellites (in particular in the outer A ring), but the majority of the finest optical depth variations, extending down to shortest resolved length scales, are likely to have some internal origin.

Right after Voyager discoveries *viscous instability* was evoked to explain the intrinsic variations (Lukkari, 1981; Lin and Bodenheimer, 1981; Ward, 1981; Hämeen-Anttila, 1982). In this type of instability (see Fig. 1.25), the collisional flux of particles, proportional to dynamic viscosity  $\eta = \nu\tau_D \propto \tau_D^{\beta+1}$ , is directed toward density maxima (equivalent to  $\beta < -1$ ). Thus any small density fluctuation is amplified by collisional diffusion, in contrast to a stable ring where diffusion smooths density variations. In the non-linear limit the growth of fluctuations is saturated to a state where the flux from dense but dynamically cool ringlets is balanced by the flux from rarefied, dynamically hot regions. This model was soon discarded, mainly as the first laboratory measurements (Bridges et al., 1984) indicated too dissipative particles for the instability mechanism to work (Wisdom and Tremaine, 1988; Araki and Tremaine, 1986). Also, the observed structures do not quite agree with the predictions of simple instability models, according to which the ring should separate into high  $\tau_D$  ringlets surrounded by almost empty gaps (Hämeen-Anttila, 1978).

Other alternatives for explaining the ring fine structure gained more attention, among them the possibility that dense rings might be viscously overstable (Borderies et al., 1985; Longaretti and Rappaport, 1995). In the axisymmetric *overstability* the radial particle flux is directed away from density maxima, like in a stable ring (see Fig. 1.25). However, the flux now increases so strongly with density (large



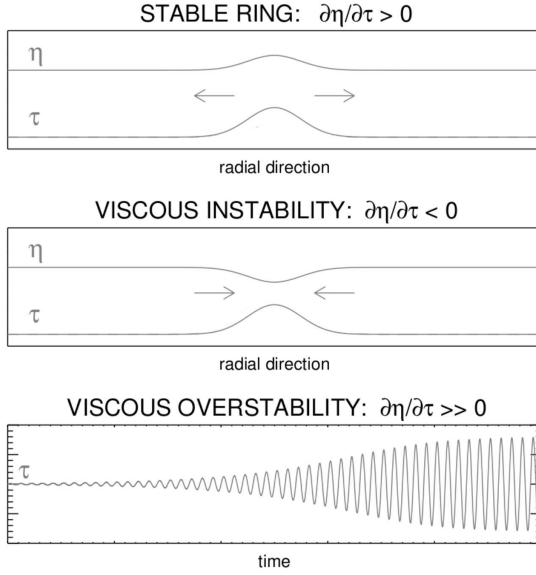


**Figure 1.25** Schematic illustration of viscous stability properties. The radial mass flux is proportional to  $-\partial\eta/\partial\Sigma$ , where  $\eta$  is the dynamic viscosity and  $\Sigma$  is the surface mass density. This indicates that the ring tries to establish a locally constant  $\eta$  profile. In stable ring  $d\eta/d\Sigma > 0$  so that local density fluctuation are smoothed, in contrast to  $d\eta/d\Sigma < 0$  which leads to *viscous instability*. However, if  $d\eta/d\Sigma >> 0$  the suppression overshoots leading to periodic oscillations with amplitude growing with time until saturated at some finite value (*viscous overstability*). In case of non-selfgravitating system optical depth  $\tau_D$  replaces  $\Sigma$  and  $\eta$  is obtained from kinematic viscosity as  $\eta = \tau_D \nu$ .

$\beta$ ), that the system overshoots in trying to smooth the density variations: this leads to density oscillating with time. Although it appears unlikely that overstability could account for large scale structures in the densest rings (Latter and Ogilvie, 2010), there are clear indications of small-scale  $\sim 100$  meter axisymmetric oscillations in moderate  $\tau$  locations in the rings (Colwell et al., 2007; Thomson et al., 2007; Hedman et al., 2014) likely to be related to such overstable oscillations.

### 1.7.1 Viscous overstability (Oscillatory instability)

Early hydrodynamical models for Saturn's rings predicted that practically any flattened ring system with  $\beta \gtrsim 0$  should be overstable (Schmit and Tscharnuter, 1995, 1999), manifesting as axisymmetric oscillations in density and velocity components. The mechanism itself can be confirmed in direct N-body simulations (Fig. 1.26, Salo et al., 2001; Daisaka et al., 2001), which however indicate considerably more stringent conditions for the onset of overstability.

In non-gravitating simulations, and in simulations including vertical self-gravity, the condition (Salo et al., 2001; Schmidt et al., 2001)

$$\beta \gtrsim 1 \quad \text{overstability condition (non - gravitating)}$$

seems to provide a sufficient condition for the onset of overstability, provided that the size of the system exceeds the

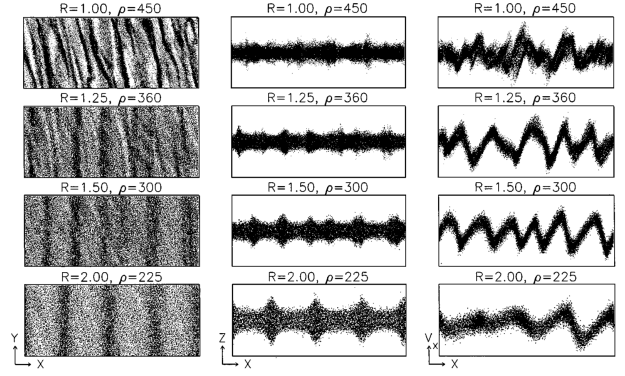


**Figure 1.26** Snapshots from self-gravitating simulations for  $\tau_D = 1.4$ , smooth ice elasticity model, using a  $10\lambda_T \times 4\lambda_T$  calculation region. The top and side snapshot of the system and the radial velocity profile after 50 orbital periods are shown, for four simulations with  $\rho = 450, 360, 300, 225 \text{ kg m}^{-3}$ . For the saturnocentric distance  $a = 100\,000 \text{ km}$  these correspond to  $r_h = 0.651, 0.605, 0.569, 0.517$ , respectively. Figure from Salo et al. (2001).

shortest scale of overstable oscillations, about 100 particle radii. For example, in the non-gravitating simulations with the 'frosty ice' elasticity model have  $\beta > 1$  if  $\tau_D \gtrsim 4$  (Fig. 1.14d). Similarly, simulations where vertical self-gravity is approximated with  $n_z/n = 3.6$ , fulfill this condition for  $\tau_D \gtrsim 1$  (Fig. 1.24d). Indeed, in both cases simulations with sufficiently large calculation regions lead to spontaneous growth of overstable oscillations (Salo et al., 2001).<sup>9</sup>

Transport coefficients derived from simulations with different values of  $n_z/n$ , in combination with improved hydrodynamical models (Salo et al., 2001; Schmidt et al., 2001), have been useful in analyzing the linear growth rates of oscillations, and also in allowing analytic treatment of saturation in weakly nonlinear case (Schmidt and Salo, 2003). Significant progress has also been made using the kinetic theory approach (Latter and Ogilvie, 2008). Recently, nonlinear hydrodynamical analysis (Latter and Ogilvie, 2009, 2010) has shown that the wavelength growth of overstable oscillations is limited via interactions of traveling wavetrains at a few hundred meter to kilometer range, the maximum scale increasing with  $\beta$ . The non-gravitating, very large-scale simulations in Rein and Latter (2013) confirm this, and also demonstrate the richness of structures that result from the non-linear interaction of such wavetrains.

However, it is still unclear what the overstability condition for a fully self-gravitating ring is. The simulations in Salo et al. (2001) indicate that self-gravitating systems may exhibit overstability for  $\tau_D \gtrsim 1$ , but *only if the wake-structure is not too strong*. For example, in the survey of Fig. 1.22a, overstability is seen only in the upper left corner with  $r_h \lesssim 0.6$ . For stronger wakes the overstability is

<sup>9</sup> The same condition,  $\beta \gtrsim 1$  holds also in non-gravitating 2D simulations where the steep rise of  $\nu_{nl}$  when the close-packing limit is approached, makes the system strongly overstable already for  $\tau_D \gtrsim 0.4$ . This fact was utilized in Salo (2001) to directly demonstrate the overstability mechanism, before it was technically feasible in 3D simulations.

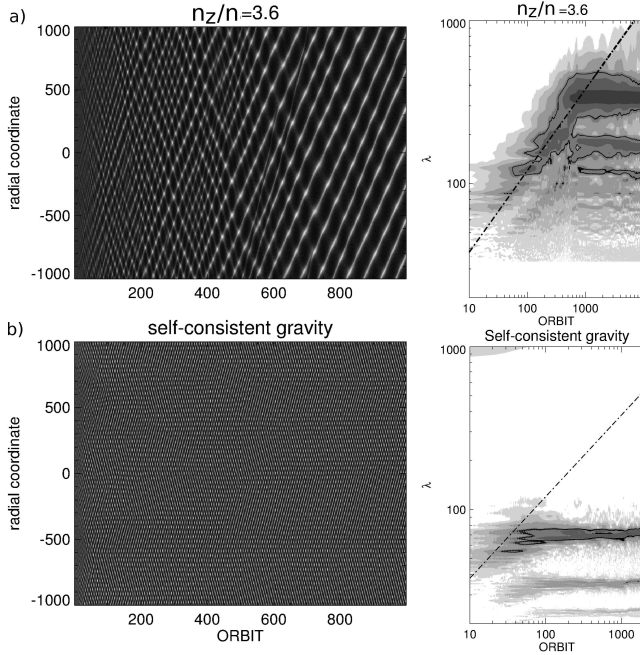


**Figure 1.27** Comparison of overstable oscillations in  $L_x = 2$  km wide non-gravitating and self-gravitating simulations ( $\tau_D = 1.2$ , ‘frosty’ ice). The frames in left show the evolution of the density profile with time, while in the right the amplitude spectrum ( $A_m(\lambda)$  in Eq. (1.74) is shown. In a) vertical self-gravity is mimicked with an enhanced  $n_z/n = 3.6$ . This leads to overstable oscillations whose radial wavelength grows until  $\sim 400$  meters. In b) gravity is treated self-consistently ( $r_h = 0.57$ ), and now the growth of overstable oscillations is limited to less than 100 meters. In the amplitude spectra the 10% contour is indicated with thick line. The dashed line in a) indicates the radial wavelength with the largest amplitude during the initial growth period. For comparison, the same line is also shown in b).

clearly suppressed (see also Fig. 1.26), although the overstability condition for non-gravitating rings,  $\beta \gtrsim 1$ , should be satisfied with ample margin (see Fig. 1.24d). This suppression might be related to different phase and pitch angle of the velocity and density oscillations for overstability and wakes, combined with the fact that they occur at practically similar wavelength range. In any case, even an approximate analytic theory is missing, making fully self-gravitating numerical simulations indispensable in looking the interplay of wakes/overstability.

As mentioned above Rein and Latter (2013) recently carried out simulations with radially very extended calculations regions (radial width even 50 km), facilitating the detailed study of interactions between non-linear wavetrains. However, these simulations use the  $n_z/n > 1$  approximation, and it is not clear how realistically they describe self-gravitating rings. Fig. 1.27 compares this approximation with the fully self-consistently calculated gravity, in moderately large-scale simulations (radial width 2 km). In the former case the evolution is similar to Rein and Latter (2013) simulations, leading to formation of traveling wavetrains with increasing wavelengths, until a maximum scale of  $\sim 400$  meters is reached after about 1000 orbital periods. In the begin-

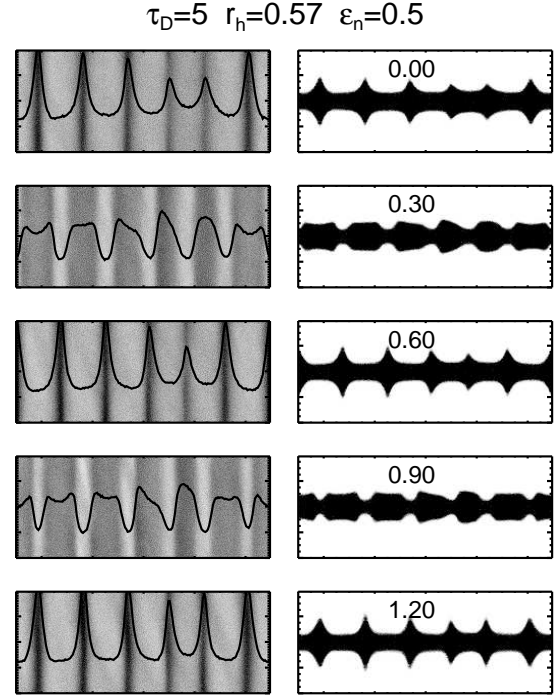


**Figure 1.28** Overstable oscillations followed over one full oscillation cycle ( $\sim 1.2$  orbital periods; the prolongation is due to self-gravity). The calculation region  $10\lambda_T \times 2\lambda_T$ . Note the vertical ‘splashing’ Borderies et al. (1985) associated with the density crests: the ring behaves in a nearly incompressible manner. The vertical scale in the plot is exaggerated by factor 5. Constant  $\epsilon_n = 0.5$  with  $\tau_D = 5, r_h = 0.57$

ning several left and right traveling waves compete, but after about 500 orbits a single traveling mode starts to dominate. The amplitude spectrum indicates that no further wavelength evolution takes place during the span of the simulation (10000 orbits): the shorter modes represent the harmonics of the prevailing mode, related to its non-sinusoidal waveform.

In the self-gravitating simulation with same parameter values (Fig. 1.27b), the initial evolution is quite similar, in addition to weak wakes being superposed with the rapidly evolving axisymmetric overstable oscillations. However, the wavelengths of oscillations do not grow beyond about 100 meter level, although there should be enough time and spatial room for further growth (see the amplitude spectrum). Unfortunately, such self-gravitating simulations are much more time-consuming than non-gravitating runs, since they must have also a tangential width sufficiently large to allow the gravity wakes properly evolve: the simulations with  $n_z/n > 1$  stay axisymmetric so their tangential width can be very narrow.

Figure 1.28 illustrates overstable oscillations over one oscillation period in a dense system ( $\tau_D = 5$ ) with moderate strength of self-gravity ( $r_h = 0.57$ ). Unlike strong self-gravity wakes at larger  $r_h$ , both the maximum and minimum optical depths stay very high ( $\tau_D \gtrsim 2 - 3$ ). If this type of behavior is typical to the densest part of the B ring, then according to the survey of Fig. 1.22 the internal density should



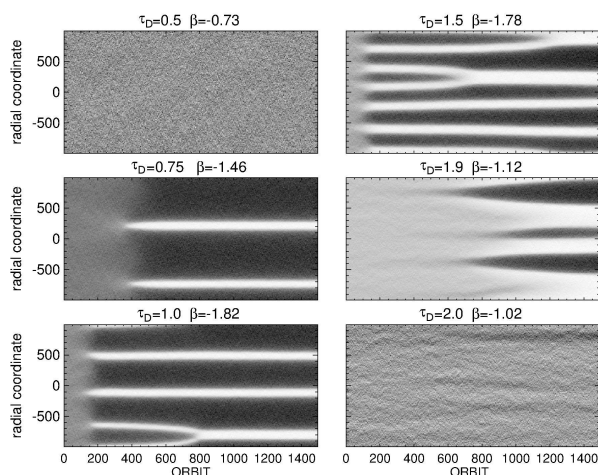


**Figure 1.29** Emergence of viscous instability in large-scale simulations (2km radial extent) using the ‘smooth’ ice elasticity model. The value of  $\beta$  is for the uniform initial state,  $\beta \leq -1$  indicates linear instability. Figure from Salo and Schmidt (2010)

be order of  $\rho \sim 450 \text{ kgm}^{-3}$ , to yield  $r_h \approx 0.6$ . This would require the ring particles to be quite porous. Also, it would seem to rule out very elastic particles.

### 1.7.2 Viscous instability

In the case of viscous instability, the hydrodynamic stability criterion

$$\beta < -1 \quad \text{instability condition}$$

is fully consistent with direct N-body simulations (Salo and Schmidt, 2010), although the shortest unstable wavelengths ( $\sim 200$  particle radii) are about a factor of ten larger than what a simple hydrodynamical linear stability analysis predicts. Figure 1.29 displays large scale (radial width 1 km) simulations, which illustrate how the non-gravitating ‘smooth’ ice elasticity model leads to spontaneous amplification of density fluctuations for  $0.75 \lesssim \tau_D \lesssim 2$ , in very good agreement with the range of  $\tau_D$ ’s where the steady-state  $\beta < -1$  in the small scale simulations of Fig. 1.14. The system is initially uniform and it takes about 100-500 orbital periods for random fluctuations to amplify to a non-linear regime. Fig. 1.22b illustrated that viscous instability may arise also when self-gravity is included provided that  $\beta < -1$  (see the snapshots with  $\tau_D = 0.9, r_h \sim 0.7$ ).<sup>10</sup>

Figure 1.30 depicts in more detail the nonlinear steady-state after the saturation of viscous instability. The state is characterized by a balance of radial particle flux between flattened dense ringlets surrounded by rarefied, large velocity dispersion regions, exactly as envisioned in Hämeen-Anttila (1978). The dynamic viscosity (obtained by tabulating pressure tensor separately at different radial zones)

<sup>10</sup> The same condition applies to 2D systems. Due to different functional form of impact frequency (see Sect. 1.6.1.1) hot 2D systems have  $\beta < -1$  at the limit  $\tau_D \rightarrow 0$ , which makes direct demonstrations of viscous instability numerically much easier than in 3D systems where  $\tau_D \sim 1$  is required (Salo, 2001; Salo and Schmidt, 2010).

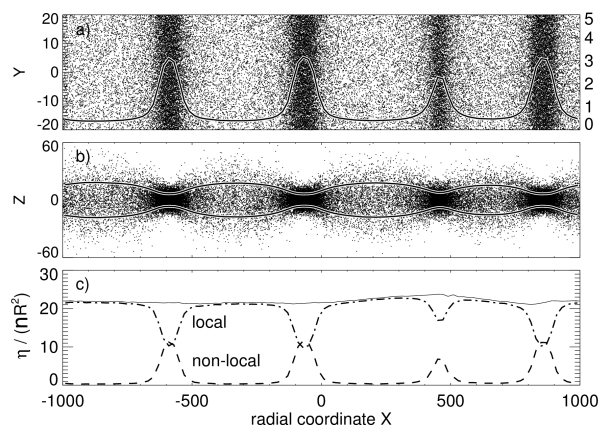


**Figure 1.30** Nonlinear radial balance between dense and rarefied regions resulting from viscous instability. The upper two frames show the top (a) and side views (b) of a simulation with  $\tau_D = 0.92$ , using the ‘smooth ice’ elasticity model. The frame c) depicts the dynamic viscosity profile (solid curve), showing separately the local and nonlocal contributions. Figure from Salo and Schmidt (2010).

has a nearly constant value through the simulation system. Note that one of the ringlets has a slightly lower  $\tau_D$  than the other three. This ringlet corresponds to a small bump in  $\eta$  and is accordingly slowly dissolving. With time, the ringlets slowly merge (see Fig 1.29), their typical separation growing  $\propto \sqrt{t}$ . In contrast to overstability, there is no mechanism known which would stop this growth. Thus at least in principle, large scale structure may emerge as a result of viscous instability.

Nevertheless, viscous instability is typically not regarded as a candidate for the ring fine-structure, basically since it requires fairly elastic particles in order to operate. In such a case the self-gravity wakes are harder to form. Also, the basic instability model in its simplest forms always requires a balance between a rarefied and a dense region, and thus, does clearly not apply, say, to the structure of the dense B ring.

#### 1.7.2.1 Selective viscous instability

There is a variant of the standard instability model that would allow both the minimum and maximum optical depths to be high, namely the possibility of a selective instability of small particles against the more uniform background of larger ones (Stewart et al., 1984). Direct simulations (Salo and Schmidt, 2010) indicate that under certain conditions such a behavior occurs if the coefficient of restitution is smaller in mutual impacts between small particles, than in impacts involving large particles. Such size-dependence of  $\epsilon_n$  adds a new degree of freedom to the system, and in principle allows a balance of radial flux also between two dense regions, provided that they have a different mixture of small and large particles. Importantly, the contrast can also have very different values depending on the details of the elasticity model assumed (Fig. 1.31). Nev-

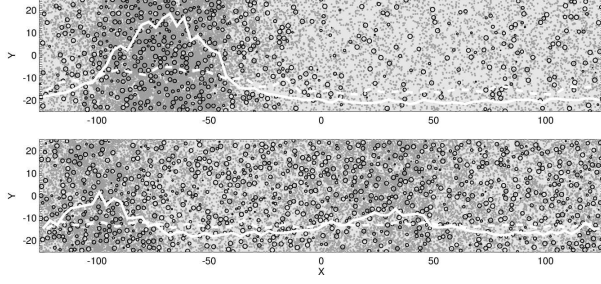


**Figure 1.31** Two examples of *selective viscous instability* in simulations (after 700 orbital periods). The systems consist of two particle sizes with  $R_2/R_1=3$ , and both population have  $\tau_D = 0.5$ . Small (large) particles are indicated by gray (black) color, and the solid (dashed) white curve indicates their radial density profile. In the upper frame the impacts between small particles are much more inelastic than those between large particles, leading to strong density contrast among the small particles. In the lower frame the size-dependence of elasticity is smaller, leading to less pronounced variations. For exact parameter values, see Figs. 21 and 22 in Salo and Schmidt (2010).

ertheless, this mechanism has yet been very little studied, and due to lack of relevant laboratory measurements it remains unclear whether real particles possess suitable size dependence of  $\epsilon_n$  required by this type of instability.

## 1.8 Photometric modeling of dynamical simulation

The dynamical simulations described above operate with surface density and particle number densities. However, these are not directly observable quantities, as the observations give the amount of sunlight reflected or transmitted through the rings, and the attenuation of stellar light when observed through the ring. The ring brightness is measured with  $I/F$ , the observed brightness in comparison to an ideal Lambert surface illuminated with the incident solar flux  $\pi F$ . In general, the  $I/F$  for a given ring region depends on the illumination elevation  $B_\odot$ , the viewing elevation  $B$ , and the corresponding azimuthal angles  $\theta_0$  and  $\theta$ . Often the phase angle  $\alpha$  between the illumination and viewing directions is specified instead of azimuthal angles,

$$\alpha = \cos^{-1} [\cos(\theta - \theta_0) \cos B \cos B_\odot + \sin B \sin B_\odot]. \quad (1.130)$$

In case of homogeneous systems this angle is sufficient. However, in case of self-gravitating systems also the direction with respect to self-gravity wakes matters, so that the azimuths themselves need to be specified. The line-of-sight optical depth relates to the fraction of light  $I/I_0$  passing through the ring at a given direction  $(B, \theta)$ , with

$$\tau_{\text{LOS}} = -\ln I/I_0 \quad (1.131)$$

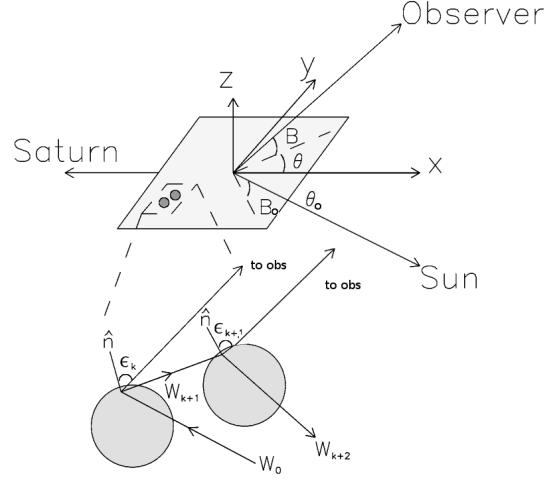


**Figure 1.32** Schematic presentation of Monte Carlo ray tracing: path of a photon, initially arriving from the direction of the sun, is shown through two successive scatterings. The post-scattering direction is Monte Carlo sampled from the single scattering phase function. In each scattering event also the probability of being scattered toward the observer is stored (taking into account the visibility of the observer's direction). Figure from Salo and Karjalainen (2003).

Usually  $\tau_{\text{LOS}}$  is converted to the normal optical depth, corresponding to  $B = 90^\circ$  with the formula

$$\tau_\perp = \tau_{\text{LOS}} \sin B. \quad (1.132)$$

A quantitative comparison of dynamical models to observations requires calculating the photometric properties ( $I/F, \tau_\perp$ ) of the simulated particle fields for various illumination and observing geometries. A large amount of modeling has been done in the framework of classical radiative transfer, which however is strictly applicable only to low filling factor rings ( $D_3 \rightarrow 0$ ) where particle separations are much larger than their sizes. If the rings are densely-packed and highly inhomogeneous, as suggested by dynamical models and many observations (see Dones et al. (1993)), an efficient modeling method is to use radiative ray tracing. Since the ring particles are much larger than visible light wavelength geometric optics can be used. For example the effects of dense packing (Salo and Karjalainen, 2003; Porco et al., 2008) and self-gravity wakes (Salo and Karjalainen, 2003; French et al., 2007b; Porco et al., 2008) have been studied with a combination of photometric and dynamical simulations.

### 1.8.1 Photometric ray tracing method

The idea in photometric ray-tracing simulations is to shoot a large number of photons ( $N_{\text{phot}}$ ) from the light source and follow their paths through successive scatterings from particle surfaces until they leave the particle layer (Fig. 1.32). The simplest way to obtain the brightness would be to count the number of photons  $N_{\text{obs}}$  which leave to the solid angle  $d\Omega_s$  around the observer's direction. However, even if relatively large  $d\Omega_s$  is used (poor angular resolution),  $N_{\text{obs}} \propto \Omega_s N_{\text{phot}}$

would be very small. Since the relative error in  $I/F$  is proportional to  $N_{obs}^{-1/2}$ , such a calculation would be very inaccurate even for a large  $N_{phot}$ . It is therefore crucial to combine such direct ray tracing with an indirect ('backward') method, where each scattering event, regardless of the direction of the post-scattering photon, is registered also from the viewpoint of the observer. If the scattering point is not blocked behind any ring particle, then the contribution of the scattering is added to the observed brightness by calculating what the probability of scattering to the direction of the observer would be. Now in principle every initial photon and scattering event contributes to the obtained  $I/F$ , and the uncertainty in  $I/F$  becomes proportional to  $N_{phot}^{-1/2} \ll N_{obs}^{-1/2}$ . Salo and Karjalainen (2003) estimated that the use of indirect method can speed-up the calculations by a factor  $> 1000$ , for the same accuracy of the results.

The obtained  $I/F$  will depend on the spatial distribution of particles, and on how the individual particles absorb and scatter light. The scattering can be defined either by specifying the surface element's reflection law<sup>11</sup>, or alternatively, via a particle phase function  $P(\alpha)$  which describes the phase angle distribution of emerging photons from a particle as a whole; this corresponds to integrating over the surface elements of the illuminated hemi-sphere. The particle albedo  $A$  gives the total fraction of scattered radiation over all angles.

Photometric ray tracing methods applied to Saturn's rings have been described in detail in Salo and Karjalainen (2003) and in Porco et al. (2008). The main difference of the methods is in the handling of multiple scattering: in the former study in each scattering event a single photon is Monte Carlo sampled from the particle phase function (or surface element's scattering law) to represent the scattered light, whereas in the latter study the light ray is divided in a deterministic fashion into a bundle of rays after each scattering, and each of these new light rays is then followed (and re-divided in the next scattering etc.). The two methods yield similar results, and they have both been verified by extensive comparisons to classical results in the low filling factor limit, both with Chandrasekhar (1960) analytic al single and multiple scattering results and with Dones et al. (1993) calculations with the doubling method. However, the method of Porco et al. (2008) is much more CPU-intensive for a given accuracy since it spends most of the time in the calculation of the higher scattering orders whose contribution to the total  $I/F$  is very small. Since the former Monte Carlo method spends less and less CPU time on each higher scattering or-

der (or at most an equal amount), it can be extended to very high orders of scattering with very little extra CPU-time consumption. The same MC method has been recently adopted in Ciarniello et al. (2014) for testing Hapke (2008) theoretical models.

With the indirect method one can tabulate separately the contributions of different orders of scattering. There is thus no need to specify the albedo before the calculations, but instead one can re-construct the final  $I/F$  for any choice of albedo (Salo and Karjalainen 2003),

$$I = \sum_{k=1}^{max} A^k \Delta I_k, \quad (1.133)$$

where  $\Delta I_k$  is the tabulated contribution from photons after  $k$ 'th scattering and  $A$  is the particle albedo; during the calculation itself the albedo has been treated as unity so that the 'weight' of the photon is kept constant over its path.

The calculation of the photon path through successive scatterings involves finding the intersection points with all particles along the current photon direction, and then choosing the closest intersection for the next scattering. If no intersections are found then the photon leaves the ring layer. The calculation has many similarities with the finding of particle impacts in dynamical simulations. In particular, if the simulated particle field contains a large number of particles it is crucial not to check every particle for a possible intersection. A simple but very efficient solution is to place a 2D grid on top of the particle field, and find first the grid cells the current photon path is crossing, and then search intersections only among the particles in these cells. A 3D grid can also be used, but since the systems of interest are usually very flattened this does not yield significant improvement over a 2D grid.

It is important to take accurately into account the periodic boundaries of the dynamical simulations: when the photon leaves the actual calculation region through its radial or tangential boundaries, it enters an identical copy of the particle field (see Eq. 1.8). Thus the photon should leave (enter) the particle field only from below (above). In practice it is easier to handle the periodic image particles in terms of an image-photon re-entering the original particle field, so that there is no need to store any extra particle locations. The correct treatment of boundaries is particularly important in case of small illumination/viewing angles, where the light rays can, at least in principle, travel very long horizontal distances before leaving the particle layer. Similarly, taking into account periodic images is essential for the calculation of  $\tau_{LOS}$ , in particular when the true probability of passing the particle layer is small: even a few missed intersections might then bias the result.

The brightness due to the illumination by the planet can be calculated in a similar manner as that due to Sun, except that the directions of the incoming photons are sampled from the solid angle extended by the planet. A model for the brightness distribution of the planet's globe is needed: both in Salo and Karjalainen (2003) and in Porco et al. (2008), the Dones et al. (1993) model based on Barkstrom (1973) law was used.

<sup>11</sup> The surface element's reflection law gives the probability  $S(\mu_i, \phi_i, \mu_e, \phi_e) d\mu_e d\phi_e$  that a photon arriving the surface from the direction  $(\mu_i, \phi_i)$  will scatter to an interval  $d\mu_e, d\phi_e$  around the direction  $(\mu_e, \phi_e)$ , where  $\mu_i = \cos(i)$  and  $\mu_e = \cos(e)$ , with  $i$  and  $e$  denoting the angles of incident and emergent rays with respect to the local normal of the surface element at the scattering point, and  $\phi_i$  and  $\phi_e$  are the corresponding azimuthal directions. A simple example is the Lambert reflection law,  $S = S_L(\mu_i, \mu_e) = \mu_e/\pi$ , corresponds to a diffusively scattering surface whose brightness ( $\sim S/\mu_e$ ) is independent of viewing direction. For a spherical particle the integration over the illuminated hemi-sphere gives the corresponding spherical particle Lambert phase function  $P(\alpha) = \frac{8}{3\pi} [\sin \alpha + (\pi - \alpha) \cos \alpha]$ .



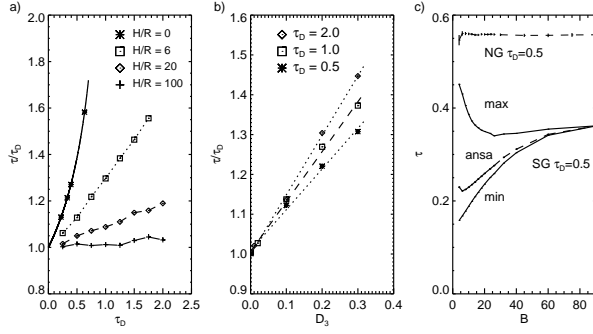


**Figure 1.33** Relation between dynamical and photometric optical depth. In a) and b) homogeneous particle fields were simulated with various  $\tau_D$  and  $H/R$ ; the curve labeled  $H/R = 0$  refers to a 2D monolayer. In c) the self-gravitating simulation depicted in Fig. 1.38 was analyzed, both along the wake major axis direction ('min'), perpendicular to it ('max'), and at the ring ansa. The curve labeled 'NG' refers to a corresponding non-gravitating simulation with  $\tau_D = 0.5$ , yielding practically constant  $\tau_{\perp} \approx 0.55$  for all  $B$ 's. Figure from Salo and Karjalainen (2003); Salo et al. (2004).

## 1.8.2 Examples of photometric modeling

### 1.8.2.1 Dynamical and photometric optical depth

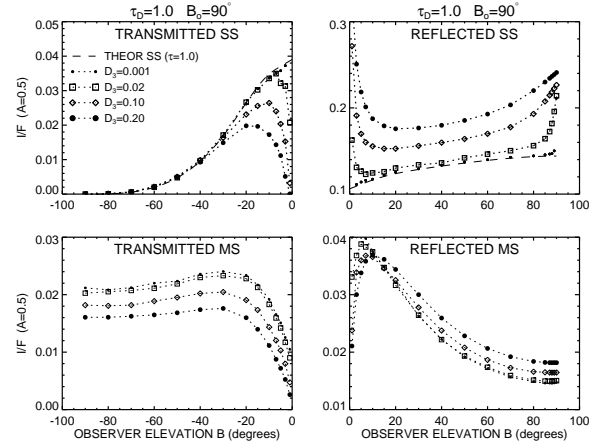
In low volume filling factor rings the vertical thickness of the system is much larger than particle radius: for a planar homogeneous, vertically uniform system of identical particles we have  $H/R = 4\tau_D/(3D_3)$ . At the limit  $D_3 \rightarrow 0$  the photometric and dynamical optical depths are equal. However, for vertically flattened systems the photometric  $\tau_{\perp}$  exceeds  $\tau_D$ . To justify these assertions, consider a vertically extended ring, and divide it into  $k$  layers each contributing  $\Delta\tau_D = \tau_D/k$  to the total dynamical optical depth. The fraction of flight passing through a single layer is  $1 - \Delta\tau_D$ , and assuming that the layers are independent, the fraction of light passing through all layers is  $(1 - \tau_D/k)^k \rightarrow \exp(-\tau_D)$  as  $k \rightarrow \infty$ . Clearly the two definitions of optical depth are then equal. On the other extreme, consider a 2D monolayer with  $k = 1$ . Now  $\tau_{\perp} = -\ln(1 - \tau_D) > \tau_D$ .

Figure 1.33, based on quantitative ray tracing calculations (Salo and Karjalainen, 2003), illustrates the dependence of  $\tau_{\perp}/\tau_D$  on  $D_3$  and  $\tau_D$ . The particle fields in a) and b) were constructed by random placing of identical non-overlapping particles into a cuboidal volume. In the case of many particle thick layer ( $H/R = 100$  in the figure; implies  $D \sim 0.01$ ) we have  $\tau_{\perp} \approx \tau_D$ , but as  $H/R$  is reduced  $\tau_{\perp}/\tau_D$  increases. Similar result holds also for realistic dynamical simulations with vertically non-uniform particle distribution, although in the case of size distribution the difference between  $\tau_{\perp}$  and  $\tau_D$  is somewhat decreased with increasing  $R_{\max}/R_{\min}$ . As a rule of thumb,

$$\tau_{\perp}/\tau_D \approx 1 + kD_3, \quad \text{with } k = 0.7 - 1.5, \quad (1.134)$$

in good agreement with the theoretically estimated enhancement factor of  $1/(1 - D_3)$  (Esposito, 1979).

Photometric simulations also show that Eq. (1.132) for converting slanted  $\tau_{\text{LOS}}$  to  $\tau_{\perp}$  works well for non-gravitating



**Figure 1.34** The effect of non-zero  $D_3$  on the brightness of perpendicularly illuminated layer. Lambert phase function is used with  $A=0.5$ . Monte Carlo simulations with  $\tau_D = 1$  for four different non-zero filling factors ( $D_3 = 0.001, 0.02, 0.10, 0.20$ ) are compared. Single scattering and multiply scattered fluxes are shown separately. Also shown are theoretical  $I_{ss}(D_3 = 0)$  for  $\tau_{\perp} = 1.0$ . Figure from Salo and Karjalainen (2003)

simulation systems, regardless of their vertical flattening (excluding strict monolayers, see (Salo and Karjalainen, 2003)). On the other hand, in the case of self-gravity (Fig. 1.33c), the deduced  $\tau_{\perp}$  depends on the observing elevation and the direction with respect to wakes (Salo et al., 2004; Robbins et al., 2010; Tiscareno et al., 2010).

### 1.8.2.2 Non-zero volume density and enhanced single-scattering

Besides optical depth, non-zero volume density has a significant effect on the observed  $I/F$ . In general, a reduced ring vertical thickness leads to brightening of the reflected component and reduction of the transmitted one. In Fig. 1.34 the upper row shows the reflected and transmitted single scattering components for various values of  $D_3$ , in comparison to theoretical values at the limit  $D_3 \rightarrow 0$ ,

$$\begin{aligned} \left(\frac{I_{ss}}{F}\right)_{refl} &= \frac{AP(\alpha)\mu_0}{4(\mu + \mu_0)} \left(1 - \exp\left[-\tau_{\perp}\left(\frac{1}{\mu} + \frac{1}{\mu_0}\right)\right]\right), \\ \left(\frac{I_{ss}}{F}\right)_{trans} &= \frac{AP(\alpha)\mu_0}{4(\mu - \mu_0)} (\exp[-\tau_{\perp}/\mu] - \exp[-\tau_{\perp}/\mu_0]) \\ &= \frac{AP(\alpha)\tau_{\perp}}{4\mu_0} \exp[-\tau_{\perp}/\mu_0], \quad (\text{if } \mu = \mu_0) \end{aligned} \quad (1.135)$$

where  $\mu_0 = |\sin B_{\odot}|$  and  $\mu = |\sin B|$ . The calculations in the figure use perpendicular illumination  $B_{\odot} = 90^\circ$ , but similar qualitative results hold for slanted illumination geometries. Also, Lambert phase function is assumed, although the ring particles are known to be more strongly backward-scattering (see Dones et al. 1993); the used phase function does not affect the relative change of  $I_{ss}$ . According to the figure, the calculated  $I_{ss}$  agrees with the theoretical value at  $D_3 \approx 0$  but is significantly larger for non-zero  $D_3$ ; for ho-



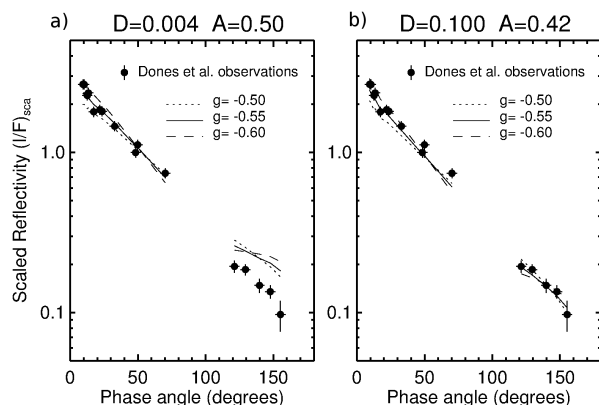


**Figure 1.35** In a) Voyager observations at 122 500 km are compared with  $D_3 \approx 0$  models, using same power-law phase functions as the classical radiative models in Dones et al. (1993). The anisotropy parameter  $-1 \leq g \leq 1$  describes how strongly backward scattering the particles are:  $g = -1$  means perfectly backscattering particle. A particle albedo  $A = 0.5$  matches well the low  $\alpha$  brightness but overestimates the high  $\alpha$  brightness by a factor of 2. In b)  $D_3 = 0.1$  and the models can now match both low and high  $\alpha$ , provided that a somewhat smaller albedo is assumed. The plot uses scaled reflectivity  $4(\mu + \mu_0)/\mu_0 \times (I/F)$ , so that observations with different  $\mu, \mu_0$  can be combined. Figure from Salo and Karjalainen (2003).

homogeneous systems the enhancement in  $I_{ss}$  at intermediate viewing elevations is about 30% for  $D_3 = 0.2$ . The enhancement is particularly strong at small phase angles (here close to  $B = 90^\circ$ ), which is the well-known shadow-hiding opposition effect: as the zero phase angle is approached, the shadows cast by particles are hidden by the particles themselves. The shadow-hiding opposition peak extends to larger phase angles as  $D_3$  increases, in good agreement with theoretical models in Lumme and Bowell (1981). The figure also shows an enhancement of  $I_{ss}$  near  $B = 0^\circ$ : this is somewhat specific to the perpendicular illumination, and follows from the fact that at low viewing angles mainly the illuminated upper surfaces of the outermost particles are visible.

In simulations with realistic size distributions the enhancement  $I_{ss}(D_3)/I_{theory}$  decreases when the width of the size distribution is extended. This reduction is related to the effective  $D_3$  at the vertical layer where  $\tau_{LOS} \sim 1$ , responsible for most of the reflected light. As illustrated in Salo and Karjalainen (2003), the effective  $D_3$  gets smaller when more extended distributions are simulated. Because of this, the angular width of the opposition brightening is reduced, in good agreement with Hapke (1986) theoretical estimates. For the same reason, the opposition peak becomes narrower for lower viewing elevations:  $\tau_{LOS} \sim 1$  is achieved at more rarefied upper layers. In practice, dynamical/photometric simulations indicate

$$HWHM \propto B, \quad (1.136)$$

where  $HWHM$  is the Half-width half-maximum of the opposition peak (Salo and French, 2010).

Dones et al. (1993) pointed out problems when trying to explain Voyager observations of Saturn's ring photometry in

the framework of classical radiative transfer, such as matching simultaneously the low and high phase angle  $I/F$  of the B and the inner and middle A ring: the rings appeared too dark at high  $\alpha$  compared to what the classical models fitted at low  $\alpha$  predicted (Fig. 1.35a). They proposed that the discrepancies stem from vertical flattening of the rings. Indeed, when including the enhancement of  $I_{ss}$  due non-zero  $D_3$ , the fit to the observed low phase  $I/F$  indicates a smaller  $A$ . This leads to reduced multiple scattering and thus smaller high phase brightness since this is mainly due to  $I_{ms}$ . Also, the nonzero  $D_3$  itself reduces the high  $\alpha$  multiple scattering compared to that in the classical limit: together these two effects bring the model and observations to a good match (Salo and Karjalainen, 2003, Fig. 1.35b). Similar conclusion was reached by Porco et al. (2008).

### 1.8.3 Opposition brightening

Saturn's rings show a strong opposition effect: a steep rise in  $I/F$  when the Sun-observer phase angle  $\alpha \rightarrow 0^\circ$ . Hubble Space Telescope observations during the 2005 opposition (French et al., 2007a) indicated that the brightness increase continues all the way to zero phase angle: the  $I/F$  increases by about 2/3 for  $\alpha < 6^\circ$ , half of this increase taking place within  $\alpha < 0.5^\circ$ . Most strikingly the opposition 'spike' is demonstrated by the zero-phase Cassini images (Déau et al., 2013), which show a bright localized spot on the ring location centered at exact opposition.

Two main explanations for the Saturn ring's opposition brightening are i) the reduced amount of mutual *interparticle* shadowing, and ii) the *intrinsic* brightening of the ring particles themselves. As demonstrated by Fig. 1.34, the mutual shadow hiding effect is inevitable in a densely packed ring, although it depends on the spatial and size distribution of ring particles whether the brightening is as strongly peaked at  $\alpha = 0^\circ$  as observed. Similarly, theoretical and laboratory studies suggest that icy particles exhibit a significant intrinsic brightening at  $\alpha \rightarrow 0^\circ$  due to constructive interference between the incoming and outgoing light rays (coherent backscattering (CB), see e.g. Hapke, 1990; Mishchenko, 1992; Nelson et al., 2000). The expected magnitude and width of CB depends on the surface structure and optical properties of particles. Rough particle surfaces can also exhibit an intrinsic shadow hiding effect.

A long-term challenge has been to separate interparticle and intrinsic contributions to the opposition effect: unless this can be done it is not possible to extract reliable information of the particle surface properties by fitting the observed curves with theoretical CB models, without including the interparticle shadow hiding (see e.g. Poulet et al., 2002; Déau, 2015). Likewise, the early volume density estimates for Saturn's rings ( $D_3 \approx 0.02$ , Lumme et al. (1983)), based on interpreting the brightening solely in terms of interparticle shadow hiding were prone to lead to wrong answers.

The expected functional forms of the intrinsic and interparticle opposition effects are very similar (see e.g. Hapke, 1986, 1990), so that their contributions can not be entangled based on an individual phase curve. However, such a separation becomes possible with multi-wavelength observations

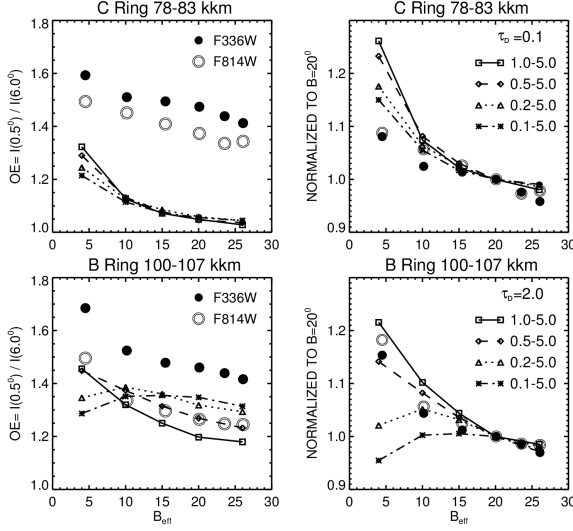


**Figure 1.36** In the left: The symbols show the near-opposition brightness enhancement in HST observations of Saturn’s C and B rings, measured in terms of  $OE = I(\alpha = 0.5^\circ)/I(\alpha = 6^\circ)$ . Lines indicate the modeled  $OE$  in size distribution simulations with different  $R_{min}$  (all have  $R_{max} = 5\text{m}$  and  $q = 3$ ). In the right, the  $OE$  is normalized with that at  $20^\circ$  opening angle: note that normalized  $OE$  is practically independent of the wavelength. Figure from Salo and French (2010).

covering a whole range of observing/illumination elevations. Namely, while the interparticle shadowing effect depends on  $B$  (Eq. (1.136)), it should be independent of the wavelength  $\lambda$ . On the other hand,  $CB$  is expected to depend on  $\lambda$  but not on  $B$ .

Salo and French (2010) exploited the full set of Saturn ring phase curves obtained with the Hubble Space telescope WFC2 instrument during 1996–2005 (Cuzzi et al., 2002; Poulet et al., 2002; French et al., 2007a). In this data set, covering  $4.5^\circ < B_{\text{eff}} < 26^\circ$  in 5 broadband filters, the opposition brightening gets significantly more pronounced as  $B_{\text{eff}}$  decreases, confirming the expected contribution of interparticle shadowing.<sup>12</sup> Fig. 1.36 illustrates this in terms of  $OE = I(0.5^\circ)/I(6^\circ)$  for ring regions selected from the C and B rings. Both rings exhibit clearly larger  $OE$  at  $B_{\text{eff}} = 4.5^\circ$  compared to larger opening angles (left frames). The relative increase of  $OE$  with elevation is also independent of wavelength, as seen when  $OE$  is normalized to its value at  $B_{\text{eff}} = 20^\circ$  (right frames).

The Fig. 1.36 shows also results from a grid of dynamical/photometric simulations performed for different  $\tau_D$ ’s and different size distributions. For example, the  $B_{\text{eff}}$  dependence of the C ring  $OE$  is best matched with  $\tau_D \sim 0.1$  and a wide size distribution with  $R_{min}/R_{max} \lesssim 0.01$ . On the other hand, the B ring comparisons suggest  $\tau_D \gtrsim 2$  and a much narrower distribution  $R_{min}/R_{max} \gtrsim 0.1$ .

<sup>12</sup> The HST observations at slightly different  $B, B_\odot$  are reduced to a geometrically corrected  $(I/F)_{\text{corr}}$  corresponding to an effective common elevation angle  $B_{\text{eff}}$ , defined by  $\mu_{\text{eff}} = 2\mu\mu_0/(\mu + \mu_0)$  and  $(I/F)_{\text{corr}} = \mu_{\text{eff}}/\mu(I/F)$ . With this transformation the theoretical  $(I/F)_{\text{corr}}$  depends only on  $B_{\text{eff}}$ .

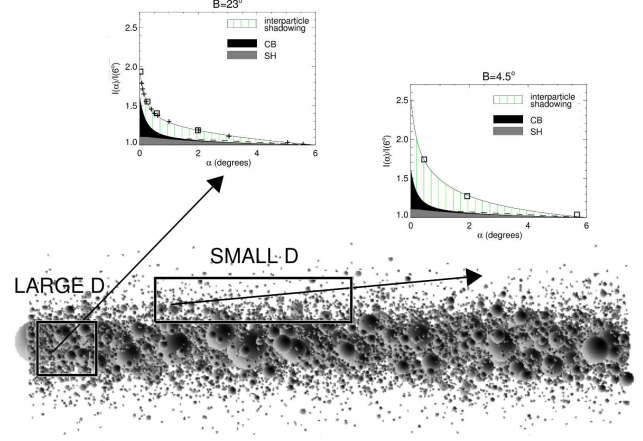


**Figure 1.37** Illustration of the opening angle dependence of opposition phase curves (normalized by  $I/F(\alpha = 6^\circ)$ ). A sideview of a dynamical  $\tau_D = 1.25$  model is displayed, together with HST phase curves observed at  $B_{\text{eff}} = 23^\circ$  and  $4.5^\circ$ . The modeled contributions of intrinsic (filled; both CB and SH) and interparticle contributions (hatched lines; mutual shadowing) are shown separately. In the fits, the intrinsic contribution is assumed to be independent of  $B_{\text{eff}}$ , and the opening angle dependent part is fitted by comparison to a grid of simulation models. Figure from Salo and French (2010).

Figure 1.37 summarizes the results of photometric modeling of opposition brightening based on the Hubble Space telescope observations (Salo and French, 2010). When ring opening angle is large (here  $23^\circ$ ), the reflection is mainly due to particles in the densely packed equatorial plane: consequently the inter-particle shadow hiding contribution to the peak in  $I/F$  is relatively wide. For low  $B_{\text{eff}}$ , the reflection is mainly due to the uppermost, low filling factor layers, which produce a stronger peak. The insert figures illustrate the final separations of observed phase curves into interparticle shadow hiding (dependent on  $B_{\text{eff}}$ ) and intrinsic contributions (same for all  $B_{\text{eff}}$ ). The intrinsic component is also separated to CB and surface shadow hiding components, using the Hapke (2002) models which are commonly applied for the whole phase curve, without taking into account the mutual shadow hiding between particles. Since the interparticle shadow hiding accounts about half of the total opposition brightening, its inclusion has an effect on the estimated CB parameters.

#### 1.8.4 Self-gravity wakes and azimuthal brightness asymmetry

Several types of observations support the existence of self-gravity wakes in Saturn’s rings. Due to their small scale,  $\lambda_{cr} \sim 100$  meters, they are unresolved in direct images. Nevertheless, the wakes have a global signature on how the rings reflect and transmit light, since the reflecting surface area will depend on the viewing direction with respect to the average direction of wakes (see Fig. 1.38). Similarly, the illumination of wakes will depend on the longitude with respect to solar longitude.

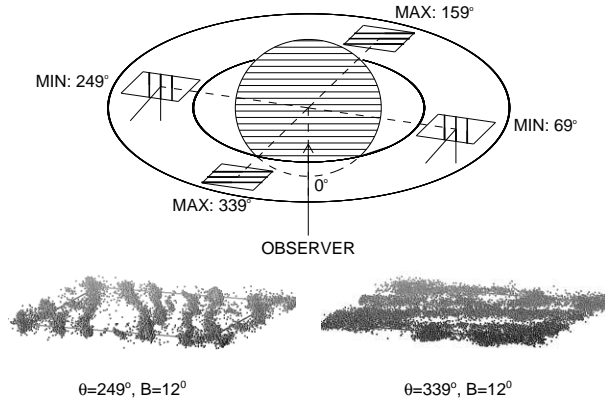


**Figure 1.38** The effect of unresolved self-gravity wakes on global brightness: at intermediate ring opening angles the reflecting surface area has a minimum at longitudes where the rings are viewed along the average major axis of wakes, and correspondingly a maximum when wakes are viewed perpendicularly. Figure from Salo et al. (2004).

The wakes provide a natural explanation to the A ring *azimuthal brightness asymmetry*, discovered already in 1950's (Camichel, 1958), intensively studied in the pre-Voyager era (Ferrin, 1975; Reitsema et al., 1976; Lumme et al., 1977; Thompson et al., 1981). In the ground-based observations the brightness at the mid A ring exhibits two symmetrical minima at the ring longitude  $\theta_{min} \sim 70^\circ$  and  $\sim 250^\circ$  with respect to sub-observer direction. The detailed analysis of low-phase Voyager images (Dones et al., 1993) showed that the amplitude of variations peaks very strongly in the mid-A ring, reaching a full amplitude  $\approx 35\%$  in reflected light at the saturnocentric distance of 128,000 km. The A ring asymmetry was also seen in Voyager transmitted light images (Franklin et al., 1987), whereas for the B ring no asymmetry was detectable. Wakes have also been inferred from the radar echo of rings (Nicholson et al., 2005), and from the way how Saturn's microwave radiation is transmitted through the rings (Dunn et al., 2004). Wakes also affect the ring opacity: the most detailed observations of wakes have been made with the Cassini stellar (Colwell et al., 2006, 2007; Hedman et al., 2007, 2014) and radio occultation measurements (Thomson et al., 2007). Wakes have also a clear signature on the ring's thermal emission (Ferrari et al., 2009; Morishima et al., 2014).

The likely connection of azimuthal brightness asymmetry to Goldreich and Lynden-Bell (1965) and Julian and Toomre (1966) type self-gravity structures was pointed out already by Colombo et al. (1976) (see also Franklin et al., 1987; Dones and Porco, 1989; Dones et al., 1993). The first detailed comparisons between dynamical self-gravitating simulations and Voyager observations were made in Salo et al. (2004), using the photometric Monte Carlo method described above. It was shown that the trailing self-gravity wakes, systematically tilted by about  $20^\circ$  with respect to the local tangential direction can indeed explain the A ring asymmetry ampli-

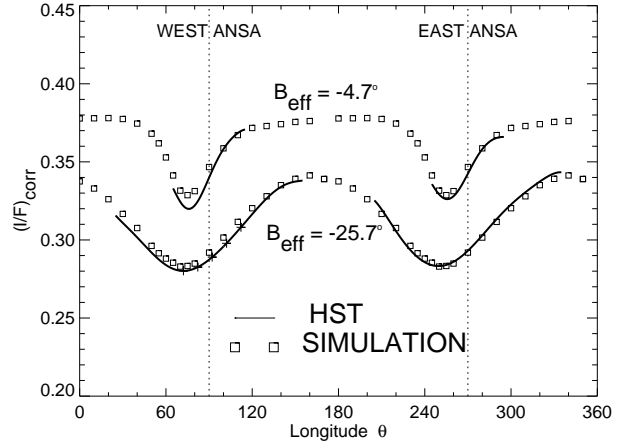


**Figure 1.39** HST observations of the A ring azimuthal asymmetry at two different ring opening angles, with corresponding simulation models assuming identical 'frosty ice' particles. Note the narrower minimum and the increased overall  $I/F$  for  $B_{eff} = 4.5^\circ$ . Figure from French et al. (2007b).

tude and longitude of minimum, both in the reflected and transmitted light observations (in the latter case one also needs to take into account the Saturn-shine contribution which also depends on ring longitude). A somewhat surprising result was (and still is) that the observed  $\theta_{min}$  is better matched by dynamical models consisting of identical particles, than by the presumably more realistic models with an extended size distribution. The shift  $\Delta\theta_{min} \approx 5^\circ$  between size distribution and identical particle models, is the same as the difference in the wake pitch angle implied by the auto-correlation analysis of simulated wakes (see Fig. 1.23). Same conclusion was reached in French et al. (2007b) when comparing identical particle and size distribution simulations with the HST observations; similar shift is also seen in Porco et al. (2008) models of Cassini phase curves.

French et al. (2007b) carried out detailed analysis of the azimuthal brightness variations on the above described Hubble Space telescope data set, covering the full elevation and phase angle ranges accessible from Earth. The change in the asymmetry amplitude, and the width and location of the brightness minima were all found to be in accordance with the predictions of the dynamical wake models (see Fig. 1.39). For example, the asymmetry amplitude is largest at  $B_{eff} \sim 10^\circ$ : when  $B_{eff} \rightarrow 0^\circ$  the sparse inter-wake regions are not anymore visible, while for larger  $B_{eff}$  the reflecting surface area is less sensitive to azimuthal orientation. The observed width of minimum gets narrower at small  $B_{eff}$  which is expected since then the inter-wake gaps are visible only when viewed very precisely along the major axis of wakes. Similar very narrow peak is seen in the amount transmitted light in the low elevation ( $3.45^\circ$ ) stellar occultations (Hedman et al., 2007). Moreover, the HST observations made it possible to fully separate the dependence of  $\theta_{min}$  on the sun-earth longitude difference.

The presence of wakes explains also the A-ring *inverse tilt effect* (the overall  $I/F$  drops with  $B_{eff}$ ; Cuzzi et al., 2002):

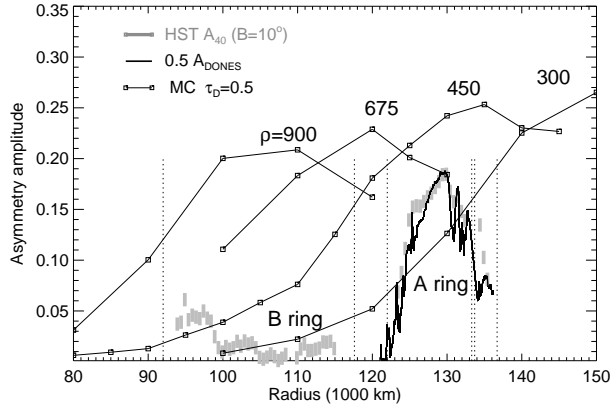


**Figure 1.40** The observed radial dependence of the asymmetry amplitude is compared with dynamical simulations performed for various internal particle densities (labels indicate  $\rho$  in units of  $\text{kgm}^{-3}$ ). Simulations assumed  $\tau_D = 0.5$  and the 'frosty ice'  $\epsilon_n$  model. Both the Hubble Space Telescope observations (filled light gray squares) and models correspond to  $B_{\text{eff}} = 10^\circ$ . The asymmetry amplitude from Voyager images (Dones et al., 1993) is also shown as a solid line, multiplied by a factor of 0.5 to account for the difference in definitions of asymmetry amplitude. Figure from French et al. (2007b).

with increasing opening angle more light leaks through the gaps. In contrast to the A ring, the B ring has a strong *positive tilt effect*, its brightness increasing by  $\sim 30\%$  between  $B_{\text{eff}} = 4^\circ - 26^\circ$ . Early on, this was interpreted in terms of multiple scattering (Esposito and Lumme, 1977; Lumme et al., 1983), but as shown in detail in Salo and French (2010) the observed positive tilt effect follows naturally by the same models which account for the elevation angle dependent opposition effect: in observations at fixed  $\alpha$ , the brightness increases with opening angle since the opposition brightening extends to larger  $\alpha$  for larger  $B_{\text{eff}}$  (see Eq. 1.136).

The Hubble Space telescope observations in French et al. (2007b) confirmed the very strong peaking of asymmetry amplitude in the mid A-ring, matching very well the Dones et al. (1993) measurements. Weak asymmetry was also discovered in the inner B ring, consistent with the stellar occultation observations (Colwell et al., 2007). Fig. 1.40 shows the observed asymmetry amplitude as a function of Saturnocentric distance, and also compares it to a set of dynamical and photometric simulation models. The simulations assume four different internal densities of particles (varying from solid ice density  $900 \text{ kgm}^{-3}$  to  $1/3$  of solid ice density), while all the other simulation parameters are kept fixed. Depending on the assumed internal density of the particles, the self-gravity wake structure emerges at different distances (at certain  $r_h$ , so that  $a \propto \rho^{-1/3}$ , see Fig. 1.22) leading to growth of asymmetry amplitude. With increasing distance, the wakes become clumpier, eventually degrading into particle aggregates. This reduced the longitude-dependence of the reflecting area and thus the amplitude of asymmetry.

Clearly, the distance dependence of the simulation models of Fig. 1.40, following solely from the slow change in the

tidal environment, is much too weak compared to the observed strong peaking at the mid A-ring. As demonstrated in French et al. (2007b), using higher  $\tau_D$ , different  $\epsilon_n(v_n)$  or different size distributions would modify the trends, if the parameters are allowed to vary with distance. For example, the rapid drop of the asymmetry amplitude at the outer A-ring could be related to a rapid increase in the fractional amount of small particles, suggested to rise due to higher impact speeds associated with the stronger perturbations by external satellites (Dones et al., 1993), or perhaps by the self-gravity wakes themselves Salo and Schmidt (2007). The increased pitch angle of wakes at the outer A-ring (French et al., 2007b; Colwell et al., 2006; Hedman et al., 2007) would also be consistent with more extended size distribution. However, truly successful models should account for such distance-dependent changes in a fully self-consistent manner.

## 1.9 Summary

### 1.9.1 What has been covered

In this chapter we have reviewed the basic ingredients of local planetary ring simulations: the use of linearized dynamical equations in a co-moving coordinate system, the shearing periodic boundaries, the modeling of particle impacts, and the calculation of self-gravity. Impacts were treated both as instantaneous velocity changes, and in terms of visco-elastic forces affecting partially overlapping colliding particles. We described different methods for calculating the ring self-gravity, including the often-used approximation in terms of enhanced  $n_z/n$ . The establishment of local energy balance between collisional dissipation and viscous gain (including local, nonlocal and gravitational contributions) was discussed in quite a detail, as well as how to measure from simulations various pressure tensor related quantities characterizing this steady state.

Extensive numerical simulation examples were given, and our aim was to go systematically through the main free parameters of the models, the elasticity and friction in impacts, the size distribution of particles, and their internal density. When possible, the results were given a hydrodynamic interpretation (see Stewart et al., 1984; Schmidt, 2009). The central theme was to illustrate how the  $\nu$  vs.  $\tau_D$  relation, deduced from small scale simulations, can be used to make predictions concerning the viscous stability properties of the ring system. We then gave examples of how the predicted viscous overstabilities and instabilities manifest in larger-scale simulations. Also, we presented a systematic survey of the expected self-gravity wake structure, when using two quite different elasticity laws representing the range of uncertainty for the ring particle physical properties. The Bridges et al. (1984) 'frosty ice' models implies strongly flattened rings ( $H \sim 10$  m at all  $\tau_D$ ) susceptible to oscillatory instability (viscous overstability) and the formation of gravitational wakes, whereas the Hatzes et al. (1988) 'smooth ice' model leads to multilayer rings ( $H \sim 100$  m at low  $\tau_D$ )



where self-gravity wake structure is harder to obtain, but which might be susceptible to viscous amplification of fluctuations (viscous instability).

Finally, we discussed the photometric ray tracing modeling of the particle fields produced by dynamical simulations, and illustrated how the dynamical models for dense flat rings (with  $D_3 \sim 0.1$ ) explain in a natural manner many photometric observations of the rings, like the azimuthal brightness asymmetry related to self-gravity wakes, and the overall deviations from classical radiative transfer theory applicable at the limit  $D_3 = 0$ . Also, we demonstrated the importance to take into account the mutual shadow hiding effect when deducing particle intrinsic properties from the modeling of opposition brightening.

### 1.9.2 Material not covered

Several important aspects of ring dynamics have not been covered by this review, both related to physical mechanisms operating in planetary rings, and to technical aspects of simulations. For example, we have not discussed the effects of adhesive forces and particle coagulation and fragmentation (see e.g. Perrine et al., 2011; Perrine and Richardson, 2012), nor described in detail the formation of gravitational aggregates (see e.g. Ohtsuki, 1993; Salo, 1995; Karjalainen and Salo, 2004; Albers and Spahn, 2006; Porco et al., 2007; Yasui et al., 2014; Hyodo and Ohtsuki, 2014, 2015). Also, we have not described dynamical simulations of embedded moonlets (e.g. Seiß et al., 2005; Lewis and Stewart, 2005, 2009; Pan et al., 2012) nor dynamical/photometric simulations of propeller structures (Sremčević et al., 2007), or those addressing rings perturbed by satellite resonance perturbations, either by using azimuthally complete rings (Hänninen and Salo, 1994, 1995) or with local calculation regions with a time-variable radial width (Mosqueira, 1996), or by applying streamline formalisms (Hahn and Spitale, 2013). On the technical side, we have not addressed parallelization of the calculations, nor current codes utilizing such methods, like *pkdgrav* (Richardson et al., 2000; Porco et al., 2008), or the publicly available *rebound* code (Rein and Liu, 2012). Similarly, we have not covered simulations addressing the large scale evolution of rings, in terms of viscous radial evolution (Charnoz et al., 2010), or via ballistic transport of mass and angular momentum (Durisen et al., 1989; Estrada et al., 2015).

### 1.9.3 Some open questions

There are several open problems in the ring dynamics, which in principle can be tackled by improved local simulations.

- *What is behind the ubiquitous fine-structure observed in Saturn's rings?*

The viscous overstability of dense, strongly flattened systems is the leading candidate for the regular axisymmetric density variations seen in the inner A ring and the B ring. As such, this would favor dissipative particle impacts ("frosty ice") and a low internal density of particles ( $\rho \leq 300 - 450 \text{ kg m}^{-3}$ ). Nevertheless, viscous instability

would provide an attractive alternative for the almost bimodal variations seen in many locations of the B ring. In its simplest form it seems to require very elastic particles and dynamically hot rings, which is not easy to reconcile with the existence of self-gravity wakes.

- *What is interplay between self-gravity wakes and viscous overstability?*

Inclusion of self-gravity leads to steeper density-viscosity relation, and is thus expected to promote viscous overstability. Indeed, this is seen when the effect of self-gravity is approximated via enhanced  $n_z/n$ . However, when full self-gravity is included the inclined self-gravity wakes, which have roughly the same radial scale, seem to suppress the growth of axisymmetric overstable oscillations. Is this due to the limitations in the current fully self-gravitating simulations?

- *What is the relation between ring optical depth and surface mass density variations?*

Several recent studies have indicated that there is a poor correlation between ring optical depth and surface density (Baillié et al., 2011; Tiscareno et al., 2013; Hedman and Nicholson, 2016). For example, the C ring plateaux are found to have similar  $\Sigma$  as the background ring, regardless of having a factor of four larger  $\tau_\perp$  (Hedman and Nicholson, 2014). The easiest explanation would be a larger fraction of smaller particles in the plateaux: such a difference might arise due to size-selective viscosity instability described in Sect. 1.7.2.1. However, this is not supported by the radio occultation measurements, which indicate that the plateaux have a larger average particle size (Cuzzi et al., 2009). Differences in particle densities and compositions have been suggested (Hedman and Nicholson, 2014) but no definite model yet exists.

- *Why does the amplitude of azimuthal asymmetry peak so strongly in the mid A ring?*

The effective viscosities obtained from the damping of A ring weak density waves (Tiscareno et al., 2007) are consistent with the viscosities estimated from self-gravitating simulations (Daisaka et al., 2001, Sect. 1.6.2.3) performed with solid ice density. Likewise, the outer edge of the A ring fits well to the distance where frosty ice particles with  $\rho \approx 900 \text{ kg m}^{-3}$  start rapidly collapsing into gravitationally bound aggregates (see Karjalainen and Salo, 2004, for simulation survey exploring the effects of elastic properties and size distribution). Still, such parameters would yield much stronger wake structure than observed, with a maximum amplitude attained much closer to planet, and with much shallower dependence on distance. Another puzzle with azimuthal asymmetry is the longitude of minimum, which matches very well with models of identical particles, but deviates clearly from that currently predicted by size distribution models.

- *Combination of photometric and dynamical simulations is a very powerful modeling tool, which needs to be applied to Cassini data in a similar manner as the HST data has been analysed.* The superior imaging resolution ( $\sim \text{km}$  in comparison to  $\sim 10^3 \text{ km}$  in HST) and coverage of wide

range of geometries provides extremely strong constraints for any dynamical model.

Improved simulation models, including both adhesion and fully consistent self-gravity, and allowing for the possibility of size-dependent or otherwise variable particle properties (elasticity, frictions, internal density) are clearly needed for better understanding of the real planetary rings.

## REFERENCES

- Albers, N., and Spahn, F. 2006. The influence of particle adhesion on the stability of agglomerates in Saturn’s rings. *Icarus*, **181**, 292–301.
- Araki, S. 1988. The dynamics of particle disks. II. Effects of spin degrees of freedom. *Icarus*, **76**, 182–198.
- Araki, S. 1991. The dynamics of particle disks III. Dense and spinning particle disks. *Icarus*, **90**, 139–171.
- Araki, S., and Tremaine, S. 1986. The dynamics of dense particle disks. *Icarus*, **65**, 83–109.
- Baillié, K., Colwell, J. E., Lissauer, J. J., Esposito, L. W., and Sremčević, M. 2011. Waves in Cassini UVIS stellar occultations. 2. The C ring. **216**, 292–308.
- Barkstrom, B. R. 1973. A comparison of the Minneart reflectance law and the reflectance from a nonconservative isotropic scattering atmosphere. *J. Geophys. Res.*, **78**, 6370–6372.
- Barnes, J., and Hut, P. 1986. A hierarchical  $O(N \log N)$  force-calculation algorithm. *Nature*, **324**, 446–449.
- Borderies, N., Goldreich, P., and Tremaine, S. 1985. A granular flow model for dense planetary rings. *Icarus*, **63**, 406–420.
- Brahic, A. 1977. Systems of colliding bodies in a gravitational field. I - Numerical simulation of the standard model. *Astron. & Astrophys.*, **54**, 895–907.
- Bridges, F.G., Hatzes, A.P., and Lin, D.N.C. 1984. Structure, stability and evolution of Saturn’s rings. *Nature*, **309**, 333–338.
- Burns, J.A., and Cuzzi, J. N. 2006. Our local astrophysical laboratory. *Science*, **312**, 1753–1755.
- Camichel, H. 1958. Mesures photométriques de Saturne et de son anneau. *Annales d’Astrophysique*, **21**, 231–242.
- Chandrasekhar, S. 1960. *Radiative transfer*.
- Charnoz, S., Salmon, J., and Crida, A. 2010. The recent formation of Saturn’s moonlets from viscous spreading of the main rings. **465**, 752–754.
- Ciarniello, M., Capaccioni, F., and Filacchione, G. 2014. A test of Hapke’s model by means of Monte Carlo ray-tracing. *Icarus*, **237**, 293–305.
- Colombo, G., Goldreich, P., and Harris, A. W. 1976. Spiral structure as an explanation for the asymmetric brightness of Saturn’s A ring. *Nature*, **264**, 344–345.
- Colwell, J. E., Esposito, L. W., and Sremčević, M. 2006. Self-gravity wakes in Saturn’s A ring measured by stellar occultations from Cassini. *Geophys. Res. Lett.*, **33**, L07201.1–L07201.4.
- Colwell, J. E., Esposito, L. W., Sremčević, M., Stewart, G. R., and McClintock, W. E. 2007. Self-gravity wakes and radial structure of Saturn’s B ring. *Icarus*, **190**, 127–144.
- Cundall, P. A., and Strack, O. D. L. 1979. A discrete numerical model for granular assemblies. *Geotechnique*, **29**, 47–65.
- Cuzzi, J., Clark, R., Filacchione, G., French, R., Johnson, R., Marouf, E., and Spilker, L. 2009. Ring Particle Composition and Size Distribution. Page 459 of: Dougherty, M. K., Esposito, L. W., and Krimigis, S. M. (eds), *Saturn from Cassini-Huygens*.
- Cuzzi, J. N., Durisen, R. H., Burns, J. A., and Hamill, P. 1979. The vertical structure and thickness of Saturn’s rings. *Icarus*, **38**, 54–68.
- Cuzzi, J. N., French, R. G., and Dones, L. 2002. HST Multicolor (255–1042 nm) Photometry of Saturn’s Main Rings. I: Radial Profiles, Phase and Opening Angle Variations, and Regional Spectra. *Icarus*, **158**, 199–223.
- Cuzzi, J. N., Burns, J. A., Charnoz, S., Clark, R. N., Colwell, J. E., Dones, L., Esposito, L. W., Filacchione, G., French, R. G., Hedman, M. M., Kempf, S., Marouf, E. A., Murray, C. D., Nicholson, P. D., Porco, C. C., Schmidt, J., Showalter, M. R., Spilker, L. J., Spitale, J. N., Srama, R., Sremčević, M., Tiscareno, M. S., and Weiss, J. 2010. An Evolving View of Saturn’s Dynamic Rings. *Science*, **327**, 1470–1475.
- Daisaka, H., and Ida, S. 1999. Spatial structure and coherent motion in dense planetary rings induced by self-gravitational instability. *Earth, Planets, and Space*, **51**, 1195–1213.
- Daisaka, H., Tanaka, H., and Ida, S. 2001. Viscosity in a dense planetary ring with self-gravitating particles. *Icarus*, **154**, 296–312.
- Déau, E. 2015. The opposition effect in Saturn’s main rings as seen by Cassini ISS: 2. Constraints on the ring particles and their regolith with analytical radiative transfer models. *Icarus*, **253**, 311–345.
- Déau, E., Dones, L., Charnoz, S., West, R. A., Brahic, A., Decriem, J., and Porco, C. C. 2013. The opposition effect in Saturn’s main rings as seen by Cassini ISS: 1. Morphology of phase functions and dependence on the local optical depth. *Icarus*, **226**, 591–603.
- Dilley, J.P. 1993. Energy loss in collisions of icy spheres: Loss mechanism and size-mass dependence. *Icarus*, **105**, 225–234.
- Dones, L., and Porco, C. C. 1989. Spiral density wakes in Saturn’s A ring? In: *Bull. American Astron. Soc.*, vol. 21.
- Dones, L., Cuzzi, J. N., and Showalter, M. R. 1993. Voyager Photometry of Saturn’s A Ring. *Icarus*, **105**, 184–215.
- Dunn, D. E., Molnar, L. A., Niehof, J. T., de Pater, I., and Lissauer, J. J. 2004. Microwave observations of Saturn’s rings: anisotropy in directly transmitted and scattered saturnian thermal emission. *Icarus*, **171**, 183–198.
- Durisen, R. H., Cramer, N. L., Murphy, B. W., Cuzzi, J. N., Mullikin, T. L., and Cederbloom, S. E. 1989. Ballistic transport in planetary ring systems due to particle erosion mechanisms. I - Theory, numerical methods, and illustrative examples. *Icarus*, **80**, 136–166.
- Esposito, L. W. 1979. Extensions to the classical calculation of the effect of mutual shadowing in diffuse reflection. *Icarus*, **39**, 69–80.
- Esposito, L. W., and Lumme, K. 1977. The tilt effect for Saturn’s rings. *Icarus*, **31**, 157–167.

- Estrada, P. R., Durisen, R. H., Cuzzi, J. N., and Morgan, D. A. 2015. Combined structural and compositional evolution of planetary rings due to micrometeoroid impacts and ballistic transport. *252*, 415–439.
- Ferrari, C., Brooks, S., Edgington, S., Leyrat, C., Pilorz, S., and Spilker, L. 2009. Structure of self-gravity wakes in Saturn’s A ring as measured by Cassini CIRS. *Icarus*, **199**, 145–153.
- Ferrin, I. 1975. On the structure of Saturn’s rings and the ‘real’ rotational period for the planet. *Astrophys. Space Sci.*, **33**, 453–457.
- Franklin, F. A., Cook, A. F., Barrey, R. T. F., Roff, C. A., Hunt, G. E., and de Rueda, H. B. 1987. Voyager observations of the azimuthal brightness variations in Saturn’s rings. *Icarus*, **69**, 280–296.
- French, R. G., Salo, H., McGhee, C. A., and Dones, L. 2007a. HST observations of azimuthal asymmetry in Saturn’s rings. *Icarus*, **189**, 493–522.
- French, R. G., Verbiscer, A., Salo, H., McGhee, C., and Dones, L. 2007b. Saturn’s Rings at True Opposition. *Publ. Astron. Soc. Pacific*, **119**, 623–642.
- Goldreich, P., and Lynden-Bell, D. 1965. II. Spiral arms as sheared gravitational instabilities. *Mon. Not. R. Astron. Soc.*, **130**, 125–158.
- Goldreich, P., and Tremaine, S. 1978a. The excitation and evolution of density waves. *Astrophys. J.*, **222**, 850–858.
- Goldreich, P., and Tremaine, S. 1978b. The velocity dispersion in Saturn’s rings. *Icarus*, **34**, 227–239.
- Hahn, J. M., and Spitale, J. N. 2013. An N-body Integrator for Gravitating Planetary Rings, and the Outer Edge of Saturn’s B Ring. **772**, 122.
- Hämeen-Anttila, K. A. 1978. An improved and generalized theory for the collisional evolution of Keplerian systems. *Astrophys. Space Sci.*, **58**, 477–519.
- Hämeen-Anttila, K. A. 1982. Saturn’s rings and bimodality of Keplerian systems. *Earth, Moon & Planets*, **26**, 171–196.
- Hämeen-Anttila, K. A., and Lukkari, J. 1980. Numerical simulations of collisions in Keplerian systems. *Astrophys. Space Sci.*, **71**, 475–497.
- Hämeen-Anttila, K. A., and Salo, H. 1993. Generalized Theory of Impacts in Particulate Systems. *Earth, Moon & Planets*, **62**, 47–84.
- Hänninen, J., and Salo, H. 1994. Collisional simulations of satellite Lindblad resonances. 2: Formation of narrow ringlets. *Icarus*, **108**, 325–346.
- Hänninen, J., and Salo, H. 1995. Formation of isolated narrow ringlets by a single satellite. *Icarus*, **117**, 435–438.
- Hapke, B. 1986. Bidirectional reflectance spectroscopy. IV - The extinction coefficient and the opposition effect. *Icarus*, **67**, 264–280.
- Hapke, B. 1990. Coherent backscatter and the radar characteristics of outer planet satellites. *Icarus*, **88**, 407–417.
- Hapke, B. 2002. Bidirectional Reflectance Spectroscopy. 5. The Coherent Backscatter Opposition Effect and Anisotropic Scattering. **157**, 523–534.
- Hapke, B. 2008. Bidirectional reflectance spectroscopy. 6. Effects of porosity. *Icarus*, **195**, 918–926.
- Hatzes, A., Bridges, F. G., and Lin, D. N. C. 1988. Collisional properties of ice spheres at low impact velocities. *Mon. Not. R. Astron. Soc.*, **231**, 1091–1115.
- Hedman, M. M., and Nicholson, P. D. 2014. More Kronoseismology with Saturn’s rings. *Mon. Not. Royal Astron. Soc.*, **444**, 1369–1388.
- Hedman, M. M., and Nicholson, P. D. 2016. The B-ring’s surface mass density from hidden density waves: Less than meets the eye? *ArXiv e-prints 1601.07955*.
- Hedman, M. M., Nicholson, P. D., Salo, H., Wallis, B. D., Buratti, B. J., Baines, K. H., Brown, R. H., and Clark, R. N. 2007. Self-gravity wake structures in Saturn’s A ring revealed by Cassini VIMS. *Astron. J.*, **133**, 2624–2629.
- Hedman, M. M., Burns, J. A., Evans, M. W., Tiscareno, M. S., and Porco, C. C. 2011. Saturn’s Curiously Corrugated C Ring. *Science*, **332**, 708–711.
- Hedman, M. M., Nicholson, P. D., and Salo, H. 2014. Exploring Overstabilities in Saturn’s A Ring Using Two Stellar Occultations. *Astron. J.*, **148**, 1–9.
- Hernquist, L., and Katz, N. 1989. TREESPH - A unification of SPH with the hierarchical tree method. *Astrophys. J., Supp.*, **70**, 419–446.
- Hyodo, R., and Ohtsuki, K. 2014. Collisional Disruption of Gravitational Aggregates in the Tidal Environment. *Astrophys. J.*, **787**, 56.
- Hyodo, R., and Ohtsuki, K. 2015. Saturn’s F ring and shepherd satellites a natural outcome of satellite system formation. *Nature Geoscience*, **8**(Sept.), 686–689.
- Julian, W. H., and Toomre, A. 1966. Non-axisymmetric responses of differentially rotating disks of stars. *Astrophys. J.*, **146**, 810–827.
- Karjalainen, R., and Salo, H. 2004. Gravitational accretion of particles in Saturn’s rings. *Icarus*, **172**, 328–348.
- Latter, H. N., and Ogilvie, G. I. 2008. Dense planetary rings and the viscous overstability. *Icarus*, **195**, 725–751.
- Latter, H. N., and Ogilvie, G. I. 2009. The viscous overstability, nonlinear wavetrains, and finescale structure in dense planetary rings. *Icarus*, **202**, 565–583.
- Latter, H. N., and Ogilvie, G. I. 2010. Hydrodynamical simulations of viscous overstability in Saturn’s rings. *Icarus*, **210**, 318–329.
- Lewis, M. C., and Stewart, G. R. 2000. Collisional Dynamics of Perturbed Planetary Rings. I. **120**, 3295–3310.
- Lewis, M. C., and Stewart, G. R. 2005. Expectations for Cassini observations of ring material with nearby moons. *Icarus*, **178**, 124–143.
- Lewis, M. C., and Stewart, G. R. 2009. Features around embedded moonlets in Saturn’s rings: The role of self-gravity and particle size distributions. **199**, 387–412.
- Lin, D. N. C., and Bodenheimer, P. 1981. On the stability of Saturn’s rings. *Astrophys. J. Lett.*, **248**, L83–L86.
- Longaretti, P.-Y., and Rappaport, N. 1995. Viscous overstabilities in dense narrow planetary rings. *Icarus*, **116**, 376–396.
- Lukkari, J. 1981. Collisional amplification of density fluctuations in Saturn’s rings. *Nature*, **292**, 433–435.
- Lumme, K., and Bowell, E. 1981. Radiative transfer in the surfaces of atmosphereless bodies. I - Theory. II - Interpretation of phase curves. *Astron. J.*, **86**, 1694–1721.
- Lumme, K., Esposito, L. W., Irvine, W. M., and Baum, W. A. 1977. Azimuthal brightness variations of Saturn’s rings. II - Observations at an intermediate tilt angle. *Astrophys. J. Lett.*, **216**, L123–L126.
- Lumme, K., Irvine, W. M., and Esposito, L. W. 1983. Theoretical interpretation of the ground-based photometry of Saturn’s B ring. *Icarus*, **53**, 174–184.
- Lynden-Bell, D., and Kalnajs, A. J. 1972. On the Generating Mechanism of Spiral Structure. *Mon. Not. R. Astron. Soc.*, **157**, 1–30.



- Makino, J., and Funato, Y. 1993. The GRAPE Software System. *Publications of the Astronomical Society of Japan*, **45**, 279–288.
- Michikoshi, S., Fujii, A., Kokubo, E., and Salo, H. 2015. Dynamics of Self-gravity Wakes in Dense Planetary Rings. I. Pitch Angle. *Astrophys. J.*, **812**, 151.
- Mishchenko, M. I. 1992. The angular width of the coherent backscatter opposition effect - an application to icy outer planet satellites. *ApJSS*, **194**, 327–333.
- Morishima, R., and Salo, H. 2006. Simulations of dense planetary rings IV. Spinning self-gravitating particles with size distributions. *Icarus*, **181**, 272–291.
- Morishima, R., Spilker, L., and Turner, N. 2014. Azimuthal temperature modulations of Saturn's A ring caused by self-gravity wakes. *Icarus*, **228**, 247–259.
- Mosqueira, I. 1996. Local simulations of perturbed dense planetary rings. *Icarus*, **122**, 128–152.
- Nelson, R. M., Hapke, B. W., Smythe, W. D., and Spilker, L. J. 2000. The Opposition Effect in Simulated Planetary Regoliths. Reflectance and Circular Polarization Ratio Change at Small Phase Angle. *Icarus*, **147**, 545–558.
- Nicholson, P. D., French, R. G., Campbell, D. B., Margot, J.-L., Nolan, M. C., Black, G. J., and Salo, H. J. 2005. Radar imaging of Saturn's rings. *Icarus*, **177**, 32–62.
- Ohtsuki, K. 1993. Capture probability of colliding planetesimals: Dynamical constraints on accretion of planets, satellites, and ring particles. *Icarus*, **106**, 228–246.
- Ohtsuki, K. 1999. Evolution of particle velocity dispersion in a circumplanetary disk due to inelastic collisions and gravitational interactions. *Icarus*, **137**, 152–177.
- Ohtsuki, K. 2006. Rotation rate and velocity dispersion of planetary ring particles with size distribution. I. Formulation and analytic calculation. *Icarus*, **183**, 373–383.
- Ohtsuki, K., and Emori, H. 2000. Local N-Body Simulations for the Distribution and Evolution of Particle Velocities in Planetary Rings. *Astron. J.*, **119**, 403–416.
- Ohtsuki, K., and Toyama, D. 2005. Local N-body simulations for the rotation rates of particles in planetary rings. *Astron. J.*, **130**, 1302–1310.
- Pan, M., Rein, H., Chiang, E., and Evans, S. N. 2012. Stochastic flights of propellers. **427**, 2788–2796.
- Perrine, R. P., and Richardson, D. C. 2012. N-body simulations of cohesion in dense planetary rings: A study of cohesion parameters. **219**, 515–533.
- Perrine, R. P., Richardson, D. C., and Scheeres, D. J. 2011. A numerical model of cohesion in planetary rings. **212**, 719–735.
- Porco, C. C., Weiss, J. W., Richardson, D. C., Dones, L., Quinn, T., and Throop, H. 2008. Simulations of the dynamical and light-scattering behavior of Saturn's rings and the derivation of ring particle and disk properties. *Astron. J.*, **136**, 2172–2200.
- Porco, C.C., Thomas, P.C., Weiss, J. W., and Richardson, D. C. 2007. Saturn's small inner satellites: Clues to their origins. *Science*, **318**, 1602–1607.
- Pöschel, T., and Schwager, T. 2005. *Computational Granular Dynamics*.
- Poulet, F., Cuzzi, J. N., French, R. G., and Dones, L. 2002. A Study of Saturn's Ring Phase Curves from HST Observations. *Icarus*, **158**, 224–248.
- Rein, H., and Latter, H. N. 2013. Large-scale N-body simulations of the viscous overstability in Saturn's rings. *Mon. Not. Royal Astron. Soc.*, **431**, 145–158.
- Rein, H., and Liu, S.-F. 2012. REBOUND: an open-source multi-purpose N-body code for collisional dynamics. *Astron. & Astrophys.*, **537**, A128.
- Reitsema, H. J., Beebe, R. F., and Smith, B. A. 1976. Azimuthal brightness variations in Saturn's rings. *Astron. J.*, **81**, 209–215.
- Richardson, D. C. 1993. A new tree code method for simulation of planetesimal dynamics. *Mon. Not. R. Astron. Soc.*, **261**, 396–414.
- Richardson, D. C., Quinn, T., Stadel, J., and Lake, G. 2000. Direct Large-Scale N-Body Simulations of Planetesimal Dynamics. **143**, 45–59.
- Richardson, D.C. 1994. Tree code simulations of planetary rings. *Mon. Not. R. Astron. Soc.*, **269**, 493–511.
- Robbins, S. J., Stewart, G. R., Lewis, M. C., Colwell, J. E., and Sremčević, M. 2010. Estimating the masses of Saturn's A and B rings from high-optical depth N-body simulations and stellar occultations. *Icarus*, **206**, 431–445.
- Safronov, V. 1969. *Evolution of the protoplanetary cloud and the formation of the earth and planets*.
- Salo, H. 1987a. Collisional evolution of rotating, non-identical particles. *Moon Planets*, **38**, 149–181.
- Salo, H. 1987b. Numerical simulations of collisions between rotating particles. *Icarus*, **70**, 37–51.
- Salo, H. 1991. Numerical simulations of dense collisional systems. *Icarus*, **92**, 367–368.
- Salo, H. 1992a. Gravitational wakes in Saturn's rings. *Nature*, **359**, 619–621.
- Salo, H. 1992b. Numerical simulations of dense collisional systems. II. Extended distribution of particle sizes. *Icarus*, **96**, 85–106.
- Salo, H. 1995. Simulations of dense planetary rings. III. Self-gravitating identical particles. *Icarus*, **117**, 287–312.
- Salo, H. 2001. Numerical Simulations of the Collisional Dynamics of Planetary Rings. Pages 330–349 of: Pöschel, T., and Luding, S. (eds), *Granular Gases*. Lecture Notes in Physics, Berlin Springer Verlag, vol. 564.
- Salo, H., and French, R. G. 2010. The opposition and tilt effects of Saturn's rings from HST observations. *Icarus*, **210**, 785–816.
- Salo, H., and Karjalainen, R. 2003. Photometric modeling of Saturn's rings. I. Monte Carlo method and the effect of nonzero volume filling factor. *Icarus*, **164**, 428–460.
- Salo, H., and Schmidt, J. 2010. N-body simulations of viscous instability of planetary rings. *Icarus*, **206**, 390–409.
- Salo, H., Schmidt, J., and Spahn, F. 2001. Viscous overstability in Saturn's B ring: I. Direct simulations and measurement of transport coefficients. *Icarus*, **153**, 295–315.
- Salo, H., Karjalainen, R., and French, R. G. 2004. Photometric modeling of Saturn's rings. II. Azimuthal asymmetry in reflected and transmitted light. *Icarus*, **170**, 70–90.
- Salo, H. J., and Schmidt, J. 2007. Release of impact-debris in perturbed ring regions: Dynamical and photometric simulations. In: *Bulletin of the American Astronomical Society*. Bulletin of the American Astronomical Society, vol. 38.
- Schmidt, J., and Salo, H. 2003. A weakly nonlinear model for viscous overstability in Saturn's dense rings. *Physical Review Letters*, **90**(6), 061102.
- Schmidt, J., Salo, H., Spahn, F., and Petzschmann, Olaf. 2001. Viscous overstability in Saturn's B ring: II. Hydrodynamic theory and comparison to simulations. *Icarus*, **153**, 316–331.
- Schmidt, J., Ohtsuki K. Rappaport N. Salo H. Spahn F. 2009. Dynamics of Saturn's Dense Rings. Page 413 of: Dougherty, M. K., Esposito, L. W., and Krimigis, S. M. (eds), *Saturn from Cassini-Huygens*.

- Schmit, U., and Tscharnuter, W.M. 1995. A fluid dynamical treatment of the common action of self-gravitation, collisions, and rotation in Saturn's B-ring. *Icarus*, **115**, 304–319.
- Schmit, U., and Tscharnuter, W.M. 1999. On the formation of the fine-scale structure in Saturn's B ring. *Icarus*, **138**, 173–187.
- Seiß, M., Spahn, F., Sremčević, M., and Salo, H. 2005. Structures induced by small moonlets in Saturn's rings: Implications for the Cassini mission. *Geophys. Res. Lett.*, **32**.
- Sellwood, J. A. 2014. GALAXY package for N-body simulation. *ArXiv e-prints 1406.6606*.
- Shu, F. H., and Stewart, G. R. 1985. The collisional dynamics of particulate disks. *Icarus*, **62**, 360–383.
- Spahn, F., and Sremčević, M. 2000. Density patterns induced by small moonlets in Saturn's rings? *Astron. & Astrophys.*, **358**, 368–372.
- Spahn, F., Hertzsch, J.-M., and Brilliantov, N.V. 1995. The role of particle collisions for the dynamics in planetary rings. *Chaos, Solitons and Fractals*, **5**, 1945–1964.
- Springel, V. 2005. The cosmological simulation code GADGET-2. *Mon. Not. Royal Astron. Soc.*, **364**, 1105–1134.
- Sremčević, M., Schmidt, J., Salo, H., Seiß, M., Spahn, F., and Albers, N. 2007. A belt of moonlets in Saturn's A ring. *Nature*, **449**, 1019–1021.
- Stewart, G. R., Lin, D. N. C., and Bodenheimer, P. 1984. Collision-induced transport processes in planetary rings. Pages 447–512 of: Greenberg, R., and Brahic, A. (eds), *Planetary Rings*. Tucson Arizona: Univ. of Arizona Press.
- Supulver, K. D., Bridges, F. G., and Lin, D. N. C. 1995. The coefficient of restitution of ice particles in glancing collisions: Experimental results for unfrosted surfaces. *Icarus*, **113**, 188–199.
- Tanaka, H., Ohtsuki, K., and Daisaka, H. 2003. A new formulation of the viscosity in planetary rings. *Icarus*, **161**, 144–156.
- Thompson, W. T., Lumme, K., Irvine, W. M., Baum, W. A., and Esposito, L. W. 1981. Saturn's rings - Azimuthal variations, phase curves, and radial profiles in four colors. *Icarus*, **46**, 187–200.
- Thomson, F. S., Marouf, E. A., Tyler, G. L., French, R. G., and Rappoport, N. J. 2007. Periodic microstructure in Saturn's rings A and B. *Geophys. Res. Lett.*, **34**, 24203–+.
- Tiscareno, M. S., Burns, J. A., Nicholson, P. D., Hedman, M. M., and Porco, C. C. 2007. Cassini imaging of Saturn's rings: II. A wavelet technique for analysis of density waves and other radial structure in the rings. *Icarus*, **189**, 14–34.
- Tiscareno, M. S., Perrine, R. P., Richardson, D. C., Hedman, M. M., Weiss, J. W., Porco, C. C., and Burns, J. A. 2010. An Analytic Parameterization of Self-Gravity Wakes in Saturn's Rings, with Application to Occultations and Propellers. *Astron. J.*, **139**, 492–503.
- Tiscareno, M. S., Hedman, M. M., Burns, J. A., Weiss, J. W., and Porco, C. C. 2013. Probing the inner boundaries of Saturn's A ring with the Iapetus -1:0 nodal bending wave. **224**, 201–208.
- Toomre, A. 1964. On the gravitational stability of a disk of stars. *Astrophys. J.*, **139**, 1217–1238.
- Toomre, A. 1981. What amplifies the spirals. Pages 111–136 of: Fall, S. M., and Lynden-Bell, D. (eds), *Structure and Evolution of Normal Galaxies*.
- Toomre, A., and Kalnajs, A. J. 1991. Spiral chaos in an orbiting patch. Pages 341–358 of: Sundelius, B. (ed), *Dynamics of Disc Galaxies*. Almquist-Wiksell, Göteborg.
- Trulsen, J. 1972. Numerical simulation of jetstreams, I: The three-dimensional case. *Astrophys. Space Sci.*, **17**, 241–262.
- Ward, W. R. 1981. On the radial structure of Saturn's rings. *Geophys. Res. Lett.*, **8**, 641–643.
- Wisdom, J., and Tremaine, S. 1988. Local simulations of planetary rings. *Astron. J.*, **95**, 925–940.
- Yasui, Y., Ohtsuki, K., and Daisaka, H. 2014. Gravitational Accretion of Particles onto Moonlets Embedded in Saturn's Rings. *Astrophys. J.*, **797**, 93.